Search for Top in the electron-muon Channel at 1.8 TeV with DZERO

A Thesis Presented

by

Vipin Bhatnagar

to

The Faculty of Science

in Fulfillment of the Requirement

for the Degree of

Doctor of Philosophy

in

Physics

Panjab University, Chandigarh

November, 1996

©1996 by Vipin Bhatnagar

All rights reserved. Typesetted in LaTeX on a PC running Linux OS.

Search for Top in the electron-muon Channel at 1.8 TeV with DZERO

Abstract

The DØ experiment announced the production of the Standard Model Top quark in proton-antiproton collisions at a center of mass energy of 1.8 TeV using the Fermilab Tevatron. The work presented here in this thesis describes the analysis performed for the Top quark search in the $e\mu+$ jets channel using an integrated luminosity of 76.6 pb^{-1} accumulated during the 1994-1995 run. This search analysis yields two top candidate events with an estimated background of 0.318 ± 0.075 events.

Vipin Bhatnagar, Department of Physics

Panjab University, November 1996

Dedicated to My Parents

Acknowledgements

First of all I would like to thank my thesis supervisors Suman Bala and J. M. Kohli for the continual support and encouragement during my stay with the Department of Physics as a research student. At the same time I would like to thank Raja for being an active player in the Indo-US exchange program for the participation of Panjab group in DØ and for his help and suggestions during my stay at Fermilab.

I would like to thank all the members of DØ collaboration who worked hard, day and night, building, operating and maintaining the detector. I feel myself proud to be a part of such a nice DØ family with whom my three and half years stay at Fermilab was a life time experience. My special thanks and regards go to Paul Grannis and Mont for ably leading the whole collaboration during all these years.

Thanks and regards to Steve Wimpenny, Meena and Jeff for taking care of the dileptonians as the group leaders. "Bolshoye Spaciba, Mon Capitan"-many many thanks to "Chief" alias Jim for being a very good friend as well as my analysis advisor.

Remembering the good old days, I would like to thank the Indian gang at Fermilab comprising of Bala, Meena & Ulrich, Brajesh, Mani, Pushpa, Ashutosh, Harsh, Dev, Mrinmoy & Bornali, Dhiman & Sudeshna, Susy-hankar (Chabba Dala), Shekhar & Tanuja, Thakur & Prajakta, Sailesh, Srini, Parua, Ambrish, Arijit, Manoj, Prakash, Prashant (guest appearances!) and Ajay. There presence at Fermilab (especially at 8 Shabbona and Dorm 5) made me forget my home in India.

I want to thank R. Mac Eochaidh (Bob), Ssumin Chang, C. L. Kim, Enuil Won,

Raul, Hoje, Choi, Al Ito, Nobu and others for such a nice time at DØ. Thanks to all the Chakra members, playing soccer with them for over 3 years was great fun.

My thanks and regards to Gene Fisk who, besides being my supervisor at Fermilab, listened and understood my problems and supported me financially during the last four months at Fermilab. Special thanks to Barbara Edmonson for taking care of all the official dealings and problems during my entire stay at Fermilab.

I would like to thank the Accelerator Division for keeping the $p\overline{p}$ collisions happening in the Tevatron, Paul Russo for keeping the DØ computing in a healthy state and to Scott who helped, even at odd hours, solve the computing problems. I thank Alan Jonckheere (Chakra goalkeeper) for helping us solve the computing problems which enabled me to reproduce some of the analysis results locally.

At Panjab, I would like to thank Shappy for lots of discussions regarding the analysis and for sending the new updates when he was at Fermilab. Thanks to my fellow classmates and friends Surendra, Jagbir & Harjeet, Dogra, Sharma, A. C., P. S. Gill, Raman, Seema, Commando, Mohindru for all the nice times during my stay in the department. Thanks and regards to Jasbir Singh for lots of healthy discussions on various physics aspects and being a friendly advisor to me. My deep regards and thanks to the Dept. of Physics Chairman Prof. Khanna and the Ex-Chairman Prof. Pathak for all the support to complete this work on time.

In the end I would like to acknowledge the sponsoring agency, NSF of the U.S.A. for supporting this work and the contribution of Free Software Foundation for the software tools which made it possible for me to compile this work at Panjab.

Contents

1 Introduction **1**

1.1 Overview of particle physics 2

1.2 The Standard Model: A Brief Picture 7

1.3 Top Quark 15

1.3.1 Is it "truth"? 15

1.3.2 Anomalies 16

1.3.3 $B^0 - \bar{B}^0$ Oscillations 17

1.3.4 **b** Decays 18

1.3.5 A_{FB} in $e^+e^- \to b\bar{b}$ 20

1.4 Production of top at the Tevatron 21

1.5 Decay Modes for top 24

1.5.1 $e\mu$ Channel 26

1.6 The State of Affair 27

2 The Donut Machine: Tevatron **30**

2.1 Accelerator Overview 30

2.2 The Colliding Beams 32

3 The DØ Detector **37**

3.0.1 Overview of DØ 38

3.1 Tracking System 41

3.1.1 Drift Chamber "Principles of Operation" 43

3.1.2 Vertex Chamber 44

3.1.3 Transition Radiation Detector 47

3.1.4 Central Drift Chamber 48

3.1.5 Forward Drift Chambers 50

3.1.6 Tracking Electronics and Readout 53

3.2 Calorimeter 53

3.2.1 Principles of Operation 54

3.2.2 Central Calorimeter 57

3.2.3 Endcap Calorimeter 59

3.2.4 ICD and MG Detectors 59

3.2.5 Calorimeter Electronics and Readout 60

3.2.6 Calorimeter Response and Resolution 62

3.3 Muon System 63

3.3.1 WAMUS and SAMUS Systems 66

3.3.2 Muon Scintillator Coverage 69

4 From Haystack to the Needle **72**

4.1 Trigger System 72

4.1.1 Level 0 73

4.1.2 Level 1 75

4.1.3 Level 2 78

4.2 Host System 79

5 Reconstruction and Identification **80**

5.1 Interaction Point 81

5.2 Jet Reconstruction 82

5.3 Missing Energy Reconstruction 84

5.4 Electron Identification 85

5.5 Muon Identification 90

5.6 Corrections 93

5.6.1 Electron Energy Corrections 93

5.6.2 Jet Corrections 93

5.6.3 Missing E_T 95

6 Modelling Signal and Backgrounds **98**

6.1 Event Simulator 99

6.2 Detector Simulator 101

6.3 Trigger Simulator 103

6.4 Fine Tuning 104

6.4.1 Musmear 104

6.4.2 Noisy 105

6.5 Signal MC 106

6.6 Background MC 107

6.6.1 Physics Backgrounds 107

6.6.2 Instrumental Backgrounds 109

7 Estimations and Expectations **111**

7.1 Input Efficiencies 112

7.1.1 Electron Efficiencies 112

7.1.2 Muon Efficiencies 115

7.1.3 Trigger Efficiencies 117

7.2 Selection Cuts 117

7.3 Acceptances for $t\bar{t} \to e\mu$ 124

7.4 Background Estimation 127

8 Collider Data Analysis **130**

8.1 Data Sample 130

8.2 Triggers 132

8.3 Offline Event Selection 132

8.4 Anything Interesting 133

8.5 Summary of $e\mu$ analysis 134

8.5.1 Cross Section from $e\mu$ Channel 139

8.6 Conclusions 140

8.7 Final Remarks 142

BIBLIOGRAPHY **144**

List of Tables

1.1 The Standard Model picture of fundamental particles 9

1.2 Decay modes from Ws for a $t\bar{t}$ pair. 24

3.1 The DØ VTX chamber parameters. 47

3.2 Central Drift Chamber Parameters. 50

3.3 Forward Drift Chamber Parameters. 52

3.4 Central Calorimeter Parameters. 58

3.5 Endcap Calorimeter Parameters. 60

3.6 Muon System Parameters. 69

7.1 Electron efficiencies for CC and EC. 114

7.2 Muon efficiency correction factors for CF and EF. 116

7.3 Trigger efficiencies. 117

7.4 $e\mu$ selection cuts. 118

7.5 Acceptances for $t\bar{t} \to e\mu$ production. 124

7.6 Systematic errors. 125

7.7 $\sigma_{t\bar{t}}$ and number of top events expected from 76.6 pb^{-1}. 127

7.8 Number of physics background events from 76.6 pb^{-1}. 127

8.1 Level 2 Triggers used in run 1b. 132

8.2 Number of data events passing each level of selection cuts. 133

8.3 Details of the two $e\mu$ candidates from run 1b. 138

8.4 $e\mu$ final summary for run 1b. 139

8.5 Measured $\sigma_{t\bar{t}}$ from the $e\mu$ channel. 140

8.6 Run 1a+1b top search results for dilepton, lepton + jets and lepton + jets with μ-tag channels (errors include correlations between channels). . 141

8.7 Summary of 1a+1b top search results. 141

List of Figures

1.1 The SM relationship between top mass and W mass, for different Higgs masses. The LEP Z mass of 91.187 GeV/c^2 is used here. The shaded band indicates a W mass of $m_W = 80.22 \pm 0.26$ GeV/c^2. 14

1.2 A fermion (quark or lepton) triangle diagram which could cause an anomaly. 16

1.3 Examples of weak processes that give $B^0 \leftrightarrow \bar{B}^0$ transitions. 17

1.4 Hypothetical b-quark decay by mixing with lighter quarks. 18

1.5 Another possible b decay if the mixing decay exists. 19

1.6 Diagrams contributing to the production of $b\bar{b}$. 20

1.7 Lowest order QCD diagrams for $t\bar{t}$ production. 21

1.8 Production cross section for top at the Tevatron (this NLO exact cross section includes the soft gluon resummation). 23

1.9 The $e\mu$ decay channel. 26

2.1 The general layout of the collider facility at Fermilab (not to scale) . . . 31

3.1 Cutaway view of the DØ Detector. 39

3.2 Side view of the DØ Tracking System. 42

3.3 End view of one quadrant of the DØ VTX chamber. 45

3.4 End view of three CDC modules. 49

3.5 One of the two sets of the FDCs. 51

3.6 Schematic view of a DØ calorimeter cell. 56

3.7 Isometric view of the DØ Calorimeter. 57

3.8 Side view of the calorimeter segmentation. 61

3.9 Elevation view of the DØ detector showing the muon system. 64

3.10 Detector thickness (in interaction lengths) as a function of polar angle. . 65

3.11 Aluminium extrusion cells forming the muon PDTs. 66

3.12 Two separate electrodes comprising the PDT cathodes. 67

3.13 A Muon Scintillation Counter (not to scale). 71

4.1 Block diagram of the DAQ/Trigger System. 74

5.1 H–matrix χ^2 and isolation (f_{iso}) distribution. (a) & (c) are for $Z \to ee$ events. (b) & (d) are for EM clusters in inclusive jet data. 89

5.2 Track match significance and track ionization (dE/dx) distribution. (a) & (c) are for $Z \to ee$ events. (b) & (d) are for EM clusters in inclusive jet data. 91

5.3 Jet E_T correction factors for 0.5 cone jets. 96

7.1 (a) $\not\!\!E_T^{cal}$, (b) H_T, (c) number of jets ($E_T > 20$ GeV), (d) $1/p_T^{\mu}$ Vs E_T^e distributions for top180 MC (after the e, μ id and muon isolation requirements). 121

7.2 (a) $\not\!\!E_T^{cal}$, (b) H_T, (c) number of jets ($E_T > 20$ GeV) distributions for $Z \to \tau\tau \to e\mu$ background. 122

7.3 (a) $\not\!\!E_T^{cal}$, (b) H_T, (c) number of jets ($E_T > 20$ GeV) distributions for $WW \to e\mu$ background. 123

7.4 Acceptance (boxes) and Expected event yield (rhombuses)Vs M_{top}. . . . 126

7.5 Laenen *et al.* $\sigma_{t\bar{t}}$ central value Vs M_{top}. 126

8.1 $1/p_T^{\mu}$ Vs E_T^e plot after the final cut. 134

8.2 DØ end-view of event 12814. 135

8.3 $\eta - \phi$ lego plot of event 12814. 135

8.4 $\eta - \phi$ lego plot of event 26920. 136

8.5 $r - z$ view of event 26920. 136

8.6 EM Shower profile of e in event 12814. 137

8.7 EM Shower profile of e in event 26920. 137

8.8 DØ top cross section. 142

Chapter 1

Introduction

Recently the discovery of the top quark has been announced by the DØ and CDF collaborations [1, 2]. Top quark being one of the missing pieces of the Standard Model of particles (section 1.2), its discovery is a great step forward in our understanding of the existence of both microscopic and macroscopic forms of matter though the fundamental question "what is the cosmos made up of?" still remains.

This thesis presents the details of an analysis performed for the top search. The outline of the thesis is as follows. The current chapter gives a summary of particle physics focusing on the major role of the top quark, and discusses its production and decay modes. Chapter 2 briefly describes the Fermilab Tevatron as a part of the experimental setup. In chapter 3, the DØ detector, i.e. the experimental apparatus used to look for the top quark, is described. Chapter 4 summarizes the process of obtaining the data used for the present analysis. Next in chapter 5, we discuss the algorithms used to identify objects such as jets, leptons, etc. Chapter 6 describes the event simulators and how we differenciate between the top signal and the related backgrounds. The estimations from

both signal and the backgrounds are described in chapter 7. Next in chapter 8, we look into real data for any top signal, concluding with the final DØ top search results and the future aspects.

1.1 Overview of particle physics

The physical world we see around us is just a combination of matter and light. For millennia scholars have talked about the constituents of this "matter" and by 1900 most scientists got convinced that all matter was made up of a number of different sorts of atoms. At present we have a much clearer picture of matter, with quarks and leptons being the most fundamental units of matter known to us. Particle Physics is the science exploring these fundamental units of matter and the interactions between them. These interactions are believed to be of four kinds with which all the known particles interact: gravitational, electromagnetic, weak and strong.

The gravitational force is described classically by Newton's famous inverse square law but since the early part of this century this force has been more precisely described by Einstein's *General Theory of Relativity* [3]. In general relativity the force of gravity is reduced to the curved geometry of space-time. Still general relativity is a classical theory; it does not account for gravity in the quantum-mechanical regime. Quantum mechanics, itself, came into existence in the 1920's as Schrödingers wave equation modelled the hydrogen atom successfully from a probabilistic viewpoint and Heisenberg's uncertainty principle paved the way to the formulation of operator algebra of physical observables. In 1927, Dirac combined the special theory of relativity and quantum mechanics into

relativistic quantum mechanics. This theory predicted the existence of antiparticles.

Boltzmann's pioneering work on statistical mechanics was soon adapted into the framework of quantum mechanics. A broad classification of all the particles came into existence depending on how the momentum is distributed amongst the particles of the ensemble. Fermi-Dirac statistics describes the momentum distribution for the electrons, protons, etc., having half-integral spins. Such particles obey Pauli's exclusion principle which restricts the acquisition of the same momentum state by two similar spin half-integral particles and are called *fermions*. Particles with integral spins are called *bosons* as they obey Bose-Einstein statistics. Any number of bosons can acquire the same momentum state thus the exclusion principle is not valid for them.

In the 1860's Maxwell combined the observations of Faraday and others into a single theory known as the *Classical electromagnetic theory* [4] as it explained the two separate phenomena of electricity and magnetism. In 1920's and 30's, Dirac, Heisenberg, Pauli and others extended Maxwell's theory to include the concepts of special relativity and quantum mechanics and thus gave the first theory of *Quantum electrodynamics* (QED) [5]. This theory gave meaningful results only when calculated to the lowest order in perturbation theory. Higher-order corrections in QED led to divergent integrals. These divergences (or infinities) reflected our ignorance concerning the small-scale structure of space-time. For $x \to 0$, or, in momentum space, as $k \to \infty$, the integrals in QED became divergent. In 1949, Feynman, Schwinger and Tomonaga showed how to extract meaningful physical information from QED by introducing the concept of renormalization. In this renormalization theory, the divergent integrals were absorbed into an infinite rescaling of the coupling constants and masses of the theory thus overcoming the infinite contributions to the perturbation series [6].

After these successes, some failures of the electromagnetic interactions surfaced! The source of radioactive β-decay and the mechanism holding the protons together inside a nucleus were unknown within the framework of QED. Explaining the continuous spectrum for β decay, to avoid the violation of energy conservation, Pauli in 1930 postulated an invisible particle called *neutrino*. In 1934, Fermi came up with the first theory of the *Weak interactions* to explain the nuclear β decay [7]. This theory was developed in close analogy with the theory of QED. Elementary particle interactions have been classified into five types: scalar(S), vector(V), tensor(T), pseudoscalar(P) and axial vector(A). These indicate the allowed ways for one particle's wave function to transform into another during an interaction while satisfying the constraints of both relativity and quantum mechanics. QED, for example, is a vector(V) interaction, implying that the transition from one wave function to another is always accompanied by the creation of a virtual particle, the photon, which has a spin of one and negative parity. So the photon is a vector particle [8]. Fermi's new theory being similar to QED was also a vector interaction. However, it failed to explain some of the experimental results (Gamow-Teller transitions).

On the other hand, in attempting to describe the features of the strong nuclear force, in 1935 the Japanese physicist H. Yukawa proposed that the nuclear force between protons is mediated by a massive particle pi-meson or pion, denoted by π, in contrast to the massless photon mediating the infinite-range electromagnetic force. The effective range of the strong force (10^{-15} m) gives a pion mass of about 150 MeV. In 1937, five years after his discovery of the positron, Anderson observed yet another particle in the cloud chambers originating from cosmic rays. This particle, at first thought to be the Yukawa mediator, was found to exist in both +ve and -ve states with a mass of about

106 MeV. The non-interactive nature of this particle with the atomic nuclei (means no strong interaction) in the earth's atmosphere, as it could make it all the way to the cloud chamber, forced theorist to discard it to be a pion and was named the *muon* (μ). If Yukawa's pion is to interact strongly with atomic nuclei, it is hard to expect it to penetrate the entire atmosphere without getting absorbed! So, in 1947 C. Powell and company took photographic plates to a mountain top to reduce the distance which the pions traversed and discovered Yukawa's pion, which quickly decays into a muon. During the same year, in 1947, two British physicists, Rochester and Butler, observed more new particles, which were named *strange* particles because of their anomalous behavior. They were observed to indicate production via strong nuclear force, say between two protons, or a pion and a proton, with a typical expected decay time of the order of a strong force ($\sim 10^{-23}$ s). But, the measured track lengths gave their average lifetimes at about 10^{-10} s, the time scale typical of weak interaction processes. In 1952, A. Pais gave the first explanation for this behavior. He suggested that the strange particles could not be produced singly by the strong interaction, but only in pairs (*eg.* $\pi^- + p \rightarrow \Lambda^0 + K^0$). In that same year Gell-Mann and Nishijima proposed a new *strangeness* conserving law, which applies only to the strong interaction. Each particle is assigned a quantum number of strangeness, in addition to its quantum numbers of spin, intrinsic parity and isospin [9, p. 49-56].

By 1960, hundreds of so-called elementary particles were observed in a number of scattering experiments with well-defined values of various quantum numbers. So the most urgent task for physicists of that time appeared to be to have some sort of classification scheme for all these particles. Well, the first scheme was proposed in 1961 by Gell-Mann and Ne'eman, which provided an internal symmetry group for the

classification. The starting point of this symmetry group is the charge independence of the strong nuclear force based on the concept of isospin. This isospin is analogous of spin in an abstract charge space. This all means that to the strong force protons and neutrons are the same entity (which are up and down isospin components of a single nucleon). This indifference can be expressed as the invariance of strong interactions to rotations in the isospin space. The group of transformations which achieves these rotations is the Special Unitary group of dimension 2 called $SU(2)$. Later on, a more upto date scheme, with a larger symmetry group, $SU(3)$, was proposed by Gell-Mann and Zweig. The transformations of the $SU(3)$ group generate many dimensional representations (multiplets), the assignment of hadrons to the multiplets thus led to the prediction of a new hadron Ω^- in 1962 which was discovered in 1964 thus validating $SU(3)$ as the fundamental representation group.

The principle of gauge invariance is perhaps the most significant of the concepts used in modern particle theories, as it is the origin of the fundamental forces themselves! Gauge invariance was first generalized to the isospin invariance of the Lagrangian (describing the interaction of particle wave functions) by Yang and Mills in 1954 and Shaw in 1955, which was later generalized to any theory with a local non-Abelian (meaning that the transformations does depend on the order of operation) gauge invariance. In 1956, T.D. Lee and C.N. Yang pointed out, after the 1950s famous $\tau-\theta$ puzzle, that there was as yet no evidence for "parity" conservation by the weak force. Within months, Wu and Ambler conducted the famous Co^{60} experiment to verify the parity violating nature of the weak interactions. In this experiment radioactive β-decay of Co^{60} into Ni^{60} was studied by putting a magnetic field around cobalt. This enabled Wu *et al.* to measure the emission of β-decay electrons along or against the orientation of nuclear spin (same

as the orientation of magnetic field). The measured electron emission asymmetry with respect to the magnetic field direction in this decay process and its mirror-image were found to be distinguishable from each other. This implied that the weak force did not conserve parity [9, p. 67-70]. Even this could not stop someone from saying that God was weakly left-handed!

To account for the parity violating effects of the weak interactions, Feynman and Gell-Mann, and independently Marshak and Sudarshan, in 1956, proposed that the interaction is a mixture of vector(V) and axial-vector(A) quantities. This led to the first theory of "weak interactions". In 1961, Glashow unified the electromagnetic and weak interactions into a single framework and based on that in 1967 Weinberg and Salam showed how the weak gauge bosons could acquire mass without spoiling the renormalizability (proved by 't Hooft in 1971). During the decade 1973-1983, many experiments confirmed the Glashow-Weinberg-Salam model's predictions. This began with the discovery of neutral currents in 1973 and finally the most spectacular confirmation came as the discovery of $W^{\pm}$ and Z bosons in 1983 which established the gauge-theory structure of the weak interactions. Works of Gell-Mann, Gross, Wilczeck and Politzer resulted in the first and almost complete version of a non-Abelian gauge theory of strong interactions, called by Gell-Mann *Quantum Chromodynamics*, in 1972.

1.2 The Standard Model: A Brief Picture

The *Standard Model* (SM) is the mathematical theory describing the structure of matter in terms of the fundamental particles. The SM or more precisely the *minimal*

SM has been tested against the experimental results to a very good precision. As we talk about the structure of matter and the SM, and gravity being a major force to hold this matter together, we leave the gravitational force out of it (see previous section). Since the SM is a theory of interacting quantum fields, and gravity is a classical theory with some ongoing attempts to quantize it, so gravity is out of the picture.

The SM of particle physics emerged in 1973 just after the development of the Glashow-Weinberg-Salam electroweak model and the development of Quantum Chromodynamics. Basically the SM is the synthesis of electroweak theory and QCD broken symmetry. Further, the SM's description of the matter is only in terms of two kinds of fundamental fermions: quarks and leptons. Both the quarks and the leptons are structureless and point like on a scale of 10^{-17} m. These fermions interact by the exchange of gauge bosons (or field quanta). Table 1.1 gives the classification of fundamental particles of the Standard Model.

Both the leptons and the quarks can further be grouped into three *generations* (or families). The flavors of quarks are arranged in the following three doublets:

$$\begin{bmatrix} u \\ d \end{bmatrix} \begin{bmatrix} c \\ s \end{bmatrix} \begin{bmatrix} t \\ b \end{bmatrix}.$$

The three leptons generations are:

$$\begin{bmatrix} \nu_e \\ e \end{bmatrix} \begin{bmatrix} \nu_\mu \\ \mu \end{bmatrix} \begin{bmatrix} \nu_\tau \\ \tau \end{bmatrix}.$$

Each successive generation is simply a heavier version of particles with the same basic quantum numbers. An interesting thing to keep in mind is that the observable

Particle Type	Name (symbol)	Charge (e)	Mass
Quarks	up (u)	$+\frac{2}{3}$	$\approx$ 5 MeV/c^2
($spin = \frac{1}{2}$)	down (d)	-$\frac{1}{3}$	$\approx$ 10 MeV/c^2
	strange (s)	-$\frac{1}{3}$	$\approx$ 200 MeV/c^2
	charm (c)	$+\frac{2}{3}$	$\approx$ 1500 MeV/c^2
	bottom (b)	-$\frac{1}{3}$	$\approx$ 4500 MeV/c^2
	top (t)	$+\frac{2}{3}$	$\approx$ 145 - 200 GeV/c^2
Leptons	electron (e)	-1	0.511 MeV/c^2
($spin = \frac{1}{2}$)	electron neutrino (ν_e)	0	$<$ 7 eV
	muon (μ)	-1	105.7 MeV/c^2
	muon neutrino (ν_μ)	0	$<$ 0.27 MeV/c^2
	tau (τ)	-1	1777 MeV/c^2
	tau neutrino (ν_τ[1])	0	$<$ 31 MeV/c^2
Gauge Bosons	photon (γ)	0	0
($spin = 1$)	W	1	80.2 GeV/c^2
	Z	0	91.2 GeV/c^2
	gluons (g_i(i = 1...8))	0	0
Higgs($spin = 0$)	H^0	0	?[2]

Table 1.1: The Standard Model picture of fundamental particles

universe (or non-exotic normal matter) is made of u, d quarks, electrons, and ν_e's (i.e. the first generation only), and the gauge bosons. The rest of the particles (2nd and 3rd generations) have been made at accelerators (including the latest addition of the "top" quark) or occasionally by collisions of energetic cosmic rays in the earth's atmosphere, and also presumably existed at the beginning of the universe (just after the BIG BANG).

[1] not definitively observed.

[2] Higgs yet to be discovered.

The three leptons generations consist of both charged and neutral particles (neutrinos) and these interact through the electromagnetic and the weak forces. Quarks, unlike leptons, interact via strong interactions in addition to the weak and electromagnetic interactions. This additional feature of quarks is accounted for by the *color* charge they carry. This color charge is responsible for the strong interactions which the quarks undergo (more details later).

One can ask why Nature chooses to repeat itself like this and whether any more generations remain to be discovered. The answers to these questions are still not known. Each of the quarks, leptons and the gauge bosons (see previous table) has an associated antiparticle, with the same mass and spin but opposite charge. Thus the antiparticle of the electron e (or e^-) is positron (or e^+). The antiquarks are denoted as $\bar{u}$, $\bar{d}$, etc. The antiparticle of the W^+ is the W^-. The photon, Z, and gluon are identical to their antiparticles. Another thing to be noted at this point is that the masses of the six quarks in table 1.1 refer to the "free"-quark masses but these can also be expressed as "constituent"-quark masses and are evaluated at 1 GeV (when the quark masses are smaller than the typical hadronic masses of 1 GeV/c^2). In similar way, neutrino masses are not yet been measured; they are consistent with zero in the SM (table 1.1 gives the present limits).

Now we know about the particles we are dealing with in the SM. The next thing to look into is how these particles in 3 families interact to give the structure to the matter we observe in the universe. It should be emphasized that the photon, $W^{\pm}$, Z, and gluons are actually responsible for the mediation of interactions among these families of particles. These particles are spin 1 particles (see table 1.1) and are called *gauge bosons* as they arise from the gauge theories (more precisely a quantum field gauge theory)

describing the interactions. These theories connect the dynamics of the interaction to the symmetry principles and conservation laws followed by that interaction. In other words, these theories couple the mediator boson's field, of a particular force, to the fields of all the particles which "feel" that force. In particular, the electromagnetic force is mediated by the massless photon, the weak force by the "massive" W and Z bosons, and the strong force by the massless colored gluons (numbering eight).

In the SM all the interactions are derived from a "gauge principle". We will discuss this gauge principle for the simplest case of electromagnetic interaction. Firstly, the symmetry operations (or transformations) on objects in the theory, which leave the physical laws unchanged, are called invariants of the law. Now consider a matter system originally invariant under a global $U(1)$ group of gauge transformations. We "gauge" this symmetry, i.e. enlarge it to a local $U(1)$ gauge invariance. This means that an independent $U(1)$ gauge group shall be associated with each space-time point. To do this it is necessary to introduce a vector gauge field, to which the matter field current becomes coupled. The coupling constant is the electric charge, the generator of $U(1)$. The original global symmetry can be gauged only if it is an exact symmetry. In the SM framework, the symmetries to be gauged refer to transformations among massless quarks and leptons of definite chirality[3].

In the standard model, instead of $U(1)$, the gauge group is now a larger group of transformations that mix the different components of the matter field. There will now be more than one gauge field–the Yang-Mills fields. Their number is equal to the number of generators of the gauge group. The relevant group for the weak, electromagnetic, and

[3]Chirality is defined as the eigenvalue of γ_5, with $\gamma_5 = 1$ corresponding to right-handedness, and γ_5 = -1 to left handedness [10].

strong interactions is $SU(2) \times U(1) \times SU(3)$. So, the gauge group is a direct product of the three mutually commuting groups defined below as the internal symmetries:

- **Color SU(3):** With respect to the color index (n=1,2,3), the three quarks of each flavor form a triplet representation of a "color group" $SU(3)$. (The leptons are color singlets.)
- **Weak isospin SU(2):** In each family, the left-handed components of the upper and lower particles (e.g., ν_L and e_L) form a doublet representation of a "weak isospin group" $SU(2)$. All right-handed particles are $SU(2)$ singlets.
- **Weak hypercharge U(1):** There is a $U(1)$ symmetry, called "weak hypercharge", associated with simultaneous phase changes of each particle. The relative phases are fixed by definite "weak hypercharge" assignments.

Gauging this direct product group necessitates the introduction of 12 vector gauge fields, one for each group generator, as listed in table 1.1.

The gauge fields generally have self-interactions because, unlike the photon, they generally carry "charge" by virtue of the non-Abelian nature of the group. It is to be noted that there are other exact symmetries of the theory, such as baryon number and lepton number, which are not gauged.

The theory so far has a serious defect, namely, all particles are massless. One cannot remedy this by simply including conventional mass terms in the Lagrangian, because such terms violate the $SU(2) \times U(1)$ symmetry, which we assume to be exact. Conventional vector boson mass terms also lead to non-renormalizable theories. A way

out is to regard the masses as arising from "spontaneous breaking" of the $SU(2) \times U(1)$ symmetry, through couplings to scalar "Higgs fields". The quarks and leptons also acquire masses through this mechanism, called the Higgs mechanism. If this prescription for acquiring masses is correct, the Higgs should appear as a real, observable particle (whose existence is yet to be confirmed experimentally). One way to close down on the Higgs is using the fact that the top mass, the Higgs mass, and the ratio of the W and Z masses [11] are interrelated, as shown in Figure 1.1 [12]. As is clear, the dependence on the Higgs mass is weak (logarithmic) and only a precise measurement of the top mass can significantly constrain the mass range the for Higgs.

Since mass and chirality do not commute, physical particles are not necessarily members of $SU(2) \times U(1)$ multiplets. This leads to a mixing of flavors across families. The electroweak interactions that result from gauging $SU(2) \times U(1)$ reproduce electroweak phenomena and predict new ones (see section on introduction).

On the other hand, color multiplets are mass eigenstates, because right and left-handed quarks can have the same color. Experimental evidence indicates that color $SU(3)$ does not suffer spontaneous breakdown. Due to the structure of color $SU(3)$, the quark-gluon coupling tends to vanish at large momenta (or small distances)–a phenomenon known as "asymptotic freedom". Thus, one should be able to detect quasi-free quarks inside a hadron by using probes that impart large momentum transfers to quarks. The quark-gluon coupling tends to grow as the momentum scale decreases, leading to very strong interactions at energies below ≈ 0.5 GeV. It is believed that these interactions lead to "quark confinement". That is, quarks (and gluons) cannot exist in isolation as physical states, but occur only as components of color-neutral bound states (hadrons).

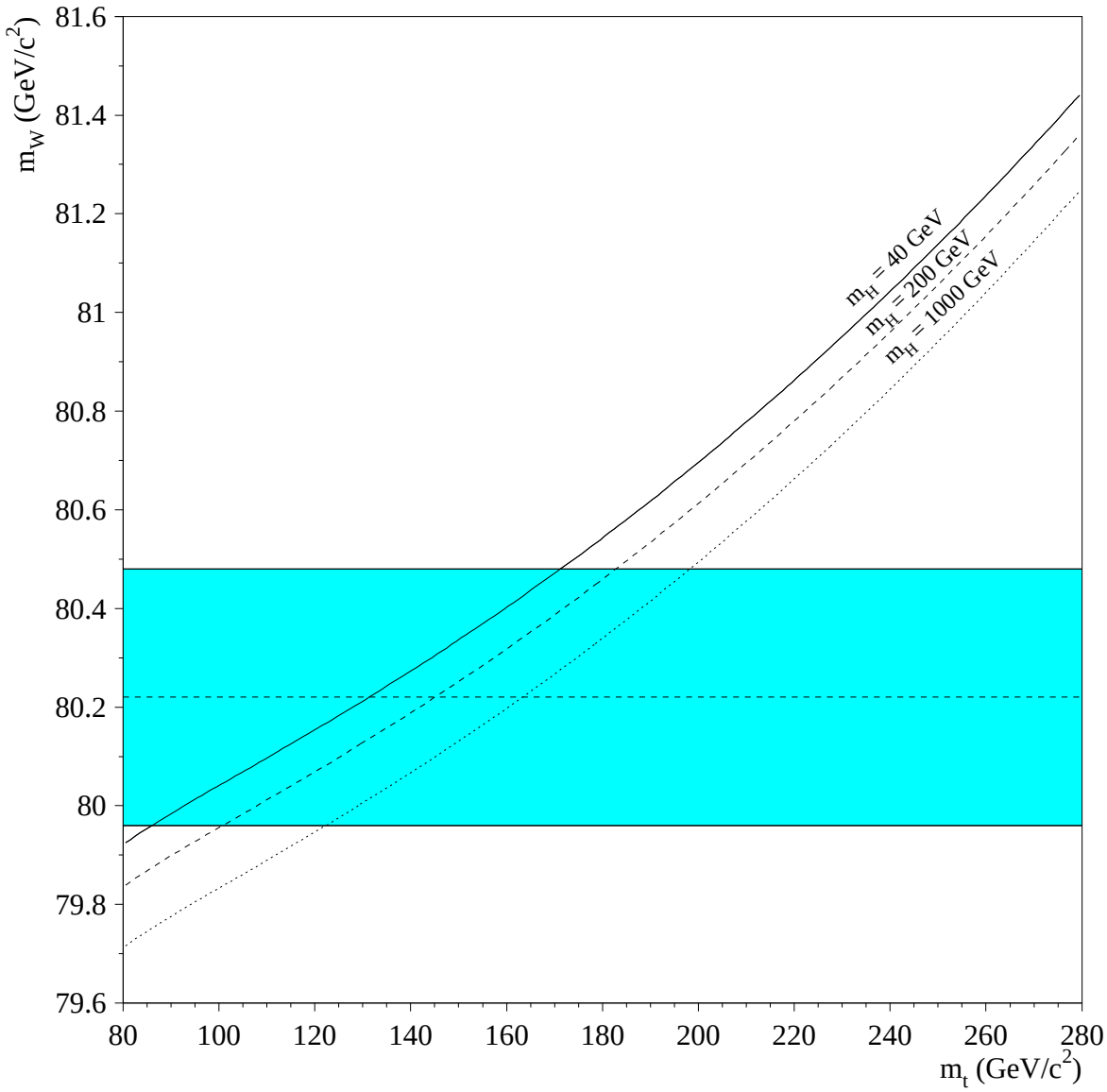

Figure 1.1: The SM relationship between top mass and W mass, for different Higgs masses. The LEP Z mass of 91.187 GeV/c^2 is used here. The shaded band indicates a W mass of $m_W = 80.22 \pm 0.26$ GeV/c^2.

The Standard Model has withstood all experimental tests in the decades since it took shape. All the gauge bosons have been discovered at the masses predicted by theory. It has opened our eyes to theoretical ideas like vacuum structures and topological excitations, which have found applications in cosmology and condensed matter physics.

1.3 Top Quark

After the firm establishment of the existence of five quark flavors (d, u, s, c, *and* b), the hunt was on for the sixth flavor, the top quark. Existence of the top quark could be inferred from the $SU(2)$ symmetry group in the Standard Model. Outside the SM, the empirical observation of the fermion (both quarks and leptons) generations gives an idea about the constituent quarks (and hence top) in the 3 families and moreover the doublet structure requires that the t quark is needed to complete the third generation. Now, there is good experimental evidence for the existence of the top quark with sound theoretical backing as discussed in the following sections.

1.3.1 Is it "truth"?

The most compelling evidence that there is "top" comes from the SM's description of b quark interactions. The very existence of the b quark, as predicted by Kobayashi and Maskawa in 1973, along with the top, and later the discovery of b quark just strengthened the $SU(2)$ symmetry structure of the SM. As discussed earlier, the b quark forms an $SU(2)_L$ doublet with the top quark (as is the case with the two lower generations), i.e. the b quark has the third component of isospin, T_3 = -1/2 and hence should have an

isospin partner with $T_3 = 1/2$. In the following sections the circumstantial evidence for the existence of the top quark becomes stronger and stronger (with some anomalies too, and with the recent discovery announcements confirming the existence). We will start with the anomalies first.

1.3.2 Anomalies

An anomaly is the failure of a classical symmetry to survive the process of quantization and renormalization. For example, in a chiral gauge theory, we naively expect axial currents to be conserved. However, we find that actions that are classically chiral symmetric can develop anomalies that spoil the conservation of the axial current. Specifically, we will examine the "triangle graph", which consists of an internal fermion loop connected to two vector fields and to one axial vector field as in figure 1.2. This is called the V-V-A triangle graph [13, p. 15,65]. Each triangle is proportional to $c_A^f Q_f^2$,

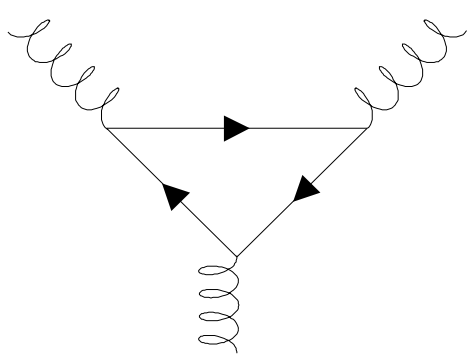

Figure 1.2: A fermion (quark or lepton) triangle diagram which could cause an anomaly.

where Q_f is the charge and c_A^f is the axial coupling of the weak neutral current [14]. The renormalization gauge theory requires a delicate cancelation between such diagrams consisting fermion loops. For an equal number N of lepton and quark doublets, the total anomaly is proportional to

$$\sum_{i=1}^{N}\{\frac{1}{2}(0) - \frac{1}{2}(-1)^2 + \frac{1}{2}N_c(+\frac{2}{3})^2 - \frac{1}{2}N_c(-\frac{1}{3})^2\} = 0. \tag{1.1}$$

Thus taking into account of the three colors of each quark ($N_c = 3$), the anomalies are canceled, i.e. taking top quark's existence into account would lead to an anomaly free gauge theory. This implies that without the top quark it is likely to have an anomaly.

1.3.3 $B^0 - \bar{B}^0$ Oscillations

Weak interactions do not conserve quark flavors and can mix B^0 with $\bar{B}^0$ states, for example by box diagrams like figure 1.3, with closed internal quark lines. The observed

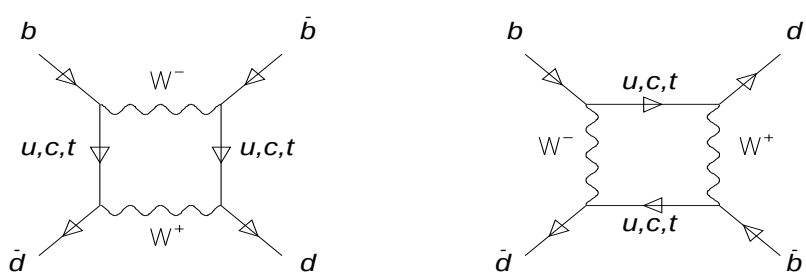

Figure 1.3: Examples of weak processes that give $B^0 \leftrightarrow \bar{B}^0$ transitions.

rate of this mixing goes as $|V_{td}|^2$ (CKM matrix element [15]), so top is needed in the

loops, in fact, a fairly heavy top is needed in the SM to explain the observed level of $B^0 - \bar{B}^0$ mixing. However, other contributions can compensate for the needed model stability, so this is not unique in general and hence not conclusive.

1.3.4 b Decays

In the SM the b quark decays occur through quark mixing [16, chap. 22], and the allowed vertices are $b \to c{+}W^-$ and $b \to u{+}W^-$. They are proportional to the elements V_{bc} and V_{bu} of the CKM matrix. This means that the b has to be in a doublet, allowing the top to exist.

Consider that b is an $SU(2)_L$ singlet. In this case b would have no interactions with $W^{\pm}$, i.e. it cannot decay via charged current. Since it does decay in this way, the only decay mode requires mixing with the lighter quarks (see figure 1.4) s and d (which are doublet and interact as usual through a virtual W, $b \to l^+\nu X$). In that case, the process

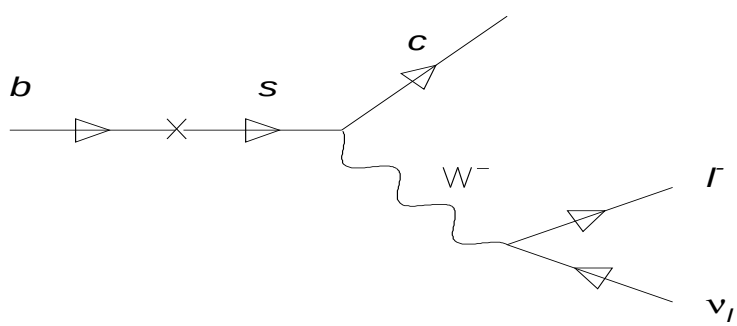

Figure 1.4: Hypothetical b-quark decay by mixing with lighter quarks.

involving a Z would also be present as shown in figure 1.5 ($b \to l^+l^-X$), with a cross section of atleast 12% of the mixing (first) process [16, chap. 25]. The experimental upper limit on this ratio is several orders of magnitude below this value. So the b quark does not have a weak isospin of 0 (that is, it is not a **singlet**). Further more, in the SM regime nothing can decay to lighter states via its interactions with Z, the decay of b quark into lighter s and d quarks requires the existence FCNC (flavor changing neutral current, e.g. $s \to d$). FCNC is suppressed for doublet quarks by the GIM mechanism which requires all left- and right-handed components of the same charge (here s and d) in different quark families to have the same weak isospin. Thus FCNC suppression implies that the b should have the same weak isospin as others of different doublet generations with the same charge, requiring the doublet partner t to exist.

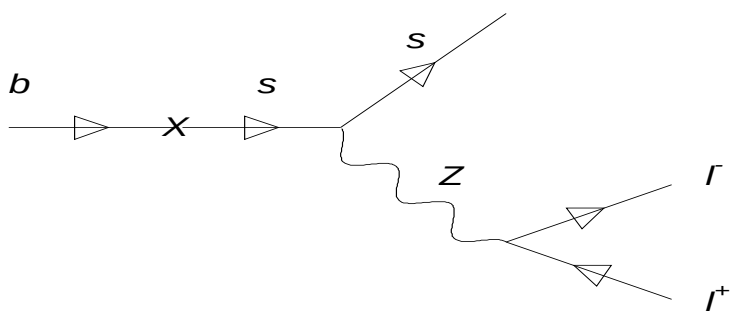

Figure 1.5: Another possible b decay if the mixing decay exists.

1.3.5 A_{FB} in $e^+e^- \to b\bar{b}$

For $e^+e^- \to b\bar{b}$, the two contributions from γ and Z are shown in figure 1.6. An asymmetric angular distribution for b production results because of the presence of Z, whereas this distribution is symmetric for γ alone. The asymmetry, A^b_{FB}, is given by

$$A_{FB} \equiv \frac{\sigma_F - \sigma_B}{\sigma_F + \sigma_B} \tag{1.2}$$

where σ_F and σ_B are the forward and backward cross sections. The amount of this asymmetry in the production is dependent on the third component of the weak isospin of the left-handed b quark (T^b_{3L}), as the coupling of b to the Z is proportional to T^b_{3L} $+\frac{1}{3}\sin^2\theta_w$, where T^b_{3L} is 0 if the b quark is a singlet (topless case) and -$\frac{1}{2}$ if b has its doublet partner–the top quark. A_{FB} and $\Gamma(Z \to b\bar{b})$ measurement results give $T^b_{3L} = -0.504^{+0.018}_{-0.011}$ [16, p. 268]. So, the left-handed b-quark is in a doublet and there has to exist a heavier quark to be its partner, which is the t-quark.

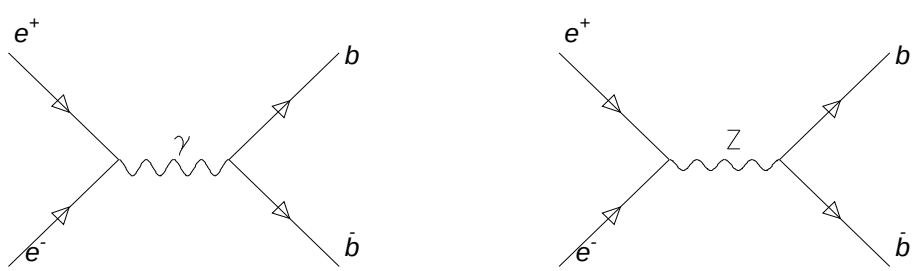

Figure 1.6: Diagrams contributing to the production of $b\bar{b}$.

1.4 Production of top at the Tevatron

The Tevatron (more details in next chapter) is the source for $p\overline{p}$ collisions at $\sqrt{s} =$ 1.8 TeV. At this center of mass energy, the dominant production mode for top is the pair production process, where $q\bar{q} \rightarrow t\bar{t}$ and $gg \rightarrow t\bar{t}$. The leading order (i.e. the lowest order!) QCD Feynman diagrams for these processes are shown in figure 1.7. Out of these two production modes, the gg channel contribution to the total cross section varies with the top mass (m_t), from $\approx$ 50 % for 90 GeV/c^2 top mass to 10 % at m_t = 200 GeV/c^2.

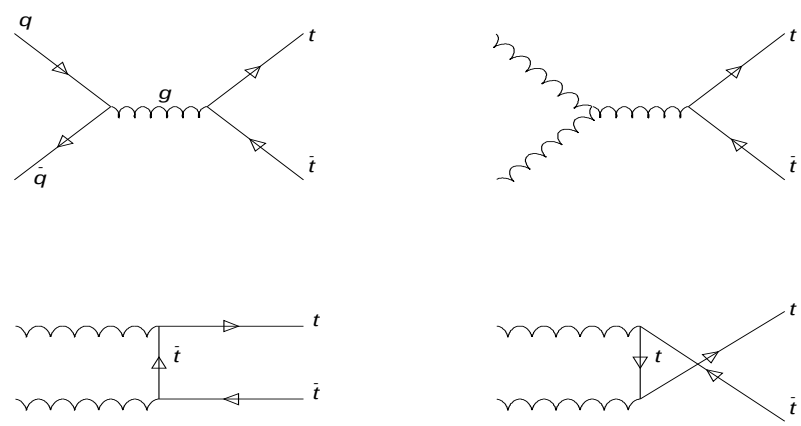

Figure 1.7: Lowest order QCD diagrams for $t\bar{t}$ production.

Until the discovery of the top quark, an estimate of the theoretical cross section for the top production was needed to either determine its mass or to give a lower limit on it so that the experimentally measured top production cross section (or the upper limit on it) could be compared with the theoretical prediction which is calculated as a function of top mass.

This theoretical cross section has been worked out based on the fixed order α_s^2 (leading order or LO) plus α_s^3 (next-to-leading order or NLO) contributions in the perturbative QCD regime. It is expected that the NLO terms contribute less than the LO terms. But, the higher order corrections in the $q\overline{q}$ channel are small, whereas those for the gg channel are of the order on 70 % or larger for top production processes at the Tevatron. For the high mass top search, what the present analysis is about, the qg and $\bar{q}g$ channels have negligible contributions to the top production. For a top mass of 150 GeV/c^2, which is quite high, the NLO terms for the gg channel still contribute about 20 % (even though $q\overline{q}$ is larger).

The source for these large corrections (and hence the difference between LO and NLO) is the initial state gluon bremsstrahlung in the threshold region for heavy quark production. The processes involving these initial state radiations have dominant logarithms which have to be summed to all orders in perturbation theory to calculate the exact contribution. There exists a technique called *resummation* to calculate the sums of these dominant logarithms. Laenen, Smith and van Neerven used this technique to resum the leading and next-to-leading logarithms in perturbative QCD to all orders (for results see [17]). Figure 1.8 gives the total cross section for top pair production as a function of top mass. But, this resummation result is sensitive to the scale at which perturbative QCD breaks down, so the solution is to stop the resummation at some scale μ_0 (since the series being resummed eventually diverges due to nonperturbative effects when α_s becomes large). This newly introduced scale μ_0 should be bounded by the QCD scale λ on the low end and by m_t on the high end (a rough estimate). In figure 1.8, the scales chosen for the central value are $\mu_0 = 0.1m_t$ and $\mu_0 = 0.25m_t$ for the $q\overline{q}$ and gg channels respectively (with $\mu = m_t$).

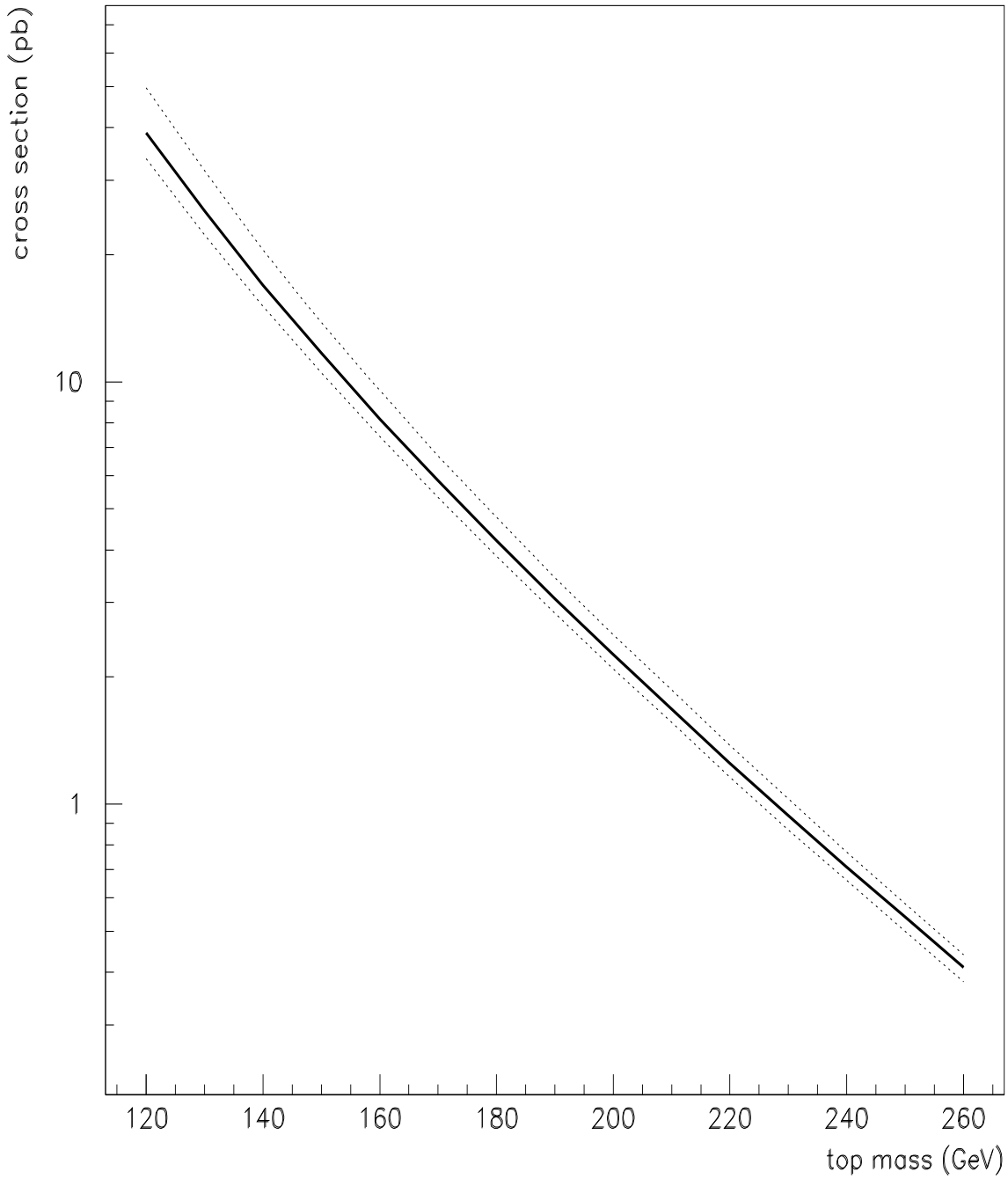

Figure 1.8: Production cross section for top at the Tevatron (this NLO exact cross section includes the soft gluon resummation).

The lower limit curve (lower edge) was determined by taking the soft gluon series out to only one additional term ($O(\alpha_s^4)$) instead of summing the whole series [18].

1.5 Decay Modes for top

In the present analysis we assume the standard model decays for the top quark. If there are only three generations of quarks, the Cabibbo-Kobayashi-Maskawa (CKM) matrix element V_{tb} has a magnitude close to unity, and if the top quark is heavy (> 90 GeV) then the dominant decay mode for top quark is the semiweak process $t \to bW^+$, i.e. top decaying to a b quark and a W. So we do not consider the decay where top quark decays to a charged Higgs (beyond minimal SM). The W will either decay leptonically to a lepton ($l \equiv e, \mu, \tau$) - neutrino (ν_l) or hadronically into a quark-antiquark ($q\overline{q}$) pair. Table 1.2 gives the decay branching ratios for the W to decay into leptons and quarks (assuming quark and lepton universality and three color degrees of freedom for the quarks).

	$W \to e\nu_e$ (1/9)	$W \to \mu\nu_\mu$ (1/9)	$W \to \tau\nu_\tau$ (1/9)	$W \to q\bar{q}$ (2/3)
$W \to e\nu_e$ (1/9)	1/81	1/81	1/81	2/27
$W \to \mu\nu_\mu$ (1/9)	1/81	1/81	1/81	2/27
$W \to \tau\nu_\tau$ (1/9)	1/81	1/81	1/81	2/27
$W \to q\bar{q}$ (2/3)	2/27	2/27	2/27	4/9

Table 1.2: Decay modes from Ws for a $t\bar{t}$ pair.

Since top is very heavy (large phase space available for decay), it has a lifetime

$\tau_t \approx 0.4 \times 10^{-24}$ s, or 0.4 yoctosecond (ys) for a top mass of 175 GeV/c^2 with the partial width [19]

$$\Gamma(t \to bW^+) \approx 1.55 \text{ GeV}. \tag{1.3}$$

So there is no toponium spectroscopy, and indeed no dressed hadronic states containing top! As the top quarks are produced in pairs, and each top decays to Wb, the top decay channels follow the WW decay (see table 1.2) classification. In the following paragraph we will go through, briefly, all the top decay channels.

Referring back to the table 1.2, when both the Ws (horizontal and vertical) decay leptonically, the top events are categorized as *dilepton* events. The branching ratio (BR) for the most favored three channels (ee, $\mu\mu$ and $e\mu$) is only 4/81 (≈ 5 %) (neglecting taus as they are hard to identify). These are however, the cleanest channels, i.e. they have very small backgrounds (especially $e\mu$ as we see in the last chapter). We will discuss more about these dilepton events in the next section. Next we consider the case where only one of the two Ws decays leptonically and the other goes to a quark-antiquark pair. These events are called *semileptonic* or *lepton + jets* events. The branching ratio for one l + jets channel is about 3 times the BR for ee, $e\mu$, and $\mu\mu$. The large BR implies a larger cross section, but the W + jets process is a large enough background to make this channel a more challenging topology. Finally, the channel with the largest branching ratio is the *all-jets* channel, where both of the Ws decay hadronically. Due to the large background from QCD multijet events this channel is still under study.

1.5.1 $e\mu$ Channel

The $e\mu$ channel is the channel in which we looked for the top signal and the details are presented here in this thesis. As discussed in the previous section, the $e\mu$ event topology is defined by the two W decays (from two top quarks, see figure 1.9). Both the Ws decay leptonically, one going into an electron and neutrino and the other to a muon and neutrino. The branching ratio available to this channel can be computed from table 1.2, which is $\frac{2}{81}$ (2.47 %). This BR excludes the τ contributions to the $e\mu$ channel. Since a τ can decay to an electron ($\tau \rightarrow e$) or to a muon ($\tau \rightarrow \mu$), the total BR available to the $e\mu$ channel has to be worked out, which is discussed in chapter 7.

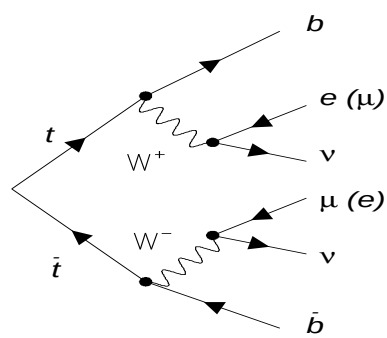

Figure 1.9: The $e\mu$ decay channel.

The "footprints" of such a decay are noticeable from the above figure. The main features which characterize an $e\mu$ event are:

- One high transverse momentum (p_T) electron

- One high p_T muon
- High missing transverse energy ($\not{E}_T$) - from two neutrinos
- Presence of jets from two b quarks

Since the BR for this channel is small, the production cross section for the top is going to be small for the present luminosities ($\sim 5\times10^{30}$ cm^{-2}s^{-1}) at the Tevatron. But, the backgrounds' contribution to this channel is relatively small as compared to the other decay channels (chapter 7). So we expect a smaller, but, cleaner signal in the $e\mu$ channel.

1.6 The State of Affair

Observation of the top quark production was reported a year and half back by the DØ and the CDF collaborations. The next step of determining the top mass is already in progress(chapter 8). In the following paragraphs, we discuss, briefly, the limits put on the top mass and how it affects our understanding of the SM.

The present state of affair, after the observation of top, in the experimental field is to measure the top mass as accurately as possible and thus finally narrow down the window for the Higgs search, the ultimate missing piece of the SM. On theoretical grounds, it's hard to say anything about the masses of new flavors, but consistency requirements give rise to constraints which can lead to some predictions. As the top mass is correlated with the W mass, G_F and other electroweak observables, plus it couples to the Higgs boson, a probable restriction for the $(t,b)_L$ doublet is $|m_t - m_b| \leq 550$ GeV/c^2. Further considering the radiative corrections, as all electroweak amplitudes are affected by them

and which account for the difference between tree level and higher order calculations, top-quark loops contribute to the renormalization of observables ρ ($\equiv M_W/M_z\cos\theta_W$, = 1 for tree level diagrams) as

$$\rho \equiv \frac{M_W^2}{M_Z^2(1-\sin^2\theta_W)}. \tag{1.4}$$

A recent fit to electroweak observables from LEP and SLC's high-precision measurement yields $m_t = 178^{+11+18}_{-11-19}$, assuming the central value $m_H = 300$ GeV/c^2 and the validity of the SM [20].

The first direct limits on the top mass exceeding the threshold for the decay into real W and a b quark came in the early 90's from the Fermilab Tevatron collider: $M_t >$ 91 GeV [21] and $M_t > 131$ GeV [22]. A brief history of the previous top searches can be found in [23]. In 1994, the CDF collaboration announced the first evidence [24] for the top production using the 1992-1993 collider run 1A with a production cross section $= 13.9^{+6.1}_{-4.8}$ pb and m_t of $174\pm10^{+13}_{-12}$ GeV/c^2. The statistical significance of this result was not enough to claim a discovery. Using the 1A data, the DØ collaboration also reported [25] an excess of signal but without much significance to claim anything. The top production cross section of 8.5 $\pm$ 5.1 pb was reported for an assumed top mass of 180 GeV/c^2 for that analysis.

In March of 1995, during the ongoing run 1B, both the collaborations across the Tevatron, DØ and CDF, announced the observation of top quark with the results of good enough statistical significance. A cross section of 6.4 $\pm$ 2.2 pb and a top of mass $199^{+19}_{-21}\pm$ 22 GeV/c^2 was reported by the DØ collaboration, and CDF collaboration's observation citation gave a cross section of $6.8^{+3.6}_{-2.4}$ pb and a mass of 176 $\pm$ 13 GeV/c^2 for top. The latest top mass measurement results are given in chapter 8.

In the following chapters of this thesis, we will go into the details of DØ result for the top search in the $e\mu$ channel.

Chapter 2

The Donut Machine: Tevatron

The Fermi National Accelerator Laboratory is currently the site of the world's highest center-of-mass energy proton-antiproton colliding beam accelerator, the Tevatron. The next upcoming machine on its way is the Large Hadron Collider (LHC) at CERN. It is the Tevatron which produces collisions between protons and antiprotons at a center-of-mass of 1800 GeV ($\sqrt{s}$). The Tevatron is a proton storage ring, composed of superconducting magnets. The ring is filled with bunches of protons and antiprotons, which circulate in opposite directions. The process of filling the ring is quite complicated; major steps are described below along with a brief overview. The references [26, 27] should give enough details to an interested reader.

2.1 Accelerator Overview

The Tevatron collider is the final stage in a series of seven accelerators that are necessary for colliding beams at Fermilab. A Cockroft-Walton pre-accelerator, a linear

accelerator (Linac), and a synchrotron (Booster) operate in series to produce 8 GeV protons for injection into the Main Ring synchrotron. The Main Ring has two purposes: it serves as the final boosting stage for protons and antiprotons before injection into the Tevatron, and it is the source of the energetic protons which are used to create antiprotons when colliding beams are required. In addition, the Antiproton Debuncher and the Antiproton Source are used in collecting and cooling antiprotons for colliding beams. The overall layout of the accelerator complex is shown in figure 2.1. The major

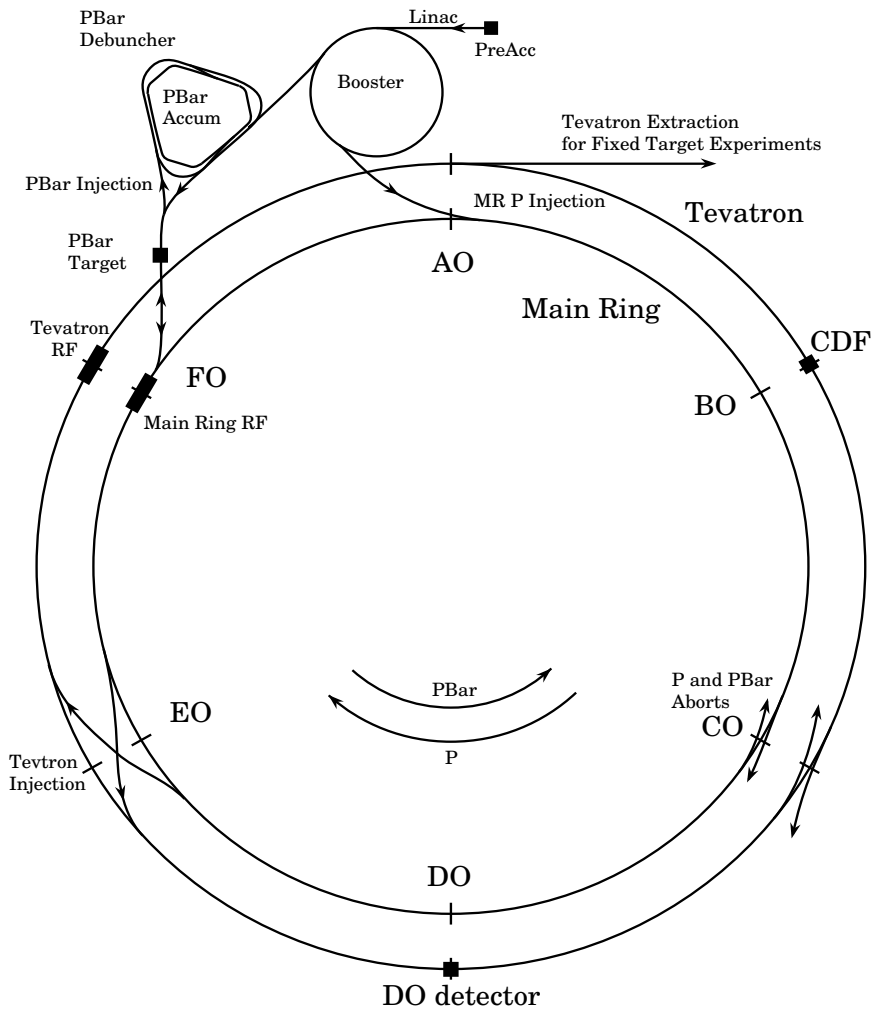

Figure 2.1: The general layout of the collider facility at Fermilab (not to scale)

components of this collider facility are: Preaccelerator (A Cockroft-Walton accelerator),

Linac (A linear accelerator), Booster (A proton synchrotron), Main Ring, Antiproton Source, Debuncher, Accumulator and the Tevatron Ring.

2.2 The Colliding Beams

The beam's birth place, a Cockroft-Walton electrostatic accelerator, is the preaccelerator. The proton beam comes to life as a pulsed 18 KeV H^- ion beam from a magnetron surface-plasma source. These ions are released into the preaccelerator, producing a static electric field to accelerate, where they get accelerated to 750 KeV (after passing through a 750 KV potential). The Femilab preaccelerator operates in a pulsed mode with a frequency of 15 Hz (matching the Linac cycle - more later). The ions coming out of the preaccelerator are bunched using a single gap RF cavity and are transported to the linear accelerator.

The Linac is a two-stage linear accelerator that produces a pulsed beam of 400 MeV H^- ions. The first stage of the 150 meter long Linac, a drift-tube accelerator, accelerates (using oscillating electric field between electrodes) the ions to 116 MeV. The second stage, a new replacement in 1993, is a side-coupled Linac which operates in tandem to accelerate the beam to 400 MeV before their injection (after charge-exchange) into the Booster. The charge-exchange occurs when H^- ions are passed through a carbon foil which strips both the electrons off from the ion and only protons (H^+ ions) are left to be injected into the booster.

The Booster is an 8 GeV fast cycling proton synchrotron which serves as an injector for the Main Ring. A synchrotron is an accelerator where the particles follow a closed

orbit by making use of bending magnets, while being accelerated. Quadrupole focusing fields keep the beam from diverging. RF cavities can be used to increase the energy of the stored particles but this requires that the magnetic fields constraining the particles to their orbits and the RF fields accelerating the particles must vary synchronously with the change in particle momentum. As

$$p = qB\rho \tag{2.1}$$

where p is the particle momentum, q its charge, B the magnetic field and ρ the radius of curvature, it's clear that the maximum particle energy is limited by the strength of the magnetic field and the radius of the ring. The protons coming out of the booster have an energy of 8 GeV.

The next leg of journey for the protons starts as soon as they enter the Main Ring (MR). The Main Ring is a 400 GeV proton synchrotron with a radius of 1000 m. This ring is composed of about 1000 conventional (copper-coiled) magnets. Till 1983, it was the highest energy accelerator in the world, i.e. prior to Tevatron. The MR serves as a 150 GeV injector of protons and antiprotons for the Tevatron as well as a source of 120 GeV protons used in antiproton creation (see below). The MR "captures" the beam (protons only) injected from the booster, accelerates the beam (protons and antiprotons going in the opposite direction) and "coalesces" them into smaller bunches. Once coalescing results in one bunch, cogging is used to align the bunch in th MR for injection into the assigned spot (a RF bucket) in the Tevatron. The MR lies mostly in a plane, except at the B0 and D0 areas where it is vertically out of plane of the circle to accommodate the detectors (the verticle separation at these two over-passes, as they are called, between the MR and the Tevatron is 19 feet at B0 and 89.2 inches at D0).

Before we talk about the world's highest energy accelerator, the Tevatron, let us look into the rest of the accelerator complex, which is a major part of the collider machine: the Antiproton source. This actually produces antiprotons and as well stores them when the collisions are occuring in the Tevatron. As mentioned above, how the 120 GeV proton beam is produced, these 120 GeV protons with a small time spread are extracted from the MR and directed onto a nickel target disk. These collisions produce some antiprotons among other nuclear debris. Antiprotons of 8 GeV are used for simplicity as this is the standard injection energy of Booster protons into the MR. About 10^7 antiprotons are produced for every 10^{12} protons striking the target. Immediately after the target is a cylindrical lithium lens. An azimuthal magnetic field, produced in this lithium piece when a pulsed current of 0.5 MA is passed longitudinally, is used to focus the secondary particles (negatively-charged). Following the lens is a pulsed dipole magnet which selects the 8 GeV negatively charged particles and directs them to the Debuncher. The Debuncher was designed to accept antiprotons fresh from the target and reduce their momentum spread, i.e. short bunches (short in time) coming from the target are rotated in phase space so that the momentum spread becomes small and the time spread large. The pbar cycle is at least 2.4 sec, so there is some free time (2 sec) which is used for the stochastic cooling [28, 29] of the beam to further reduce the momentum spread. This stochastic cooling operates by measuring the trajectory of collections of particles relative to the desired orbit. From this knowledge, a correction signal is derived which is passed across the ring to kicker electrodes which apply a force on the particles to move them back towards the desired orbit. The result of the corrective signal is small due to the incoherent contribution of all other particles near it in the beam ($\approx$ 1 part in 10^6), however this becomes significant when the beam makes $\approx 10^6$ turns per second.

Now the beam of antiprotons, a fairly continuous ribbon with a low momentum spread, is injected into the Accumulator as the Debuncher gets ready for the next batch. The Accumulator is also another storage ring, which lies inside the Debuncher. Further, the stochastic cooling continues for several hours causing the antiprotons to move into smaller and smaller orbits and finally they are pushed into the core, which is 63 mm inside the central orbit whereas they are 80 mm outside the central orbit when injected. When enough antiprotons have accumulated to fill the Tevatron ($\sim$ 50 - 150$\times 10^{10}$), they are extracted from the Accumulator. After being accelerated to 150 GeV in the MR, the antiprotons are injected in bunches into the Tevatron.

The Tevatron is a proton-antiproton colliding beam synchrotron accelerator producing collisions at a center-of-mass energy of 1.8 TeV and is the first large scale user of the superconducting magnets. All the dipoles, quadrupoles and correction magnets are superconducting and are cooled by liquid helium to a temperature of 4.6 K. The Tevatron is quite similar to the MR, with 1000 meter radius, it is situated 25.5 inches below the MR. It currently operates in a "six-on-six" mode where six bunches of protons and six bunches of antiprotons counter–circulate in the ring with two interaction regions, B0 and D0. Each proton bunch is about 150×10^9 protons and the antiproton bunches are composed of roughly 50×10^9 antiprotons each. The beams keep circulating the ring at maximum energy of 900 GeV each and lasts for about 12 to 20 hours. This is called a *store*. Electrostatic separators are used to keep the beam from colliding at unwanted places. The peak luminosity during the run 1B, the previous run during the year 1992-1993 is called 1A, was $2.5 \times 10^{31}/cm^2 sec$.

The future of the Fermilab collider is bright with the new Main Injector coming up. This is getting constructed tangent to the existing Tevatron in a separate tunnel.

This will make possible to achieve higher luminosities of the order of 5×10^{31}. It will also make possible to run the Tevatron in both the collider and the fixed target modes simultaneously. At the time of this writing, construction work was in progress on the Main Injector.

Chapter 3

The DØ Detector

The DØ detector is a multipurpose detector currently operational at the DØ collision point of the Fermilab Tevatron $p\overline{p}$ collider since 1992. It was designed with an emphasis on the study of high p_T physics and high mass states. This includes the search for the top quark, precision study of the W and Z bosons as the test of electroweak theory, perturbative QCD studies as well as searches for new phenomena beyond the "Standard Model". With such physics aims, the DØ detector design stressed the need to identify and measure electrons and muons, the measurement of the direction as well as the total energy of the jets and the determination of missing transverse energy. Less emphasis was paid on identifying and tracking individual particles within jets, as the details of hadronization are not relevant to the underlying hard scattering.

Generally speaking a detector for colliding beam experiment consists of various particle detection devices, based on the first principle of how particles interact with matter. So starting from the point of interaction, we put *tracking* devices which record the hits encountered because of the passing particles in 3-D. At this tracking level itself,

the part closest to the beam-beam interaction, a lot can be accomplished by knowing the momentum of the charged particles by using a magnetic field surrounding the tracking detector. After the tracking device, we need something which could tell us the energy of the particle which is coming out the tracking detector and here comes the need to have a *calorimeter*. Typically a calorimeter would be so thick that it will absorb all the incident particles' energy, basically stopping all known particles coming out except muons and neutrinos. Muons are detected outside calorimeter by using tracking chambers and a magnetic field provides the measure of the momentum of the muons. Neutrinos are not detected directly, chargeless weakly interacting particle, but are accounted for the imbalance left in the total detected momentum transverse to the beam.

3.0.1 Overview of DØ

The DØ detector, illustrated in figure 3.1, as it emerged from papers to negotiations, with different constraints for obvious and non-obvious reasons, in general followed the above discussed ideal topology with the previously briefed physics ambitions and goals. The Tevatron beam pipe can be seen in this picture along with the Main Ring pipe passing through the calorimeter (upper cylindrical part). The tracking detectors are surrounding the beam pipe, followed by the calorimeter. A point worth mentioning here is that DØ does not use any central magnetic field at the moment. One of the reasons for this is because of the energy and momentum resolution dependence between the calorimeter and the tracking detector being complementary to each other. As with the magnetic field, the tracking system's momentum resolution is roughly proportional to the momentum while the energy resolution of a calorimeter is proportional to $1/\sqrt{E}$, meaning for high-p_T objects, a better momentum resolution is obtained from

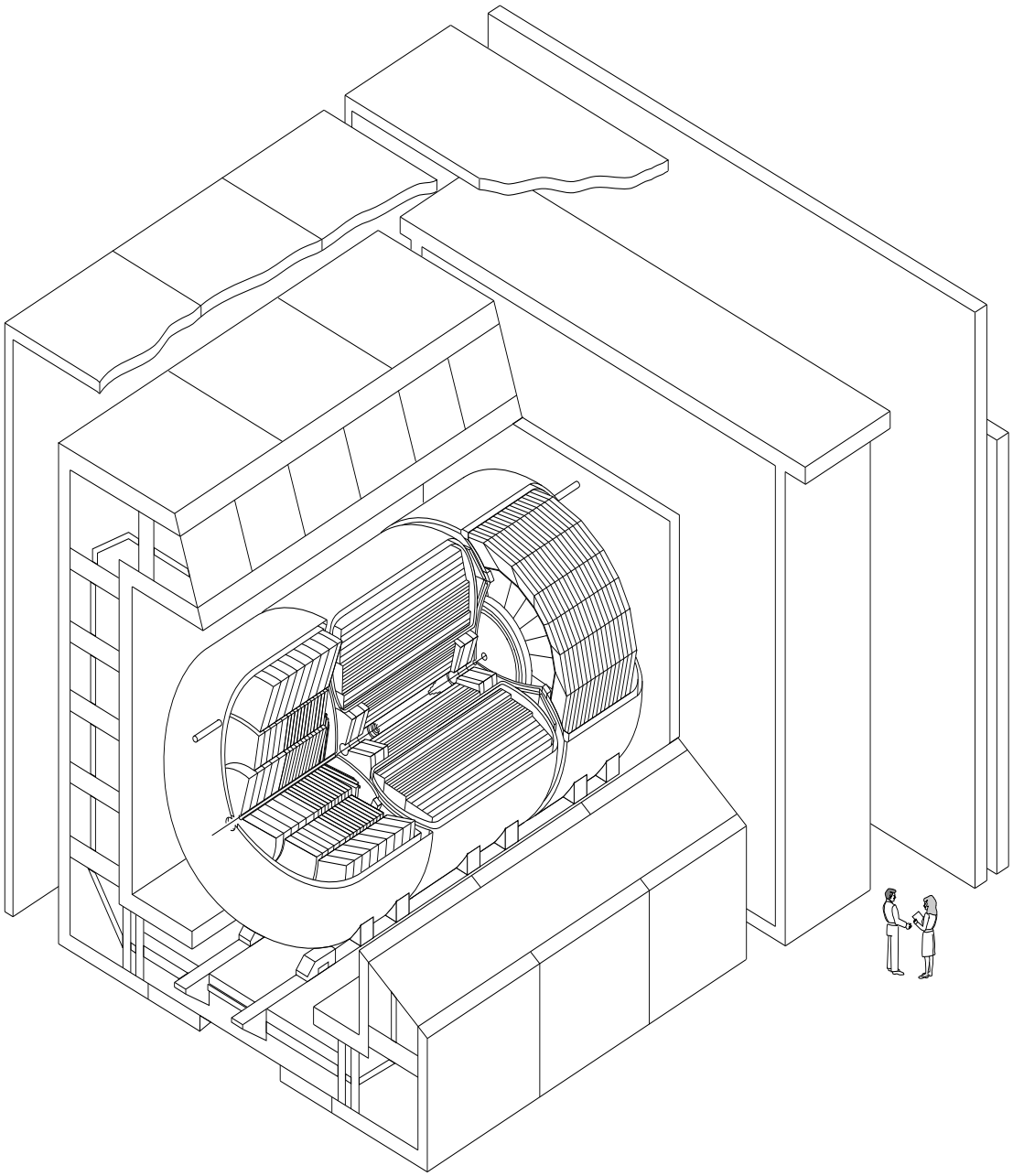

Figure 3.1: Cutaway view of the DØ Detector.

the calorimeter than the tracking system. On the other hand, the very presence of the magnetic field causes low-p_T objects to be removed from the jets, there by changing the energy deposition in the calorimeter. As it looks in figure 3.1, DØ is really a compact detector because of the absence of solenoid. But, size wise it is not a small detector with dimensions of 13m×11m×17m and a total weight of about 5500 tons [30].

The very basic requirement, without magnetic tracking, is thus to have a good calorimeter. The DØ calorimeter which is a uranium-liquid argon sampling (see calorimeter section for details) calorimeter fulfills this need. Muons are tracked down using another set of tracking chambers immersed in magnetized iron toroids installed outside the calorimeter (more later). The whole detector sits on a support platform shown in figure 1.9 (muon section). This platform provides support for the detector electronics modules also. The whole detector talks to the outside world through the counting house, called MCH (moving counting house). This house houses the digitizers, level-1 trigger (see next chapter), voltage supplies and other services.

In the next sections, the major systems and subsystems of the DØ detector are described, but let's first go through the co-ordinate system used in here. The reference line is the proton beam direction, which is the z-axis with the nominal collision point as the "origin". The x-axis points radially outward from the Tevatron ring. Thus, using the right handed Cartesian co-ordinate system, the y-axis is fixed and points towards zenith. In spherical (r, ϕ, θ) co-ordinates, the radial distance r is the distance from the beam axis, ϕ is the *azimuthal* angle about the beam axis, so that $\phi = \pi/2$ is parallel to the upward (+ve) y-axis and the *polar* angle θ subtended with the z-axis, i.e., $\theta = 0$ is coincident with the positive z-axis. However, most of the time we talk about a variable

η, the pseudorapidity, defined as

$$\eta = -\ln(tan\frac{\theta}{2}). \tag{3.1}$$

This variable η approximates the true rapidity y (in the limit that $m \ll E$, where m is the invariant mass $m^2 = E^2 - p^2$), which has the advantage of being simply additive under Lorentz boosts along the z axis.

3.1 Tracking System

As evident from the name itself, a tracking system employed in a particle detector takes care of the paths and trajectories traversed by the charged particles passing through it by reconstructing them in three dimension. This tracking information, either track multiplicity or dE/dx or both, is processed while deciding the source of the electromagnetic showers in the calorimeter (sitting outside the tracking system). The precise measurement of the location of the interaction point for each event helps both the muon momentum measurements and the calorimeter position measurements.

There are different types of tracking detectors being used in the particle detectors namely wire chambers, drift chambers, proportional drift tubes, time projection chambers and silicon detectors. The tracking system for DØ detector consists of four subsystems starting from outside of the Tevatron beam pipe and ending just before the calorimeter detector. These four subdetectors shown in figure 3.2 are: VTX, CDC, FDC (all three drift chambers) and TRD.

The inner most detector is the Vertex chamber (VTX) which lies just outside the

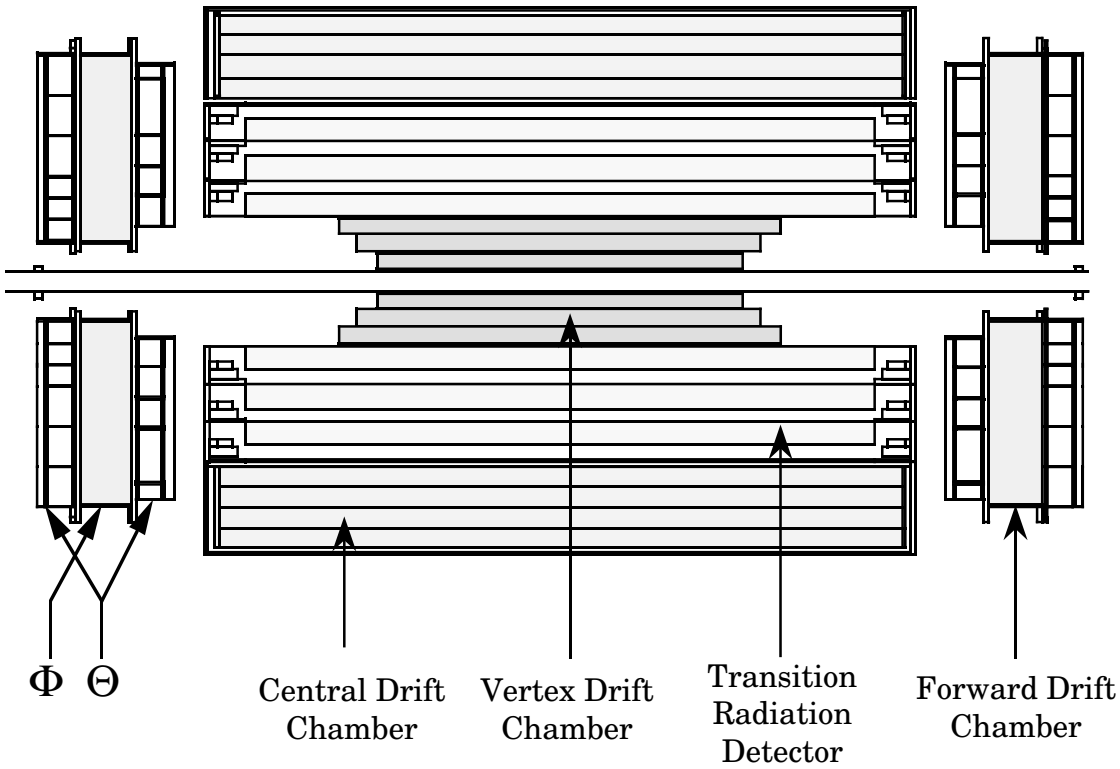

Figure 3.2: Side view of the DØ Tracking System.

beryllium beam pipe. It consists of total three layers. As we move outward, away from the interaction point, the next detector is the Transition Radiation Detector (TRD) for electron identification. TRD has three concentric layers of polypropylene foils followed by radial drift detectors. Surrounding the TRD is the cylindrical central drift chamber (CDC) having four layers of axial wire chambers. At the both ends of this cylindrical CDC lie the forward drift chambers (FDC). These two FDCs consist of two types of chambers, Φ and Θ each. This whole system of four detector is enclosed inside a cylindrical (non-magnetic) volume of radius $r = 75$ cm and length $l = 270$ cm. Before we go into the details of each one of these detectors, let us briefly discuss the working principles of a drift (wire) chamber.

3.1.1 Drift Chamber "Principles of Operation"

A charged particle when passes through a gaseous medium it interacts electromagnetically with the closeby atoms of the medium. This electromagnetic interaction results in both excitation and ionization of the atoms and hence results in the creation of electron and ions. In the presence of an electric field (applied), the ionization electrons and ions start drifting apart towards the anode and the cathode respectively. As the positive ions drift very slowly compared to the electrons, we ignore them here. If the electric field near the anode is strong enough, the incoming electrons can acquire enough energy to create an additional electron by knocking down an atom of the interacting gas. Now this electron can go on and create more free electrons (with positive ions) by collision and thus starts an avalanche with number of electrons increasing exponentially. At an instant this avalanche looks like a drop with all the electrons sitting in the front and the slowly moving ions inside the tail. This avalanche will induce a signal at the anode, giving rise to a measurable current. The size of this avalanche is proportional to the original number of ions created. The detected charge is proportional to the deposited charge through a gain factor called the gas gain which is typically of the order of a few tens of thousands. The physical parameters are tuned to obtain the optimal detection efficiency for the avalanche induced signal.

The avalanche multiplication factor cannot be increased as wanted. This is because of the secondary processes, like photon emission inducing the generation of avalanches spread over the gas volume, and space charge deformation of the electric field (near the front of the avalanche), finally results in a spark breakdown. The way to overcome this is to go for a coaxial geometry. The anode is made up of a very thin wire, stretched

on the axis of the conducting cylinder. The electric field in such a geometry is very strong in the close vicinity of the anode wire and decreases as r^{-1}, towards the outer cylindrical cathode. So, an electron far away from the wire moves slowly with a velocity proportional to the field and as it gets closer to the wire, the rapidly increasing field leads the incoming electron to initiate an avalanche.

Since, the velocity of the drifting electrons is known, determined by the strength of the field and the medium parameters, we can use the known times for the original source particle to start ionization and when the signal arrives at the readout device to find out the drifted distance. Such a device is called a *drift chamber*. This type of measurement is possible only because the time for the signal to traverse the anode wire and the time between the original particle's collision and the beginning of the ionization process is negligibly small compared to the drift time. It is obviously needed to have a linear space-time relationship, and this can be obtained in structures with uniform electric field. However, in a multiwire drift chamber (as used in DØ), the low field region between the anode wires would result in a strong non-linearity of the space-time relationship, especially for large wire spacings. The way out is, the anode wires are alternated with thick field-shaping cathode wires that reinforce the electric field in the critical region.

3.1.2 Vertex Chamber

The Vertex Chamber (VTX) is the first, out of the total four making up the DØ tracking system, and the closest detector to the beam pipe to record the imprints of the particles coming out of the interaction region and passing through it. The VTX

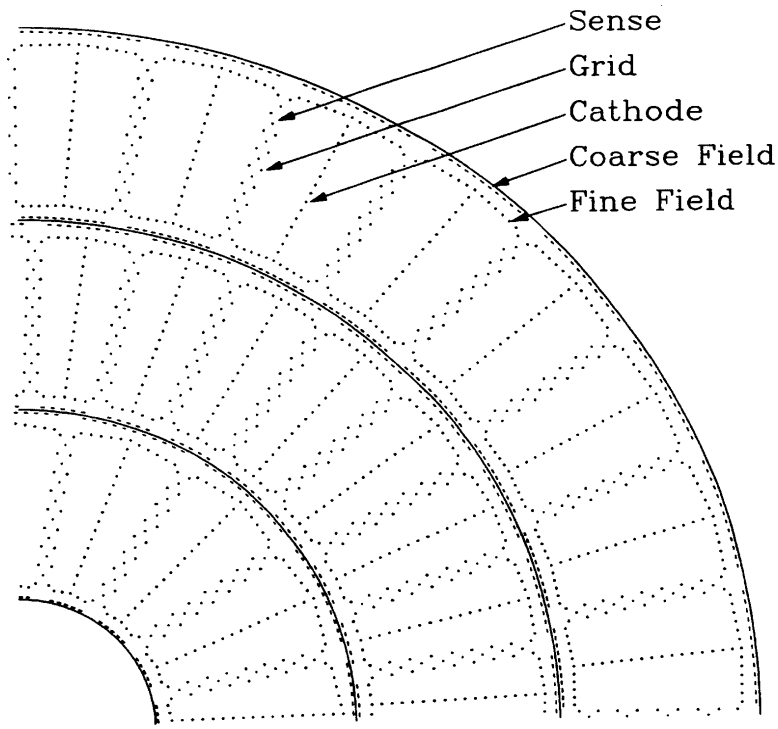

Figure 3.3: End view of one quadrant of the DØ VTX chamber.

can be used to determine the co-ordinates of the interaction vertex of an event. In addition it compliments the other tracking detectors for track reconstruction, dE/dx, and conversion identification (see section on TRD). The VTX consists of three layers of cylindrical drift chambers enclosed in four carbon fiber's concentric layers. The inner most layer has a length of 97 cm and the next two layer are still longer by about 10 cm, with the outer most being about 117 cm in length. The VTX's radial coverage is in the region 3.7 cm $\leq r \leq$ 16.2 cm.

Figure 3.3 shows the $r - \phi$ view of the DØ VTX chamber's one quadrant. The three layers are clearly noticeable. The innermost layer (or layer 0) is made of 16 cells in azimuth and the outer two layers (1 and 2) have 32 cells each in azimuth. These cells are staggered in ϕ between the three layers. This is to avoid the dead regions and to resolve the left-right ambiguities. Such an ambiguity would arise because of the mirror

image of a true track as the drift times do not tell which side of the sense wires' plane the electron drifted from so we have to map the signal corresponding to each SW onto two points. Further, each cell has 8 axially mounted sense wires (SW) or the SWs are in a plane which is parallel to the particle tracks. These SWs are staggered by ± 100 μm with respect to each other. This is done again to resolve the left-right ambiguities which arise when joining together the track segments in different layers of VTX. The field shaping is taken care by fine field, grid, cathode and the sense wires. In addition each cell has a set of aluminium traces on carbon fiber support tubes which works as the coarse field shaper. All of these wires are shown in figure 3.3.

The gas used for the operation of the Vertex drift chamber is a CO_2 - ethane mixture maintained at 1 atm with a small admixture of H_2O. In normal operation the gas is unsaturated, that means the value of field per unit pressure (E/p) is not on the plateau of the curve of drift velocity vs E/p. This is required to obtain the low drift velocity of 7.3 μm/ns which is, in turn, required for a 50 μm resolution (table 3.1). The $r\phi$ position of a hit is determined from the drift time and the wire hit. The z position is determined using a technique which involves reading out the resistive SWs at the two ends and treated as a voltage divider. This technique is known as "charge division". In the high-multiplicity DØ environment, this method of charge division is not as efficient because it requires the SW signals to be well separated and the drift chamber cell occupancy to be low. This necessitates the VTX not to be operated at saturation and keeping the high voltage well under control and uniform to have a uniform space-time relationship (previous section). Some relevant parameters for the vertex chamber are tabulated in table 3.1 [30, 31, 32].

Number of layers	3 (layers 0,1 and 2 of equal thickness)
Length of each layer	96.6 cm (for 0), 106.6 cm (1), 116.8 cm (2)
Radial interval	3.7 cm to 16.2 cm
Number of cells/layer	16, 32, 32
Number of sense wires (SW)	8 per cell (total 640)
SW separation	radial = 4.6 mm; stagger = 100 μm
SW specification	25 μm NiCoTin, 80 g tension
SW voltage	+2.5 kV
Field wire specification	152 μm Au-plated Al, 360 g tension
Gas used	CO_2 95%, ethane 5%, H_2O 0.5% at 1 atm and 25° C
Gas gain	4×10^4
Average drift field and velocity	1 kV/cm, $\approx$ 7.3 μm/ns
Maximum drift distance	1.6 cm
Position resolution	$r\phi \approx 60$ μm, $z \approx 1.5$ cm

Table 3.1: The DØ VTX chamber parameters.

3.1.3 Transition Radiation Detector

The second subsystem in line after VTX is the transition radiation detector or TRD. The basic principle of its working is that when a charged particle crosses the boundary between two materials with different dielectric constants, photons are emitted in the forward direction. This phenomenon is known as transition radiation. The intensity of this radiation is proportional to the relativistic gamma factor ($\gamma = E/(mc^2)$) and is emitted in a cone with a half opening angle of $1/\gamma$ with respect to the particle direction. The intensity of radiation emitted from a single particle when crossing one and only one boundary is not enough to be detected readily, so a large number of such boundaries are stacked together to give a detectable signal. For highly relativistic particles ($\gamma > 10^3$), the emitted radiation is in the X-ray region. So we can, basically, use this property to

distinguish between two energetic particles having different masses (but similar energies). For instance, at Tevatron energies, the most energetic particles are electrons which can produce detectable transition radiation but a $\pi^0 \rightarrow \gamma\gamma$ can fake an electron with an overlapping low-energy track associated with this electromagnetic jet. This situation is different in a magnetic tracking system, which is not the case with DØ so the transition radiation intensity measurement gives us a tool to overcome such a background.

The TRD covers the region of $|\eta| < 1.2$ and occupies the annular region between the VTX and the CDC (next section). It consists of three separate, cylindrical, layers each having a radiator and a detector of its own. The radiator is made of 393 layers of 18 μm thick polypropylene foils separated by nitrogen gas with a mean spacing of 150 μm. The energy spectrum of transition radiation is peaked at 8 KeV and is contained well below 30 KeV. Surrounding each radiator is a cylindrical X-ray detector. This detector is composed of two stage time-expansion type proportional wire chamber (PWC). The first stage is a 15 μm space filled with the operating gas (Xe/C_2H_6) for the conversion of X-rays. In the second stage, where avalanche takes place, anode or sense wires and field shaping wires are present. For further information on the performance of TRD refer to [30, 33, 34].

3.1.4 Central Drift Chamber

The central drift chamber is the outermost tracking subsystem, just before the central calorimeter. This tracker covers a pseudorapidity range of $|\eta| \leq 1.2$. The cylindrical CDC consists of four concentric cylindrical layers, which occupy the active radial region between 51.8 cm - 71.9 cm. Figure 3.4 shows the end view of a portion of the CDC.

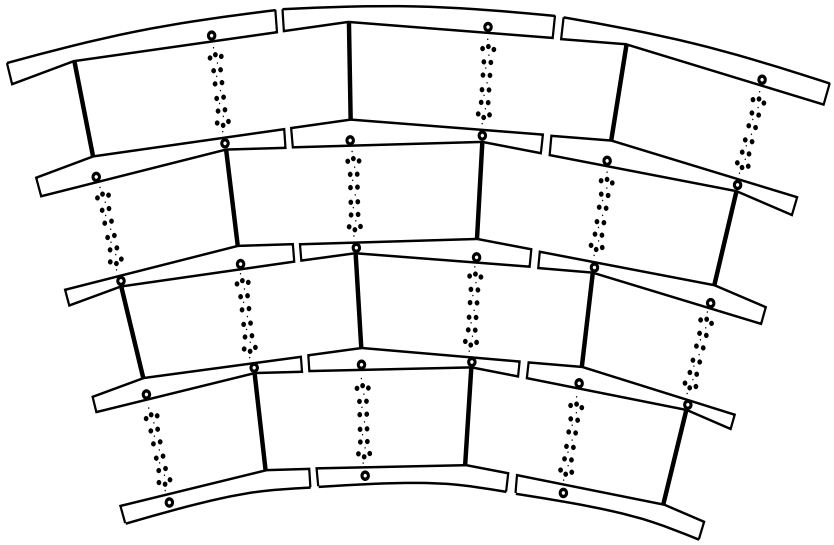

Figure 3.4: End view of three CDC modules.

The CDC, with a length of 184 cm, occupy the region of 49.5 cm $\leq r \leq$ 74.5 cm. The CDC is made up of 32 separate but identical modules placed inside a cylindrical shell. Three such modules are shown in the above figure. The module walls are made from Rohacell foam laminated with Kevlar and wrapped with Kapton layer, 50 μm thick. The ends of these modules are capped with G10 walls and the chamber ends are capped by aluminum plates. This whole setup is enclosed in an aluminum tube having a carbon fiber tube sealing the inner radius. All the 32 cells consist of 7 sense wires and 2 delay lines. The sense wires are staggered by $\pm$200 μm to resolve the left-right ambiguities and the cells, in different layers, themselves are staggered by half a cell to further enhance the pattern recognition. The delay lines are readout at both ends for determining the z co-ordinate, i.e. when an avalanche occurs near a sense wire, a pulse is induced in the nearby delay line, embedded in the module walls in the sense wire plane, and by comparing the arrival times of the signal at both ends the z position is measured. The $r\phi$ position of a hit is determined via the drift time and the wire hit.

Number of layers	4
Active radius	51.8 cm - 71.9 cm
Number of cells	32 per layer
Number of sense wires (SW)	7 per cell (896 total)
SW separation	radial = 6 mm; stagger = 200 μm
SW specification	30 μm Au-plated W; 110 g tension
SW voltage	inner SW = +1.45 kV, outer SW = +1.58 kV
Number of delay lines (DL)	2 per cell (total 256)
Field wire specification	125 μm Au-plated CuBe, 670 g tension
Gas composition	Ar 93%, CH_4 4%, CO_2 3%, H_2O 0.5%
Gas pressure	1 atm
Average drift field	620 V/cm
Drift velocity	$\approx$ 34 μm/ns
Maximum drift distance	7 cm
Gas gain	inner SW = 2×10^4, outer SW = 6×10^4
Resolution	$r\phi \approx 180$ μm, $z \approx 2.9$ mm

Table 3.2: Central Drift Chamber Parameters.

Field shaping is provided by a set of resistive strips printed on the Kapton cell surface. More CDC parameters are listed in the table 3.2, for further description of the DØ CDC see [30] [35, p. 37-43].

3.1.5 Forward Drift Chambers

The forward drift chambers [36, 37, 38] take over the central drift chamber's job in the "forward" region, i.e for $|\eta| > 1$ and down to an angle of $\theta \approx 5^o$. See figure 3.2 for the location of FDC as a part of the DØ tracking system. There are two sets of chambers, one located at each end of the CDC. This each set of FDC consists of one Φ

module sandwiched between two Θ modules. Figure 3.5 illustrates the details of one such FDC set. It shows that the two Θ layers are rotated by 45° with respect to each other.

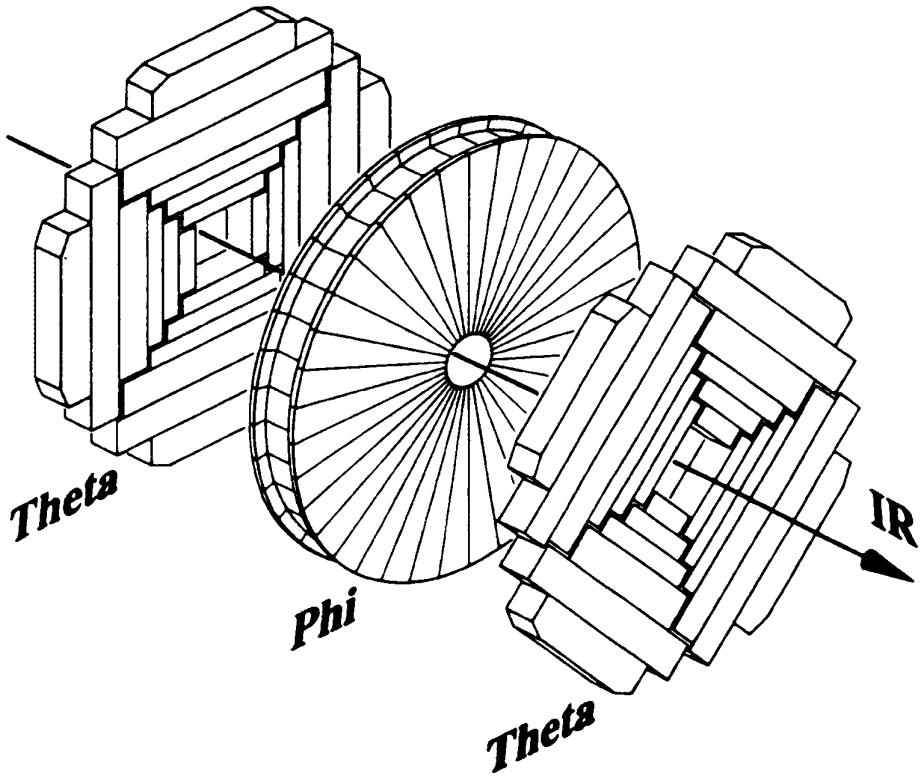

Figure 3.5: One of the two sets of the FDCs.

Further, the four quadrants of the Θ layers, each of which is made of 6 rectangular drift cells, are noticed. Each of these cells have 8 sense wires arranged in a plane parallel to the z-axis and perpendicular to the radial direction. The inner three cells are half cells in which the sense wires are strung at one edge of the cell. The electron drift is, therefore, unidirectional and left-right ambiguities do not exist. These Θ cells also contain a delay line each to measure the position along the length of the cell. Each Φ module is a single chamber containing 36 azimuthal cells (i.e. over the full ϕ range). Each cell has 16 sense wires strung radially (forming a plane in rz), but there are no delay lines. Construction wise FDCs are similar to the CDC, except that the FDCs use 25 μm aluminum etchings

instead of the CDC's epoxy strips. Vital statistics regarding the FDC's can be found in table 3.3.

Parameter	Θ modules	Φ modules
Active radial coverage	11 cm - 62 cm	11 cm - 61.3 cm
Active z interval	104.8 - 111.2 cm 128.8 - 135.2 cm	113.0 - 127.0 cm
Number of cells per layer	6 per quadrant	36
Number of sense wires(SW)	8 per cell	16 per cell
SW separation	8.0 mm radially with ± 200 μm stagger	
SW specification	30 μm Au-plated W, 50 - 100 g tension	
SW voltage	+1.55 kV	+1.66 kV
Number of delay lines	1 per cell	none
Delay line velocity	2.35 mm/ns	—
Field wire specification	163 μm Au-plated Al, 100 - 150 g tension	
Gas composition	Ar 93%, CH_4 4%, CO_2 3%, H_2O 0.5%	
Gas pressure	1 atm	1 atm
Average drift field	1.0 kV/cm	1.0 kV/cm
Drift velocity	40 μm/ns	37 μm/ns
Drift distance (Max.)	5.3 cm	5.3 cm
Gas gain	inner SW = 2.3×10^4 outer SW = 5.3×10^4	3.6×10^4
Resolution (drift)	$\approx$ 300 μm	$\approx$ 200 μm

Table 3.3: Forward Drift Chamber Parameters.

3.1.6 Tracking Electronics and Readout

All the detectors in the DØ tracking system have identical electronics, composed of three main stages: pre-amplification, pulse shaping and analog to digital conversion. All the tracking chambers together have more than 8000 channels which must be processed in parallel. In the first stage of signal processing, the signals from the chamber wires are fed into preamps attached to the chambers themselves. From there, the signals are carried to the detector platform, where the analog pulse shaping cards are located (underneath the detector). Then this analog shaped output is sent to flash analog-to-digital converters (FADCs) located in the moving counting house. The signals are sampled and digitized here at a rate of 106 MHz, starting at the beam crossing. More information on tracking electronic can be found in [30, 36].

3.2 Calorimeter

In the absence of the central magnetic field, the calorimeter is the heart of the DØ detector and the source of precise energy measurements for electrons, photons and jets. The very presence of the DØ calorimeter enhances the capabilities to identify (see chapter 5) electrons, photons, jets and muons, which at first appears to be a hard task in the absence of the magnetic field. Calorimeter comes in handy when calculating the total missing transverse energy (because of neutrinos) in the DØ detector. Before we go into the details of the DØ calorimeter the working of such a wonderful device is briefly discussed below.

3.2.1 Principles of Operation

A calorimeter is a block of matter of sufficient thickness which intercepts the primary particle and causes it to interact and deposit all of its energy in the subsequent cascade or shower of increasingly lower-energy particles [39]. For an electromagnetic object, the mechanisms by which it can lose energy, when it passes through a dense material, are Bremsstrahlung and pair production depending upon whether the incoming primary is an electron or photon respectively. The particles produced as a result of these interactions can themselves undergo the processes responsible for their creation. Thus an energetic electron or photon showers into secondary electron, positron and photons. The resultant shower is called an *electromagnetic shower*. The unit of measure for an electromagnetic shower is the *radiation length* X_o, which is related to the rate at which an incident particle loses energy, and is a constant of material. For hadronic particles the particle showers primarily by knocking protons and neutrons out of the nuclei of the atoms. This is because of the inelastic collisions between the incoming hadron and the atomic nuclei. As a result we have secondary hadrons, which in turn can undergo again such inelastic collisions. Now the process is called a *hadronic shower* and the measure of such a shower is given in terms of nuclear *interaction length* λ for the material. For example, uranium has $\lambda \approx 10.5$ cm and X_o about 3.2 mm. This implies that the hadronic showers are bigger in size as compared to the electromagnetic showers of similar energy.

The next step is to measure the energy of the shower particles. This can be achieved in two ways: either make the absorber to function as an active material also or to have alternate layers of both an absorber and an active medium through which the particles pass. The first type of calorimeter is called a *homogeneous* calorimeter with best energy

resolution. Some typical materials for such a calorimeter are NaI, BGO ($B_4Ge_3O_{12}$) and lead glass. These type of detectors are not practical in high-energy scenario. So the alternative, sandwich, type of calorimeters having a dense, inert absorber with interlaced layers of an active material is used. Such a calorimeter is called a *sampling* calorimeter. As the shower particles lose most of their energies in the absorber part of the detector, only a fraction of the incident energy can be detected. This fraction is called the *sampling fraction.* Being statistical in nature this sampling process reduces the energy resolution of the calorimeter. The response of a calorimeter (which is the ratio of the measured signal to the energy of an incident particle) may not be the same for the electromagnetic and the hadronic showers. As a hadronic shower will contribute to the electromagnetic component also because of the γ's from π^o and η decays, the response for a hadronic shower tends to be lower [40]. So the response for a calorimeter is expressed in terms of the e/π ratio, the ratio of the calorimeter responses to electrons and pions. A calorimeter with this ratio close to 1 is called a *compensating* calorimeter.

The DØ calorimeter is a sampling calorimeter with Uranium/Copper/stainless steel as the absorber and liquid Argon as the ionization medium. The choice of liquid Argon as the active medium comes with the advantages of unit gain, radiation hardness, low cost of readout electronics and a straightforward method of calibration. However, the use of liquid argon is also disadvantageous in terms that it requires the cryostats to maintain the liquid argon at 86 K and it further prohibits the access to the calorimeter modules during operation. Uranium was chosen as the absorber for the electromagnetic (EM) and fine hadronic (FH) layers. Uranium being very dense allows the calorimeter to be of very compact size.

A typical calorimeter unit cell is shown in figure 3.6. Such a cell consists of an

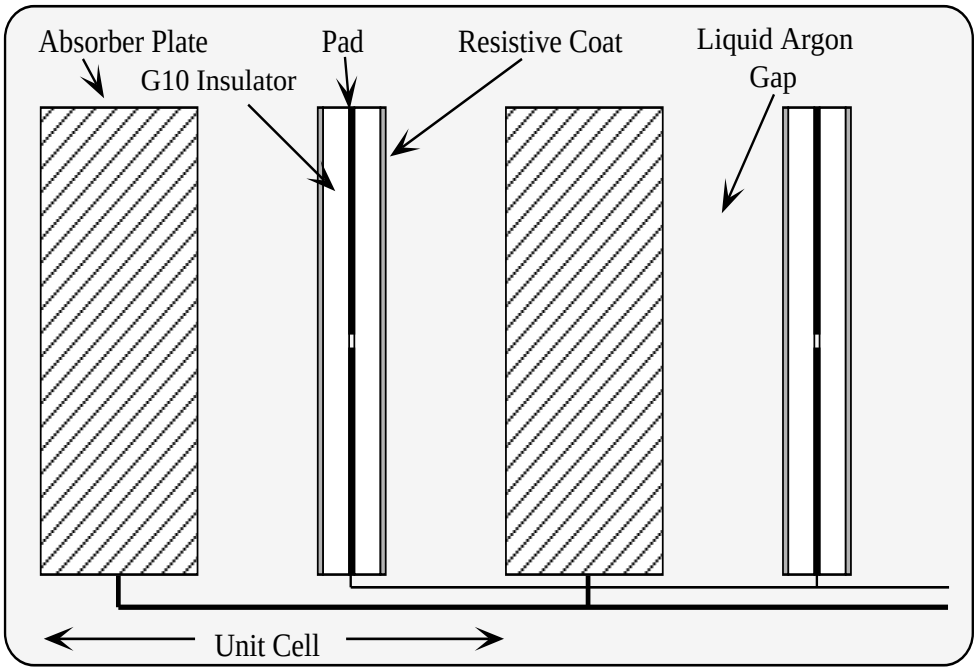

Figure 3.6: Schematic view of a DØ calorimeter cell.

absorber plate and a signal board with the gap between them filled with liquid argon. The absorber plate is grounded and a positive voltage of 2.0 - 2.5 kV is applied to the signal board. This creates the field necessary to drift the electrons from the ionization medium to the signal board. The signal board construction is of two different types depending upon the location of the board (when the gap between neighboring azimuthal sectors is critical the signal boards are made of multilayer PCBs). The outer surfaces are coated with a high resistivity carbon loaded epoxy and the required segmentation is provided by etched pads on an interior surface. The other type of signal boards consist of copper pads sandwiched between two 0.5 mm G-10 sheets having the same resistive coating on the outer side. The signal board in figure 3.6 is of second type. Readout cells are formed by ganging together several signal boards with approximately the same $\Delta\eta$ and $\Delta\phi$ in depth [30].

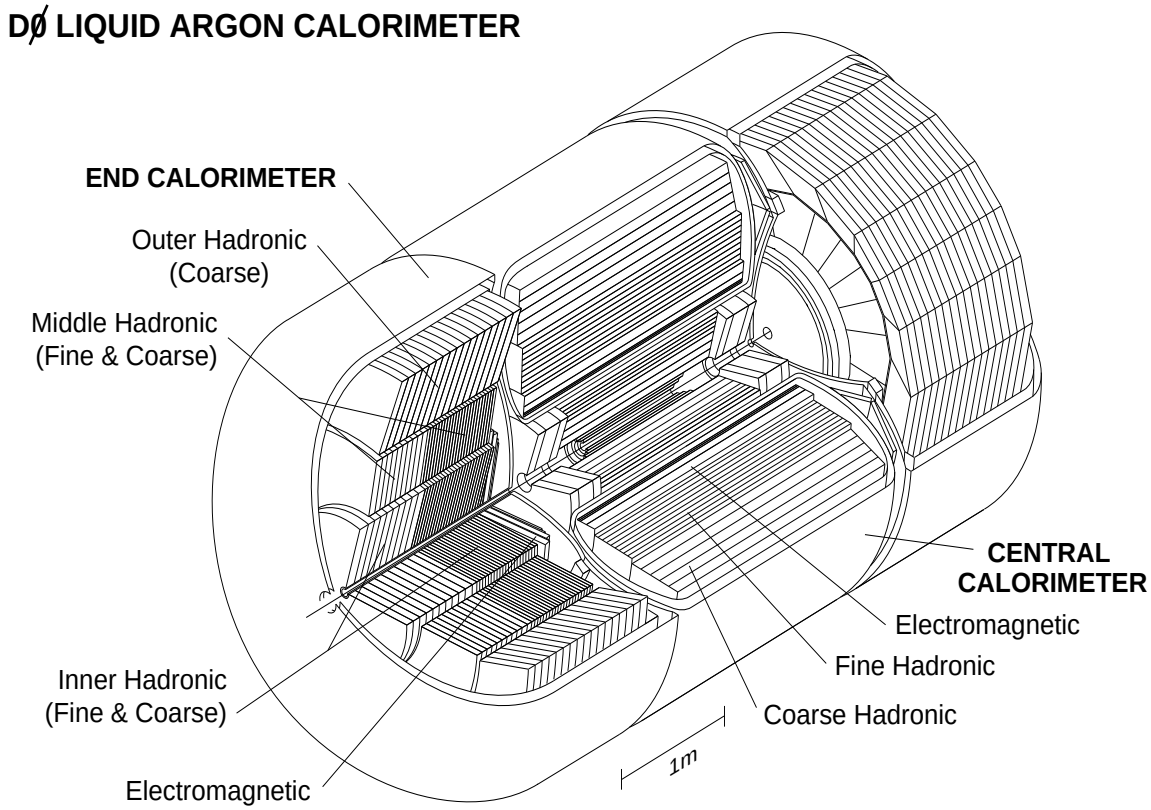

Figure 3.7: Isometric view of the DØ Calorimeter.

3.2.2 Central Calorimeter

The DØ calorimeter, figure 3.7, is constructed in three parts, each in its own cryostat to provide access to the central detectors: central calorimeter (CC) and the 2 endcap calorimeters (EC). The central calorimeter covers the region upto a pseudorapidity of about 1.2. The CC consists of three concentric cylindrical layers. The innermost layer is made up of 32 azimuthal electromagnetic (EM) modules. The signal boards' readout cables are ganged into four longitudinal layers. These layers are named as EM1 through EM4, with EM1 being the innermost and EM4 the outermost. The thickness of these EM modules is enough to contain most electromagnetic showers. These four layers have X_o = 2.0, 2.0, 6.8 and 9.8 respectively starting from the EM1. The transverse

Module $\longrightarrow$	EM	FH	CH
Rapidity coverage	± 1.2	± 1.0	± 0.6
Number of modules	32	16	16
Absorber[1]	Uranium	Uranium	Copper
Absorber thickness (mm)	3	6	46.5
Argon gap (mm)	2.3	2.3	2.3
Number of signal boards	21	50	9
Number of readout layers	4	3	1
Cells per readout layer	2,2,7,10	20,16,14	9
Total radiation lengths[2] (X_o)	20.5	96.0	32.9
Total nuclear absorption lengths[2] (λ)	0.76	3.2	3.2
Sampling fraction (%)	11.79	6.79	1.45
Total readout cells	10,368	3000	1224

Table 3.4: Central Calorimeter Parameters.

segmentation is $\Delta\eta = 0.1$ and $\Delta\phi = 0.1$, except in EM3 where it is 0.05 both in $\Delta\eta$ and $\Delta\phi$. Outside this EM layer is the fine hadronic (FH) layer having 16 azimuthal modules. This FH section has only three longitudinal readout layers with transverse segmentation 0.1×0.1. The outermost layer is called coarse hadronic (CH). This layer also has 16 modules, which measure any leakage of energy out of FH. This layer, in addition, serves as a shield to stop large longitudinal fluctuations from entering into the muon system. Table 3.4 gives a summary of some important CC parameters [41, p. 55] [35, p. 55].

[1] Uranium is depleted and FH absorbers contain 1.7% Niobium alloy.

[2] At $\eta = 0$.

3.2.3 Endcap Calorimeter

The two endcap calorimeters extend the pseudorapidity coverage to 4.5 on each side of the CC. Endcaps are similar in construction to the CC in terms of gap structure, readout structure and segmentation. EC, like CC, also contains the EM and the hadronic sections. The hadronic sections are further subdivided into 3 parts: inner, middle and outer hadronic. So, in total EC has four types of modules as shown in figure 3.7. The absorber plates are the same in EM and FH portions but the CH portions use stainless steel plates instead of copper. Transverse segmentation is also the same (0.1×0.1) except for $3.2< |\eta| <4.5$ where it increases from 0.2×0.2 to 0.4×0.4. The ECEM also has four readout layers (EM1 through EM4). Followed by ECEM are two inner hadronic (ECIH) modules. The fine hadronic part has 4 readout sections, each containing 16 absorber plates while the coarse hadronic portions has a single readout section containing 13 absorber plates. The middle hadronic (ECMH) and outer hadronic (ECOH) are concentric layers outside the ECEM and ECIH modules. The ECMH has four FH and one CH sections, whereas the ECOH has only one CH section. More important parameters for the EC are listed in table 3.5 [41, p. 56] [35, p. 57].

3.2.4 ICD and MG Detectors

Looking at figure 3.8, one notices in the transition region between the CC and EC, corresponding to $0.8 < |\eta| < 1.4$ that there is a significant amount of uninstrumented (or dead) material. This is due to the cryostat walls, module endplates and the support structures for them. The ICD (Intercryostat Detector) and the MG (Massless gaps) help to sample the energy deposited (or lost otherwise) in this region. The ICD consists of

Module $\longrightarrow$	EM	IFH	ICH	MFH	MCH	OH
Rapidity range	1.3-3.7	1.6-4.5	2.0-4.5	1.0-1.7	1.3-1.9	0.7-1.4
Number of modules	1	1	1	16	16	16
Absorber[3]	DU	DU-Nb	SS	DU-Nb	SS	SS
Thickness (mm)	4	6	6	6	46.5	46.5
LAr gap (mm)	2.3	2.1	2.1	2.2	2.2	2.2
Signal boards	18	64	12	60	14	24
Readout layers	4	4	1	4	1	3
Cells/readout layer	2,2,6,8	16	14	15	12	8
Total rad. length	20.5	121.8	32.8	115.5	37.9	65.1
Total abs. length	0.95	4.9	3.6	4.0	4.1	7.0
Sampling frac.(%)	11.9	5.7	1.5	6.7	1.6	1.6
Total readout ch.[4]	7488	4288	928	1472	384+64	896+64

Table 3.5: Endcap Calorimeter Parameters.

384 scintillator tiles mounted on the inner surface of the EC. The tiles have a size of 0.1×0.1 segmentation in $\Delta\eta \times \Delta\phi$ and exactly match the calorimeter cells in CC and EC. The massless gaps are mounted on the CCFH, ECMH and ECOH modules. These MG consist of simply two signal boards surrounded by liquid argon. The segmentation is again 0.1 in both the η and ϕ space.

3.2.5 Calorimeter Electronics and Readout

The processing of the signal from the calorimeter starts with pre-amplification electronics located in four enclosures on the surface of each cryostat. The signal is then

[3]Depleted uranium (DU), depleted uranium with 1.7% niobium (DU-Nb), or stainless steel (SS).

[4]MCH and OH cells are summed together at $|\eta| = 1.4$

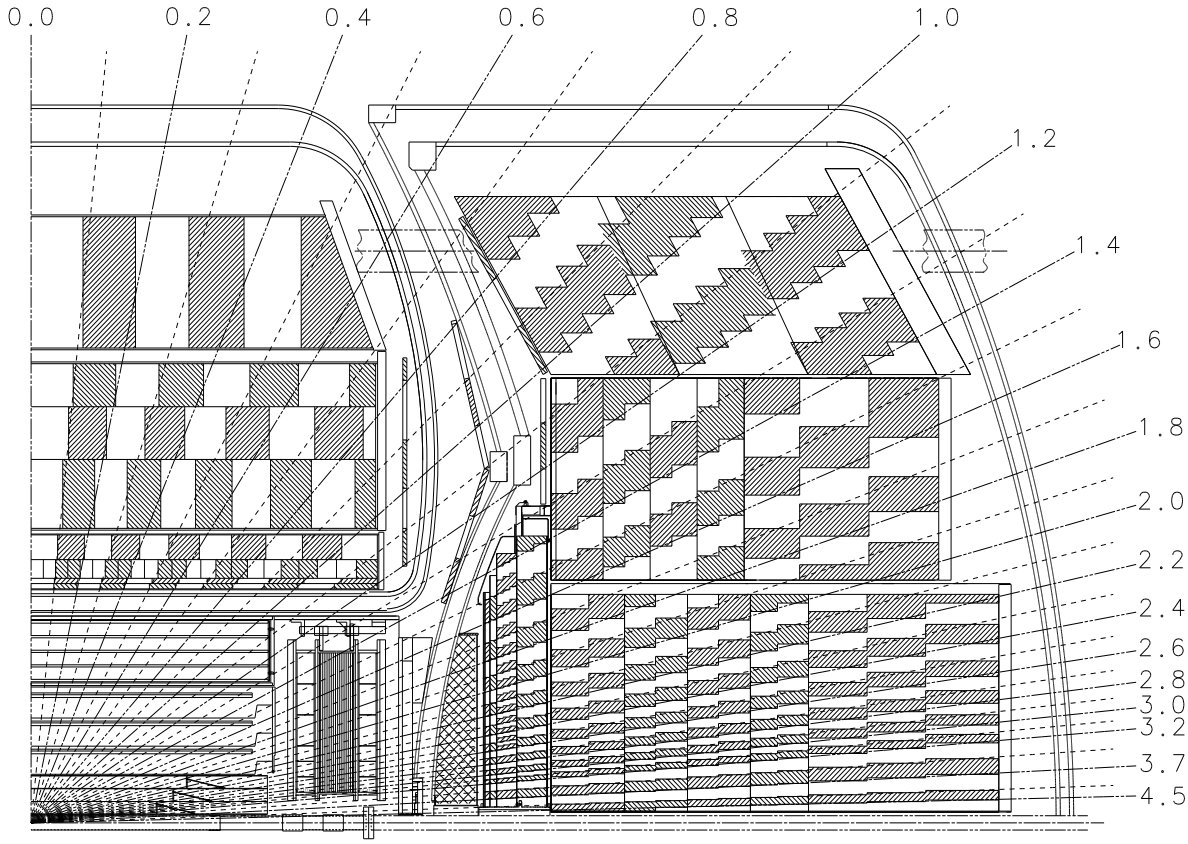

Figure 3.8: Side view of the calorimeter segmentation.

brought to the baseline subtracter (BLS) shaping and sampling hybrid circuits located in the detector platform. The BLS modules split the signal into two paths.

The first path is used for triggering. The signals from all the fine hadronic cells within a 0.2×0.2 tower are summed and similarly the signals from the electromagnetic cells. These signals then form the input to the level-1 calorimeter trigger (chapter 4).

The second path is used for data readout. The incoming signal is sampled just before the beam crossing and again 2.2 μs later. The difference of the two is provided as a DC voltage proportional to the collected charge. This difference is amplified by a

factor of 1 to 8 depending on the signal size, multiplexed by a factor of 16, and then sent to the 24-channel 12-bit ADC circuits in the MCH.

3.2.6 Calorimeter Response and Resolution

As discussed in section 3.2.1, a perfectly compensating calorimeter (with e/π close to 1) will also have some sort of degraded resolution because of energy fluctuations and because of the statistical nature of the shower and sampling processes. Several other sources of energy fluctuations are listed below [35, p. 51]:

- leakage of energy out of the calorimeter
- noise in the active layers due to natural radioactivity of the uranium plates
- variations in high voltage, absorber thickness and spacing, electronics gain, liquid argon temperature and its purity
- electronic noise

The response of the calorimeter modules to single electrons and pions has been studied in test beams [30] [41, p. 60]. The response is found to be linear, for both of these, to be within 0.5%. For DØ the resolution is parameterized as

$$\left(\frac{\sigma}{E}\right)^2 = C^2 + \frac{S^2}{E} + \frac{N^2}{E^2} \tag{3.2}$$

where the constants C, S, and N represent the calibration (gain) errors, sampling fluctuations, and noise contributions (includes electronic and uranium noise) respectively.

The measured constants for electrons are

$$C = 0.003 \pm 0.002,\ S = 0.157 \pm 0.005\,(GeV)^{\frac{1}{2}},\ N \approx 0.140\,GeV \tag{3.3}$$

and for pions,

$$C = 0.032 \pm 0.004,\ S = 0.41 \pm 0.04\,(GeV)^{\frac{1}{2}},\ N \approx 1.28\,GeV. \tag{3.4}$$

The position resolution for electrons is found to be about $0.8 - 1.2$ mm, varying approximately as $1/\sqrt{E}$. The position resolution is very important (in conjunction with the tracking) to distinguish electrons from $\pi^{\pm}/\pi^{o}$ overlaps. The e/π ratio of the calorimeter falls from about 1.11 at 10 GeV to about 1.04 at 150 GeV.

3.3 Muon System

Finally we get to talk about the DØ Muon system, the outermost particle detection system of the four storey high assembly of various detectors. Muon, earlier thought to be the Yukawa mediator (section 1.1), does not interact strongly and being $\approx$ 200 times heavier than electron does not readily produces electromagnetic showers either. Muons having a lifetime of 2.2 μs traverse the whole detector without interacting thus may be regarded as stable in the relativistic regime. So, along with neutrinos, muons are the only particles surviving the dense calorimeter material and as they carry charge are detected by the tracks left by them where as neutrinos leave completely undetected. While passing through the calorimeter muons do deposit energy corresponding to a minimum ionizing particle, a good enough trace to confirm the muon's passage.

The DØ muon detection system [30] consists of five separate solid-iron toroidal

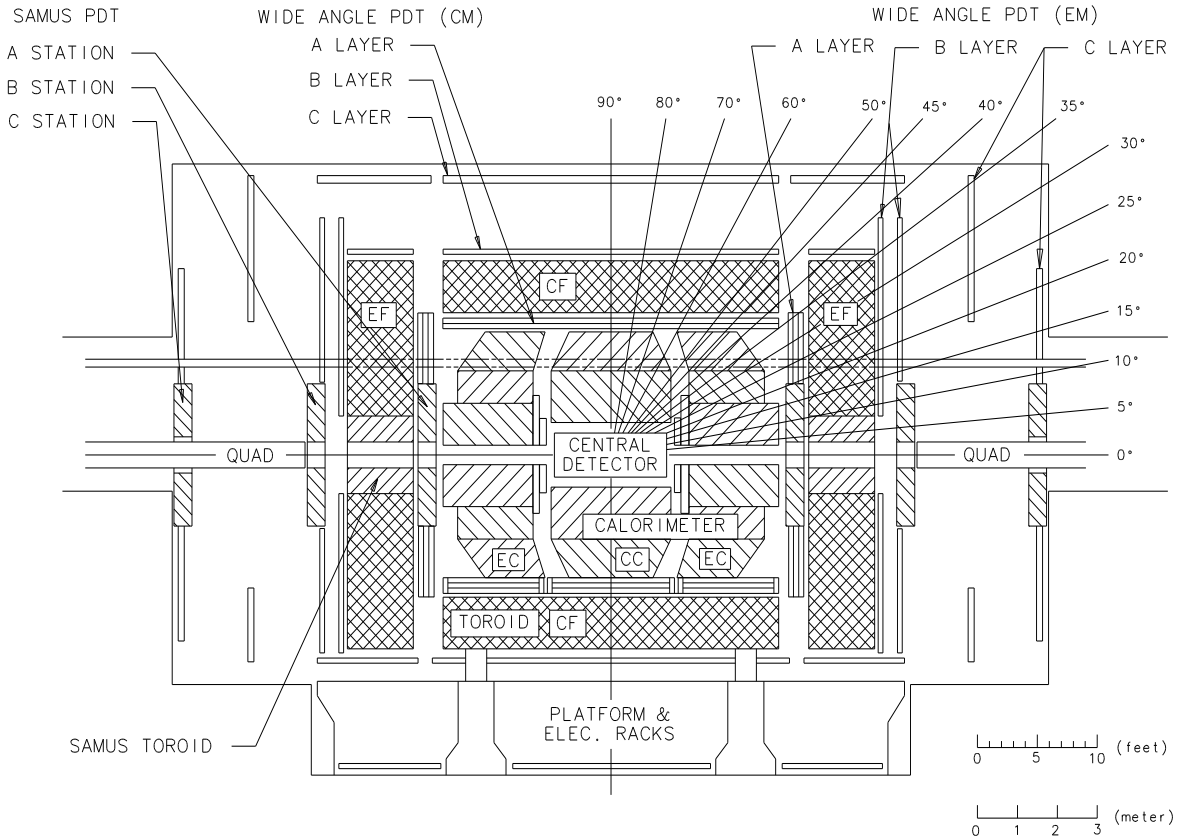

Figure 3.9: Elevation view of the DØ detector showing the muon system.

magnets, with three layers of proportional drift tube chambers (PDTs) surrounding these toroids for measuring the track co-ordinates (see figure 3.9). The purpose of this system is the determination of the muon trajectories and the momenta, which is done by measuring the muon's trajectory before and after it passes through the magnetized iron toroid. The five iron toroidal magnets are: the CF (covering $|\eta| \leq 1$), two EFs (cover $1 < |\eta| \leq 2.5$) and the two Small-Angle MUon System (SAMUS) magnets. These SAMUS toroids fit in the central hole of the EF toroids (see figure 3.9) and cover $2.5 < |\eta| \leq 3.6$. The CF and the two EFs together are referred to as the Wide-Angle MUon System (or WAMUS). Both the WAMUS and SAMUS chambers are deployed in three layers: the "A" layer before the iron toroids and the "B" and "C" layers after the

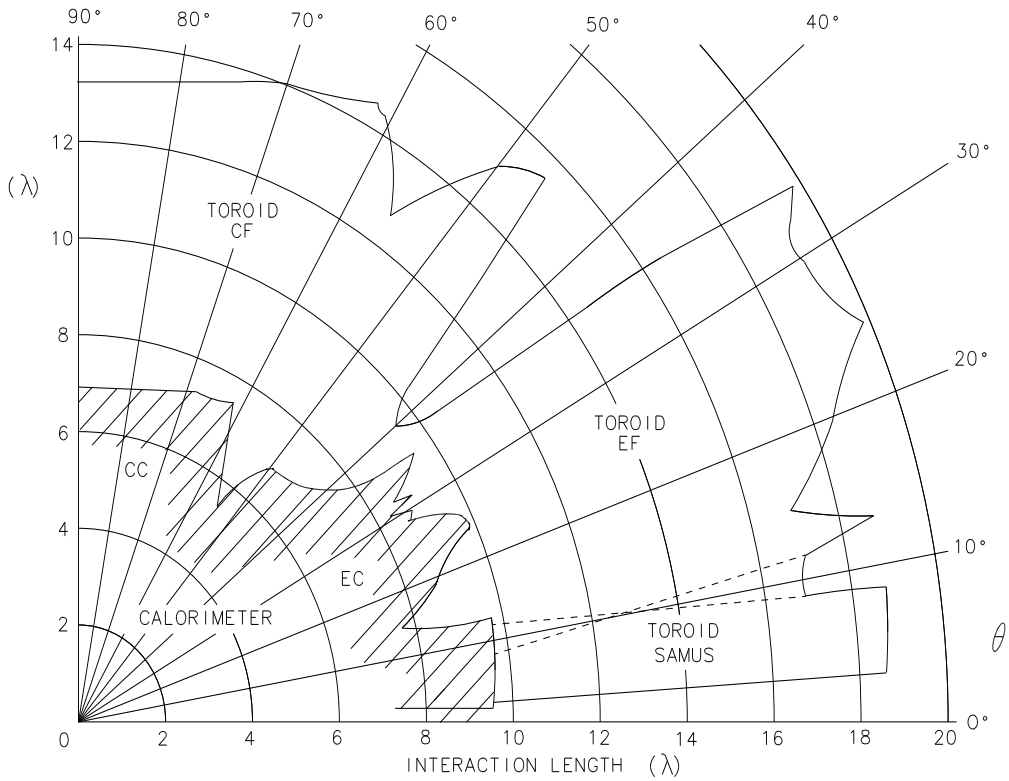

Figure 3.10: Detector thickness (in interaction lengths) as a function of polar angle.

magnets. The air gap between the B and C layers varies from 1 to 3 m. As noticed in the figure 3.9, there are some gaps (missing PDT layers) underneath the detector to provide support elements for the calorimeter and give access to the detector.

The muon system is quite thick, as shown in figure 3.10 the variation of the detector thickness, in terms of nuclear interaction lengths, as a function of polar angle clearly indicates the amount of material present before a muon enters the muon toroids. This helps in reducing the hadronic punchthrough [42] background and provides us with a clean muon identification environment. This allows muons to be identified in the middle of hadron jets with much greater purity than electron can be. The minimum momentum

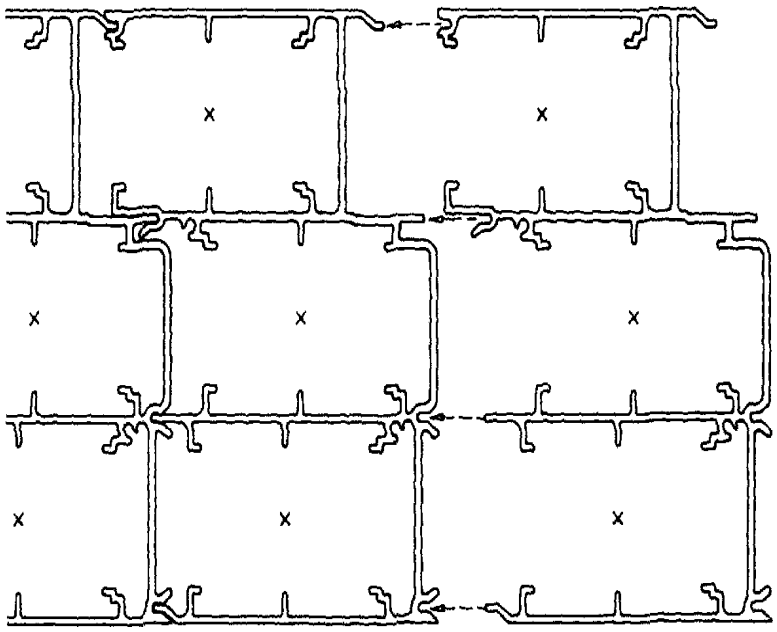

Figure 3.11: Aluminium extrusion cells forming the muon PDTs.

required for a muon to emerge from the iron toroids varies from about 3.5 GeV/c at $\eta = 0$ to about 5 GeV/c at larger η [30].

3.3.1 WAMUS and SAMUS Systems

The WAMUS PDTs are formed from aluminium extrusion unit cells as shown in figure 3.11. These rectangular drift cells have only one anode wire each (50 μm gold-plated tungsten). Both the B and C layers have three such extrusions from which the PDT chambers are constructed, whereas the A layer chambers have four such cells. Also visible, in figure 3.11, is the relative offset between the planes of chambers that allows breaking of the left-right drift-time ambiguity. The WAMUS chamber wires are parallel to the direction of the magnetic field to give an accurate measurement of the bend co-ordinate (perpendicular to the wires) by measuring the drift time.

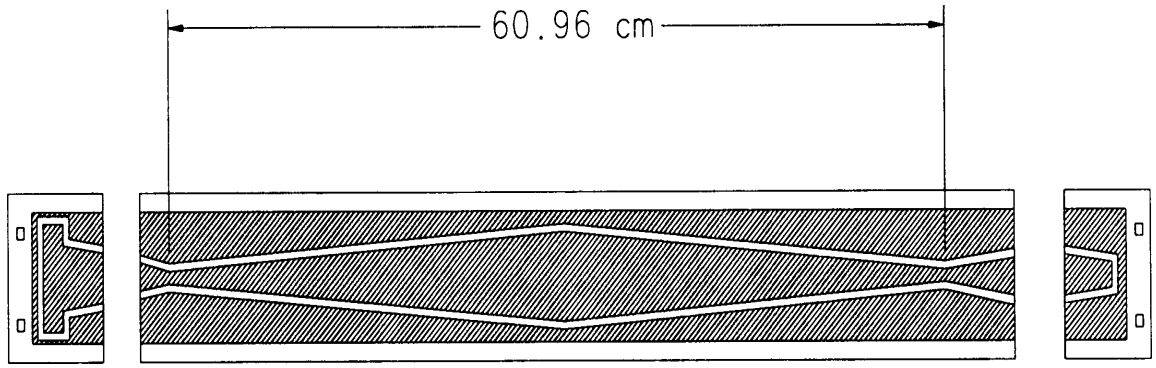

Figure 3.12: Two separate electrodes comprising the PDT cathodes.

The position measurement along the wire direction is done by using the timing information from the anode wires and the cathode pad signals. For this, wires from two adjacent cells are jumpered at one end, and signals are taken in pair from the other ends. A rough estimate of the position (within 10 - 20 cm) is obtained by measuring the time difference for a particular anode signal from the two ends of the paired wire. A fine measurement is made using the information from the cathode pad signals. These vernier cathode pad strips are inserted into the top and bottom of each unit cell [30]. Both the upper and the lower cathode planes are made from two independent electrodes (figure 3.12) forming the inner and outer portions of a repeating diamond pattern with repeat distance of 61 cm. The two inner pads of a given cell are added and read independently of the sum of the outer pads. The ratio of the charge deposited on the inner and outer pads can be used to localize the hit to within ± 3 mm. Each tube also has a single bit output which is set if there were any hits on the cathode pad in that tube (the pad latch) [30] [41, p. 64]. These bits form the input to the muon trigger (chapter 4).

As the magnetic field direction is perpendicular to the beam axis, the muon trajectories are bent in the $r - z$ plane. So, in order to measure the bend, and hence knowing

the muon momentum, its trajectory before and after the iron must be known. The A layer tracks give the trajectory before the magnet and the B - C layers tracks give the after magnet segment of the muon trajectory. Most often the A layer tracks are matched with the central tracking system tracks and to the minimum ionizing particle's trace in the calorimeter to enhance the muon identification and the direction measurement. The muon momentum resolution is dependent on two factors: the multiple Coulomb scattering that occurs in the iron toroid and the position resolution of the hits in muon chambers. Chamber inefficiencies and geometrical misalignment also degrade the momentum resolution. The muon momentum resolution is parameterized as [43]:

$$\left(\frac{\delta p}{p}\right)^2 = \left(\frac{0.18 \cdot (p-2)}{p}\right)^2 + ((0.003 \pm 0.001) \cdot p)^2, \tag{3.5}$$

with p in GeV. The first term is due to multiple Coulomb scattering and the second term comes from the space point drift resolution ($\sim$ 1 mm). This parameterization was determined by comparing $Z \to \mu\mu$ data with the Monte Carlo simulated events where the position resolution was tuned until the width of the $\mu\mu$ invariant mass matched that from the data. The parameterization indicates that below 60 GeV the muon resolution is determined, mainly, by multiple scattering. More relevant parameters [30, 44, 45] of the muon system are listed in table 3.6.

The SAMUS system being in the forward region uses smaller drift tubes to compensate for the high hit rate. It has three stations with three drift tube planes each. Further, each plane is divided into two subplanes with an offset of half a tube diameter. The three PDT layers are rotated with respect to each other. Similar to WAMUS, here also a single sense wire is used. More details on SAMUS system are available in [30, 44, 46]. Some of the SAMUS parameters are tabulated in table 3.6.

	WAMUS	SAMUS
Rapidity coverage	$\|\eta\| < 1.7$	$1.7 \leq \|\eta\| \leq 3.6$
Magnetic field	2 T	2 T
Interaction length	≈ 13.4	≈ 18.7
Number of modules	164	6
Number of drift cells	11,386	5308
Sense wire specifications	50 μm Au-plated W, 300 g tension	50 μm Au-plated W, 208 g tension
Sense wire voltage	+4.56 kv	+4.0 kV
Cathode pad voltage	+2.3kV	—
Gas composition	Ar 93%, CF_4 5%, CO_2 5%	CF_4 90%, CH_4 10%
Bend view resolution	$\pm$ 0.53 mm	$\pm$ 0.35 mm
Non-bend view resolution	$\pm$ 0.3 mm	$\pm$ 0.35 mm
Average drift velocity	6.5 cm/μs	9.7 cm/μs
Maximum drift distance	5 cm	1.45 cm

Table 3.6: Muon System Parameters.

3.3.2 Muon Scintillator Coverage

The DØ muon scintillator counters are the latest addition to the original DØ detector. These counters would provide a coverage on all the six sides of the DØ detector once installed completely. The main idea of having such a coverage is to reduce the backgrounds for the muon detection and to assist the muon drift chamber system (previous section) in pinpointing the exact bunch crossing which initiated the muon trigger. Having a response time in nano seconds these scintillators can provide a time stamp needed to determine the time of arrival of PDT tracks.

These counters are made up of plastic scintillator (Bicron 404A) with maximum

emission around 408 nm, decay constant of 2 ns and bulk light attenuation length of 1.7 m. Depending on where these are placed, the size of these counters varies in length, having width of 25″ and thickness of 0.5″, as 113″, 108″ and 81.5″. One such counter is shown in figure 3.13. These counters use the wavelength shifting fibers (WLS) to carry the scintillations produced in the counter upto the phototube for detection. These fibers (Bicron BCF-91A) are 1mm in diameter with emission in green (494 nm peak) region of the visible spectrum, with 12 ns decay time and an attenuation length of 3.5 m (for a quality study of these fibers see [47]).

These fibers are laid, in a group of four, in the grooves (4 mm wide) running along the length on the scintillator surface. The fibers coming from both the ends of the counters are bundled separately and led to the light tight phototube enclosure through a plastic cookie. These counters make use of two phototubes of EMI make (Thorn EMI 9902KA). The ends of the fibers at the counter edges are coated with Anodized Aluminium and Alcoa Aluminium everbrite tape. The whole counter is wrapped in a light tight Dupont Tyvek wrapping material.

These counters are already placed on the top and on the two sides of the DØ detector. The bottom scintillator counters were under production when this section was written.

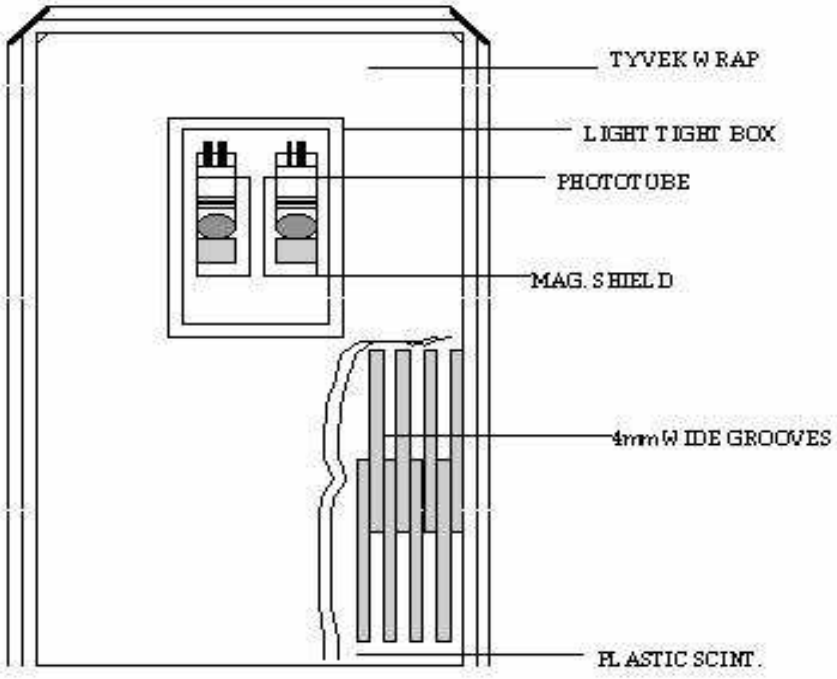

Figure 3.13: A Muon Scintillation Counter (not to scale).

Chapter 4

From Haystack to the Needle

Yes, it is really like looking for a needle in a haystack stored outside your house! In this chapter, we discuss one of the major systems of the DØ detector, i.e. the Triggering system. This system, besides talking to the other DØ detector parts (see previous chapter), takes a first look at the $p\overline{p}$ collisions down the beam pipe and helps us decide what to record and when to record with the help of another system, called the DAQ system or the Data Acquisition System. The basic idea for the triggering is to reduce the number of "unwanted" events, which are in majority.

4.1 Trigger System

At a luminosity of 5×10^{30} cm^{-2}s^{-1}, with a beam crossing rate of about 290 kHz at the interaction region, an inelastic collision will occur in about three-fourth of these crossings [41, p. 67]. So out of these interactions the DØ trigger system selects events of interest, which get recorded finally for the analyses. The block diagram for the DØ

DAQ and trigger system is shown in figure 4.1. The diagram shows the flow of data from the detector to the VMS host machine after passing through the hardware (Level 0 and Level 1) and the final (Level 2) software trigger subsystems.

The first two trigger subsystems (L0 and L1) are responsible for bringing down the event rate from 290 kHz to a rate of 200 - 300 Hz. This reduction of the event rate is based on the trigger decisions which can be made during the beam crossing time of 3.5 μs. The software trigger (or L2) further brings down the event rate to 2 Hz and these events are sent to the host system [41, sec. 3.9] for recording. The details of the three triggering levels are described in the following sections.

4.1.1 Level 0

This is one of the two hardware triggering systems in DØ. This L0 system [48, 49] looks for the beam crossings and detects events resulting from an inelastic scattering. This trigger subsystem consists of two sets of rectangular scintillator tiles mounted on the front surface of each endcap calorimeter (i.e. between each FDC and the closeby EC cryostat). These rectangular shaped scintillators provide almost complete coverage in the range $2.2 < |\eta| < 3.9$ and a partial coverage in the range $1.9 < |\eta| < 4.3$. The inelastic collisions from the beam-beam interactions result in a large amount of activity in the higher eta regions. Thus, the coincidence requirement between the signals from the two scintillator arrays gives L0 trigger an efficiency $> 99\%$ of all non-diffractive inelastic collisions.

The arrival times of the signals from the two level 0 detectors gives a measure of

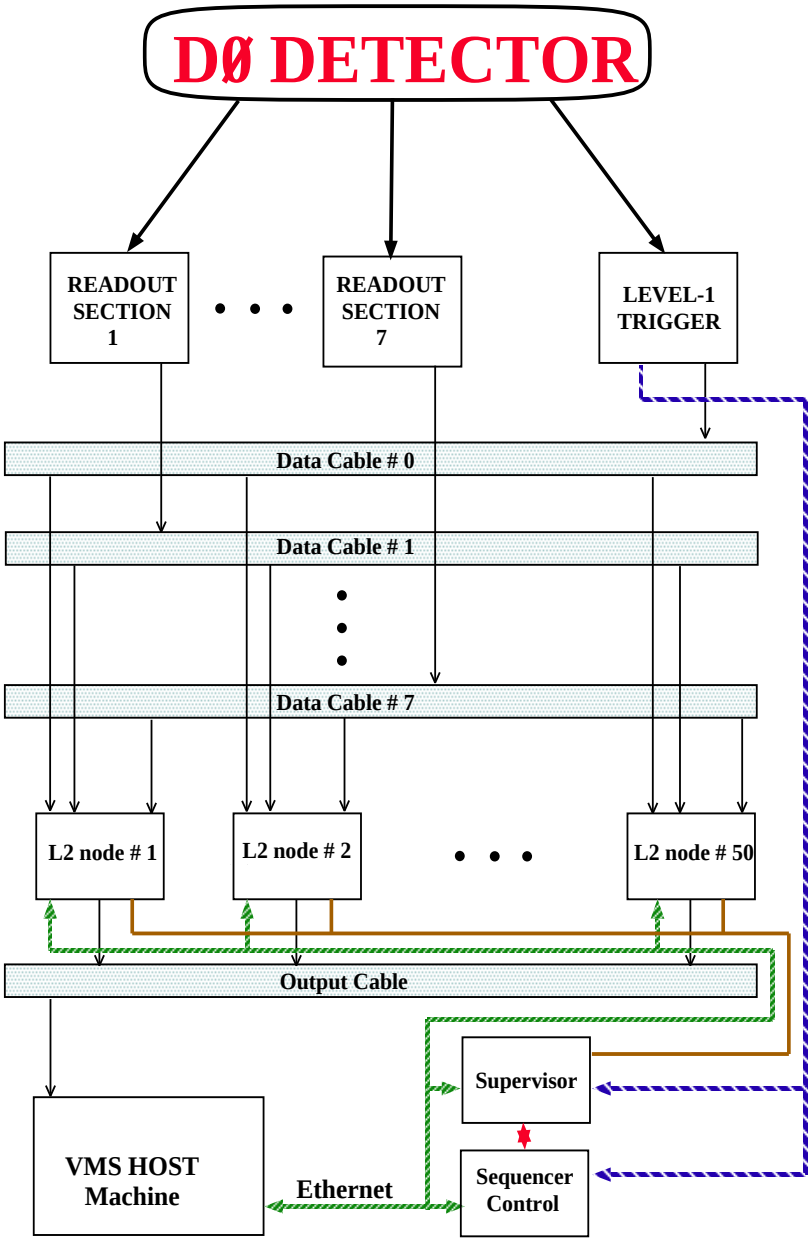

Figure 4.1: Block diagram of the DAQ/Trigger System.

the approximate position of the interaction vertex. One of such measurements [49] [50, p.59] gives a fast estimate of the z-vertex (called fast z), z_f, with a resolution of ± 15 cm within 800 ns after the collision. The second, or more accurate, determination of the z-vertex is available within 2.1 μs with a resolution of ± 3.5 cm. This z-vertex is termed as slow z (z_s). These vertex positions play a big role in the further processing of the event. Like, z_f is used to eliminate beam-gas and beam-halo interactions by applying a vertex cut of $|z_f| < 97$ cm, similarly z_s is used to flag multiple interactions. Further these vertices help in applying various transverse energy corrections by the level 1 and level 2 triggers [51, p. 43].

4.1.2 Level 1

The Level 1 (L1) trigger framework [41, p. 69] is another hardware based trigger system, processing digital signals from level-0, other level-1 components (calorimeter level-1 and muon level-1 trigger), and the timing signals from the accelerator and the host computer [30, p. 233-234]. The trigger framework decides, within 3.5 μs (beam crossing time), whether to keep or reject an event. Then the selected events are passed to the level-2 for further software based selections to be performed. The basic input to the level-1 trigger framework consists of 256 trigger terms (each of a single bit), corresponding to some specific condition being met by the worked out event. These 256 trigger terms are logically combined to give a reduced set of 32 level-1 *trigger bits*.

L1 Calorimeter

As the name implies, this level-1 trigger system is responsible for supplying the digital information from the calorimeter to the trigger framework [41, p. 73-74]. The input to this system comes from the first stage calorimeter electronics, i.e. BLS (baseline subtractor) circuits. These analog inputs are read out in terms of trigger towers, which is formed by summing the output from all the cells in 0.2×0.2 in $\eta - \phi$ space, extending out to $|\eta| = 4.0$. There are separate inputs for cells in the EM and the FH modules (numbering 1280 each). The CH modules are not used for this trigger level. The energies deposited in the trigger towers (for both EM and total) are available after 800 ns of the beam crossing. Following global sums of the calorimeter inputs are calculated by the trigger:

- The total electromagnetic energy, $\mathrm{E}^{em} = \Sigma_i E_i^{em}$.
- The total hadronic energy, $\mathrm{E}^{had} = \Sigma_i E_i^{had}$.
- The transverse electromagnetic energy, $\mathrm{E}_T^{em} = \Sigma_i E_i^{em} sin\theta_i$.
- The transverse hadronic energy, $\mathrm{E}_T^{had} = \Sigma_i E_i^{had} sin\theta_i$.
- The total transverse energy, $\mathrm{E}_T^{tot} = E^{em} + E^{had}$.
- The missing transverse energy, $\not{E}_T = \sqrt{E_x^2 + E_y^2}$, where

  $\mathrm{E}_x = \Sigma_i (E_i^{em} + E_i^{had}) sin\theta_i cos\phi_i$ and $\mathrm{E}_y = \Sigma_i (E_i^{em} + E_i^{had}) sin\theta_i sin\phi_i$.

These quantities are compared with the preset (programmable) thresholds resulting in a trigger term which is then input to the trigger framework.

L1 Muon

This trigger system uses muon system information to indicate the presence of muon tracks in the detector. The inputs to this level-1 muon trigger [52] are the pad latch outputs from the muon system (section 3.3.1). There is one latch bit for each drift cell of the muon system, with a total of 16,700 bits. A latch bit is true if its associated cell has been fired. At level-1, the muon system is divided into five geographical sectors: CF, EFN, EFS, SAMUS-North and SAMUS-South. The trigger looks for patterns of hits which resemble those of a muon emitted from the interaction vertex in these five regions. After counting the number of track candidates in each region, the L1 trigger compares it with a set of preset thresholds and assigns the appropriate trigger term to the level-1 trigger framework.

The level-1 muon trigger requires all the three layers of the muon drift chambers to be hit in most of the regions (but with some exceptions in CF, where there is no third layer coverage). This matching of tracks between the layers gives a very coarse description of the muon in the event and is unable to distinguish between muons of different momenta. So an additional, level-1.5, muon trigger provides more precise muon track and p_T information to level-2 directly. As this precise information requires more computations, specially in the busy SAMUS environment, it takes more than allocated time of 2.4 μs to the level-1. So the presence of level-1.5 trigger is only limited to a small range of η and is not used in the present analysis.

4.1.3 Level 2

After the two hardware triggers, reducing the event rate drastically, it is now the turn for the software trigger system to do the final filtering. Once an event satisfies level-1, full detector read out takes place and level-2 (L2) gears up to run software filters on this event's data. This data is handled by a combination of complex hardware/software, which is described in the next section, before being fed into L2.

L2 trigger [41, p. 76-78] framework resides on a large farm of general purpose processors. Each level-2 farm member or node is a Vaxstation 4000/60 (some of them now upgraded to 4000/90's during run 1b), running the VaxELN realtime OS. The L2 software is composed of a set of *tools* or algorithms which do the filtering job. These tools are FORTRAN routines taking a set of parameters which describes the cuts to be applied on the event. For example, in the EM tool (which finds EM objects) it is possible to require the number of electrons/photons, the minimum E_T of these objects in CC and EC, etc. The value returned by the tool corresponds to either passing or failing of the event. Tools with specific values for the parameters are put together into filter scripts. Corresponding to each script there is an associated level-1 trigger bit. Once all the level-1 bits for an event are available, the corresponding level-2 scripts are called in for all the level-1 set bits. In turn the filter scripts execute the tools embedded in them and if all the tools in a script pass, the script as a whole passes setting up a bit in a 128-bit mask of *filter bits*. If a single, out of 128 bits, bit is set level-2 passes on the event to the host system.

4.2 Host System

The host system comprises of various online utilities which handle the events coming out of the L2 trigger framework. The DØ host cluster [41, sec. 3.9] (backbone of the host system) consists of Vax mainframe computers, disk controllers, etc. The processes being run on this host system can be broadly grouped into four categories: run control, data logging, downloading and monitoring. These processes run as detached server processes communicating with each other and fulfilling requests from users or from other servers besides responding to events taking place in the experiment.

The details of the host system, which have been left out of the discussion here, are available in these references [30, 41]. The overview presented in this chapter is only intended to provide a bare minimum for understanding the data analysis that follows.

Chapter 5

Reconstruction and Identification

In this chapter we will discuss the process of identifying objects and measuring the various qualities of those "identified objects" or particles in the raw data. The raw data or the electronic read outs from the detector, which are just the digitized counts, are of no physics interest till they are translated to the observable entities. The basic idea of having a reconstruction process is to convert these raw quantities into measurable quantities which, in turn, could be used to identify the particles in the event with definite kinematic properties. Thus, the conversion process of turning the raw detector data into particles (such as leptons, jets) is termed as *reconstruction*. This whole cumbersome process is executed by a huge software program called DØRECO.

The reconstruction program starts with the very first step of *hit finding*. This step involves the unpacking of the raw data and the conversion of counts into hits of definite energy and location. The second step involves *tracking and clustering* of these hits. The hits which are closer spatially are grouped together to form clusters in the calorimeter and tracks in the tracking chambers. The last and the final step of the reconstruction

program is the *particle identification* which involves making use of the information from all the detector parts to produce a number of candidate objects for being jets, electrons or muons. During this step the identification criteria is kept quite loose to have high efficiency. More detailed working of the DØRECO package is available in the reference [41]. In the following sections the identification criteria for each object (particle) is described, starting with the vertex finding (crucial one!).

5.1 Interaction Point

The interaction point plays a major role in getting the kinematics correct. In DØ, a detector meant for (high-) p_T analysis, the transverse energy or momentum of a particle are calculated as: $E_T = E\ sin\theta$ and $p_T = p\ sin\theta$, where θ is its polar angle in the lab frame (section 3.1). So, we must know θ for an emerging particle. The only information which is available for a particle being detected in the calorimeter is the location where it deposits energy. In order to get an angle from this direction, another point is needed along its trajectory. This point is fixed by locating the point of $p\overline{p}$ collision from which this particle has emerged. This point is called the *interaction vertex*.

As the collisions are happening in three dimension, so it is necessary to know the x, y and z coordinates of the interaction point. The x and y positions of the vertex can be known quite well because the cross-section of the beam is made as small as possible in these dimensions. This is done to maximize the luminosity. The typical cross-section of the beam was about 50 μm at a location of about 3-4 mm from the center of the detector with a drift of less than 50 μm over the length of a data run [53, p. 14-16]. So,

the position of the interaction point could be taken as constant in x and y or could be set to (0,0) for many purposes.

The third coordinate, z-coordinate, of the vertex needs more work to estimate. The particle bunches in the Tevatron are some what elongated in the beam direction, so this results in a width of about 30 cm in the z-distribution of interaction vertices in the detector. So, it makes it necessary to measure the z-coordinate of the interaction point for each event individually. This is achieved using the track information from the CDC [53, p. 12-13] [54, p. 39-41]. The process involves projecting the tracks found in the CDC back to the center of the detector. Then the impact parameter is calculated and some cutoff is applied to eliminate low-momentum tracks. Each track is projected into the (r, z) plane and the intersection with the z-axis is, thus, computed. Next is histograming the z-positions of the intersections and fitting a Gaussian around the peak of the resulting distribution. The mean gives the estimate of the z-position of the vertex.

This estimate gives a resolution of about 1-2 cm for the z-coordinate of the interaction point. Multiple vertices can be separated if they are at least 7 cm apart [54].

5.2 Jet Reconstruction

A jet is described as a group of colorless hadronic particles emerging out in a fixed direction as a result of the *hadronization* process after a hard scattering has taken place. These closeby particles in a jet appear as a cluster of energy in the calorimeter. At L1, a jet is identified by a trigger tower with E_T greater than some threshold. All such jets are known to the L2 algorithm which is the "cone algorithm". In this, jets are taken to

be comprising of all the energy inside cones of a fixed radius in the $\eta - \phi$ space [55, 56]. Another type of algorithm used in DØ is the "nearest neighbor" algorithm, which is described in the section on electron reconstruction.

Following is the description of the fixed cone jet algorithm which is used in most of the analyses at DØ including this one for the offline reconstruction of jets [57]:

- Preclustering: The L1 calorimeter towers are first sorted in E_T and a set of seed clusters are formed centering on the hottest tower including all the contiguous towers within $|\Delta\eta| < 0.3$, $|\Delta\phi| < 0.3$ and having $E_T > 1$ GeV. These seeds are called "preclusters". Preclustering continues until all towers with $E_T > 1$ GeV are attached to a seed cluster. For each precluster, the E_T weighted centroid defines the axis of the corresponding jet candidate.

- Cone Clustering: Here a new cluster is formed by defining a cone around the precluster axis, which includes all the calorimeter cells within a fixed distance R in η, ϕ space. The E_T-weighted centroid of this cluster defines the new jet axis. The computation of the centroid continues until the axis stabilizes.

- Merging/Splitting: After the cone clustering, if two jets are found to share some cells the fraction of total energy being shared between the two is examined. The two jets are merged into one if the fraction is more than 50% and the jet axis recalculated from the centroid of all the cells in the merged jet, otherwise the jets are split and the shared cells are assigned to the closest jet (whose axis lies closer to it).

- E_T Cut: A jet is required to satisfy some minimum E_T threshold before it could be considered in analyses as one of the event's objects. This threshold is 8 GeV

usually. The jets with radius $R = 0.5$ are used in the present analysis.

The jet energy resolution is measured by using the transverse momentum balance between the two jets in the dijet events. The jet E_T resolution is parameterized as:

$$\left(\frac{\sigma_{E_T}}{E_T}\right)^2 = C^2 + \frac{S^2}{E_T} + \frac{N^2}{E_T^2}, \tag{5.1}$$

where C is a cell by cell error from the calibration, S represents the shower fluctuations in the sampling gap and N denotes the contribution of noise. The resolution in the forward region is worse than in the Central Calorimeter (CC) due to the out-of-cone energy and η resolution effects. In the CC we have $C = 0.0 \pm 0.005$, $S = 0.81 \pm 0.016\,(\mathrm{GeV})^{1/2}$, $N = 7.07 \pm 0.09$ GeV [58].

5.3 Missing Energy Reconstruction

Missing energy in an event implies the presence of neutrinos, which escape detection in the detector. This missing energy is inferred from the imbalance in the total energy deposited in the calorimeter. From the momentum conservation and the colliding proton and antiproton having opposite momenta, it is evident that the vector sum of the momenta of all the final state particles in the event is zero. However, there are many particles going down the beam pipe which escape detection so it is hard to apply the momentum conservation. The only way out is to apply momentum conservation in the plane transverse to the beam as the particles escaping down the pipe have very small transverse momenta. If the resultant sum of the transverse momenta of the detected particles is significantly different from zero, the discrepancy is accounted for to the presence

of one or more neutrinos in the event. The undetected neutrinos must have transverse momentum opposite to the total detected transverse momentum.

Since only the energy of all particles (except muons) is measured by the DØ detector and not the momentum, we replace the missing transverse momentum by an equivalent quantity, missing transverse energy ($\not\!\!E_T$). This is done by assigning each cell of the calorimeter a four-vector with energy that is measured to be deposited in the cell, a direction vector pointing from the interaction point to the center of the cell and a mass of zero. The x and y components of these vectors are summed over all the calorimeter cells (including the ICD) to get the transverse component of energy ($\Sigma_i E_T^i$). Since the missing E_T must balance the total detected E_T in the calorimeter, the negative of $\Sigma_i E_T^i$ gives the "calorimeter missing-E_T" or $\not\!\!E_T^{cal}$. Besides calculating this $\not\!\!E_T^{cal}$, DØRECO also corrects this missing-E_T for the muons, if any, present in the event. Only high p_T muons deposit a small fraction of their energy in the calorimeter, thus the "muon corrected" or total missing-E_T, $\not\!\!E_T$, is just the difference between $\not\!\!E_T^{cal}$ and the transverse momenta of all the good (see chapter 7) muons in the event.

5.4 Electron Identification

Electron identification involves looking for a localized electromagnetic (EM) cluster in the EM calorimeter, having an associated track in the central tracking system pointing back to the event vertex. The electron identification steps followed by DØRECO are:

- *Cluster formation*: Using the nearest neighbor algorithm [59] [35, p. 71-72], clusters are formed from the calorimeter towers. This process starts with the selection

of a highest E_T tower to which the nearest neighbor towers are added so that the tower achieves an E_T threshold, keeping the cluster size fixed.

- *Cluster EM fraction*: This newly formed cluster is required to have $\geq 90\%$ energy in the EM calorimeter and at least 40% of its total energy to be contained in a single tower. This energy requirement checks on the transverse and the longitudinal containment of the shower.

- *Cluster position*: The cluster centroid is computed using the cells in the EM3 layer. The shower centroid is the logarithmically weighted center-of-gravity [60] [61, p. 83-85]:

$$\vec{r}_{\mathrm{COG}} = \frac{\Sigma_i w_i r_i}{\Sigma_i w_i} \tag{5.2}$$

where the weights w_i are defined as

$$w_i = max\left(0, w_0 + ln\left(\frac{E_i}{\Sigma_i E_i}\right)\right) \tag{5.3}$$

where $\vec{r}_i$ is the position of the center of the cell i and E_i is the energy deposited in that cell. w_0 is a parameter chosen to optimize the position resolution, and the sums are over all the EM3 cells in the cluster. The log weighted centroid is used because of the exponential lateral development of an electromagnetic shower. The position resolution achieved is about 1.5–2 mm.

- *Cluster–track match*: The EM cluster finally qualifies as an electron candidate (and stored in the PELC bank) if there is a central detector track pointing to this cluster from the interaction vertex. This track has to lie in a narrow road of dimensions $\Delta\eta = \pm 0.1$, $\Delta\phi = \pm 0.1$. If there is no such track found by DØRECO, the cluster qualifies as a photon candidate (stored in PPHO bank).

After the recognition of an EM cluster as an electron candidate, more selection cuts, specifically required for the analysis, are applied to the EM cluster to fully qualify it as an electron. The general electron selection cuts are following:

- *Shower shape*: Shower shape is one of the primary and powerful tools used for selecting the electrons and rejecting the background. This selection cut is based on a "Covariance matrix" (H–matrix χ^2) analysis [62, 81, 82]. Consider a set of N observations of events of a given type, where each observation comprises of M variables: $\mathrm{x}^n = (x_1^n, ..., x_M^n)$. Then the covariance matrix is

$$V = \frac{1}{N}\sum_{n=1}^{N}(\mathrm{x}_\mathrm{i}^\mathrm{n} - \bar{\mathrm{x}}_\mathrm{i})^\mathrm{T}(\mathrm{x}_\mathrm{j}^\mathrm{n} - \bar{\mathrm{x}}_\mathrm{j}), \tag{5.4}$$

where $\bar{\mathrm{x}}$ is the mean value of the N measurements:

$$\bar{\mathrm{x}} = \frac{1}{N}\sum_{n=1}^{N}\mathrm{x}^\mathrm{n}. \tag{5.5}$$

The H–matrix is the inverse of this covariance matrix, i.e, $\mathrm{H} = \mathrm{V}^{-1}$. To check the pattern of energy deposition in a shower comply to that of an electron, one can define a χ^2 with respect to this H–matrix describing how consistent the shower (measured as y) is with that expected from an electron:

$$\chi^2 = (\mathrm{y} - \bar{\mathrm{x}})\mathrm{H}(\mathrm{y} - \bar{\mathrm{x}})^\mathrm{T}. \tag{5.6}$$

The events x used to build the H–matrix are Monte Carlo electron events. 41 variables are used to characterize the shower, consisting of the fractional energies in layers 1, 2 and 4 of the EM calorimeter, the fractional energies in each cell of a 6×6 array (centered on the tower with maximum energy) in the EM3 layer, the z–vertex position and the logarithm of the total cluster energy. There is a separate matrix for each of the 37 rings into which the calorimeter is divided in $|\eta|$. The

present analysis requires $\chi^2 < 100$ for the electron candidates. Figures 5.1(a),(b) show the χ^2 parameter for electron and background samples.

- *Isolation*: The electron from a W decay is expected to be isolated from other objects in the event. This isolation of electron is measured in terms of an *isolation fraction* (f_{iso}) defined as:

$$f_{iso} = \frac{E_{tot}(0.4) - E_{EM}(0.2)}{E_{EM}(0.2)}, \tag{5.7}$$

where $E_{tot}(0.4)$ is the total energy deposited in all calorimeter cells within a cone of radius $R < 0.4$ ($R = \sqrt{\Delta\phi^2 + \Delta\eta^2}$) around the electron direction. $E_{EM}(0.2)$ is the energy deposited in the EM calorimeter within a cone of radius $R < 0.2$. The present analysis requires $f_{iso} < 0.1$. Figures 5.1(c),(d) show the f_{iso} parameter for electrons from $Z \to ee$ events and from inclusive jet data respectively.

- *Track match significance*: This selection cut is effective against the background from photons which are produced either directly or by the decay of π^0 and η mesons and, in addition, appear to have a track in the central detector (CD) because of some nearby charged particle. In this cut, it is required that the track points accurately at the EM cluster centroid in the calorimeter. The significance of the matching between the track and the centroid of EM cluster is defined [58] as

$$S_{CC} = \sqrt{\left(\frac{\Delta\phi}{\sigma_{\Delta\phi}}\right)^2 + \left(\frac{\Delta z}{\sigma_{\Delta z}}\right)^2}, \tag{5.8}$$

where $\Delta\phi, \Delta z$ are the differences between the cluster centroid and the point where the track hits the calorimeter (in η, ϕ space), and $\sigma_{\Delta\phi}, \sigma_{\Delta z}$ are the measurement resolutions for ϕ and z. The above relation is valid for CC and for EC, z is replaced by r. The distribution of *track match significance*, S, is shown in figures 5.2(a),(b) for electron and background samples. This analysis requires a cutoff at $S < 5$.

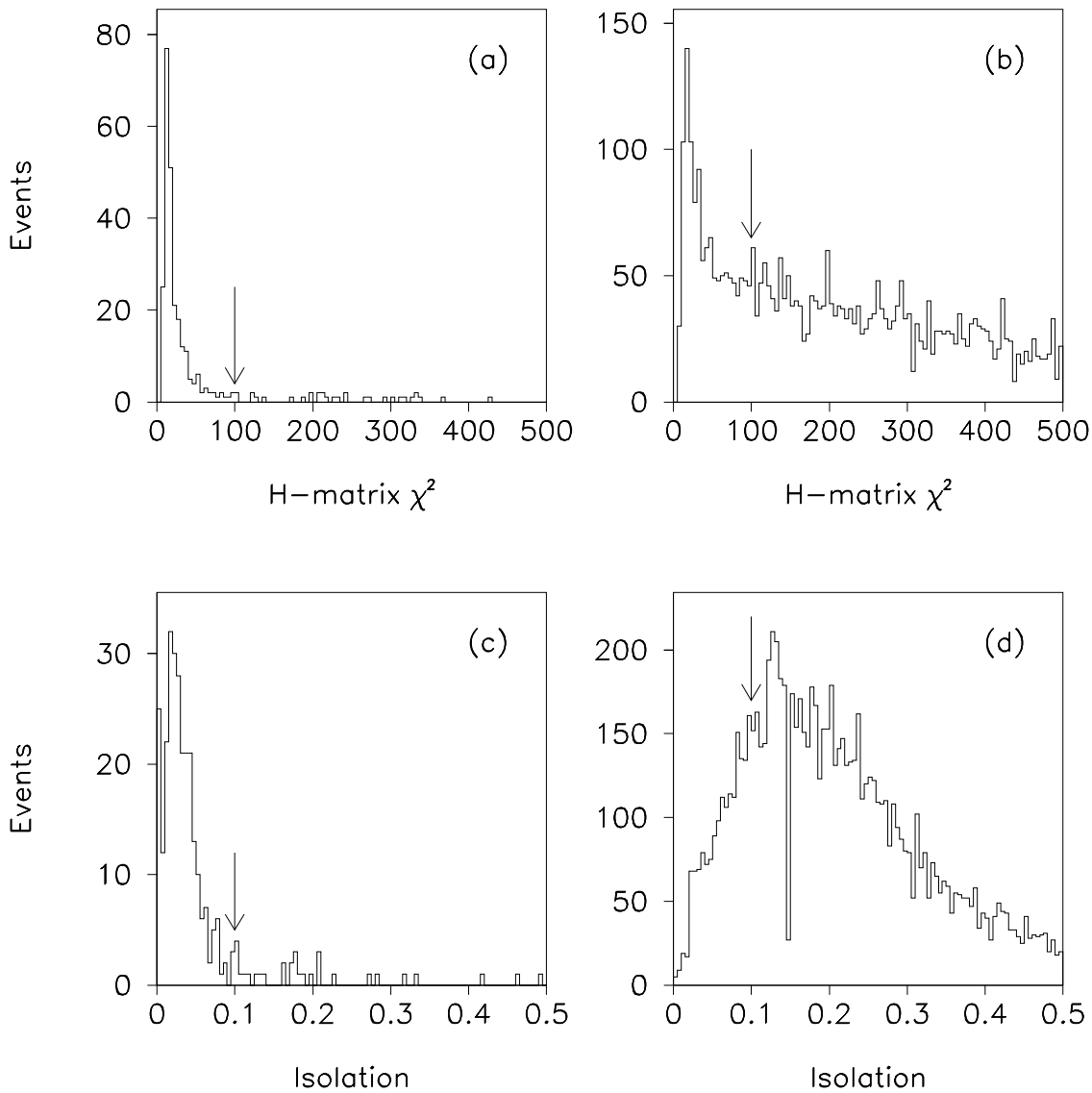

Figure 5.1: H–matrix χ^2 and isolation (f_{iso}) distribution. (a) & (c) are for $Z \rightarrow ee$ events. (b) & (d) are for EM clusters in inclusive jet data.

- *Track ionization*: Photon conversions in the material in front of the tracking system produce e^+e^- pairs. Since DØ has no central magnetic field, the resulting tracks from this pair production are very close and are often reconstructed as a single track. However, the energy deposition per unit length (dE/dx) will be twice that of a single electron (called one MIP, for minimum ionizing particle). Thus, the background due to conversions can be reduced by cutting out the region around 2 MIPs. Figures 5.2(c),(d) show the ionization for electron and background samples.

5.5 Muon Identification

Muons are identified as tracks, in the muon drift chambers, pointing back to the interaction point. Similar to the central detector reconstruction, muon reconstruction involves three steps: hit sorting, track finding, and global fitting. The first two steps make use of the information from the muon system only, whereas the last step, as the name signifies, uses the information from the full DØ detector. These three steps are followed by a number of selection cuts for the quality of the reconstructed muon candidates.

- *Muon Reconstruction*: The muon candidate reconstruction starts by converting the raw hits and the time information into three-dimensional hit positions and then finding those hits which lie on straight lines and point towards the interaction point [63]. Further, the tracking gets complicated because of the magnetic field present between the first(A) and second(B) layers of drift tubes (see section 3.4).

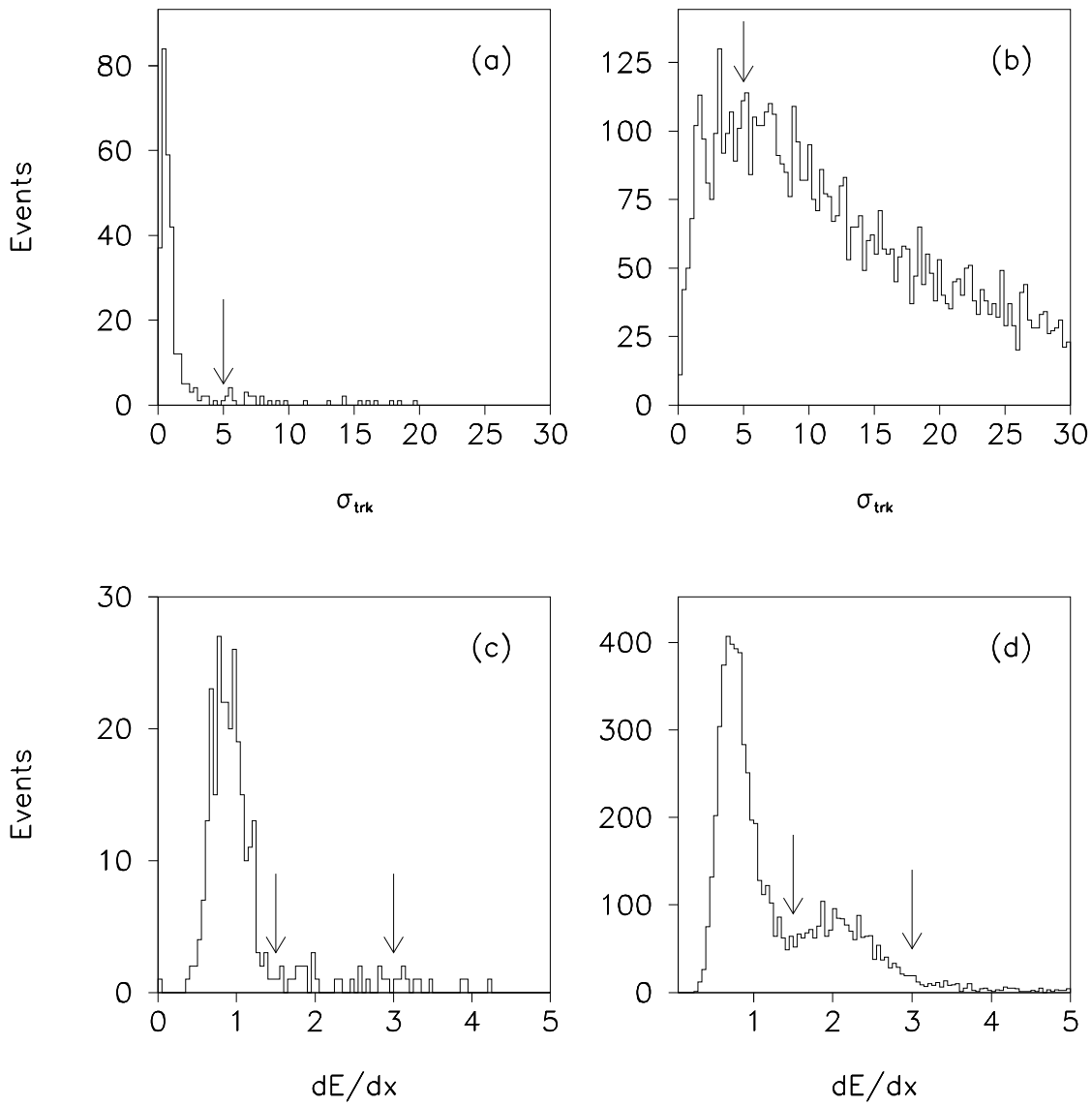

Figure 5.2: Track match significance and track ionization (dE/dx) distribution. (a) & (c) are for $Z \to ee$ events. (b) & (d) are for EM clusters in inclusive jet data.

Thus, tracking is done separately for the two segments, i.e. one before magnet and another after magnet, and then these two segments are matched. The bend in the track, while passing through the magnet, is used to measure the muon momentum. However, this measurement is not very good so another technique, known as *global fitting*, is used to improve the momentum resolution of the muon. In this method, the muon track is associated with a central tracking chamber track and an interaction vertex, thus allowing a better measurement of the muon track before the magnet.

Track quality is defined in terms of quality of fit, number of hits used on the track, the $\int B.dl$ which indicates the amount of magnetic field traversed and the number of muon chambers hit by the track. The energy deposition in the cells along the extrapolated muon track in the calorimeter corresponding to the minimum ionizing energy equivalent to that of a single charged particle gives a good confirmation for the muon and is useful for background rejection. DØRECO also flags the cosmic ray tracks, which could be mistaken for muon tracks, at the track finding level in two ways: The muon system is divided into 8 sections in ϕ (called octants), any track which crosses from one octant to another cannot be consistent with originating from the vertex and is flagged as a cosmic ray. The second way is to look for a track or an excessive number of hits located opposite in η and ϕ to a muon track candidate, as a cosmic ray muon penetrates the entire detector and will leave hits in the muon chambers on both sides of the interaction vertex. The muon momentum resolution is discussed in section 3.3.1.

5.6 Corrections

Several corrections are applied to the energy of the reconstructed objects given by DØRECO. This is because the DØ calorimeter energy scale and the algorithms to implement the energy scale on some objects were finalized during or after the run and hence could not be included in DØRECO.

5.6.1 Electron Energy Corrections

The absolute energy scale of the calorimeters was originally set using test beam calibration data. However, due to differences in conditions between the test beam setup and the DØ installation, this calibration is slightly low. One useful point of reference is the mass of the Z in $Z \to e^+ + e^-$ events, which has been measured very accurately by the LEP experiments [11]. So, the measured electron energies are scaled up so that the mass peak in $Z \to e^+ + e^-$ events matches the LEP measurement [61]. This correction is about 5% in the CC and 1–2% in the ECs. More details about the correction can be found in [64].

5.6.2 Jet Corrections

The basic idea is to know the energy of the original parton which initiates a jet, so we expect the measured jet energy to give back the original parton's energy. However, there are systematic biases in jet measurements which need corrections. From this point of view, there are several effects, in addition to energy scale determination, which have

to be considered due to the extended, multiparticle nature of the jets for making the corrections:

- Most of the particles even in a high-E_T jet will be having low momenta. As the calorimeter response becomes nonlinear in this soft E_T region, so simply summing the calorimeter responses will not give the correct total energy.
- As the hadronic shower is an extended object (in η, ϕ space), the shower may extend beyond the fixed jet cone. In addition, there may be some energy deposited by the particles outside the cone.
- Due to the zero–suppression used in the calorimeter readout and the asymmetric pedestal distribution, there is a systematic shift in energy which scales with the shower size.
- There is always some extra energy added to the jet energy because of the underlying (spectator) event and due to the natural radioactivity of the uranium absorber. These two sources affect jets much more than electrons because of the larger hadronic spread.

The jet corrections at DØ are obtained by a Missing E_T Projection Fraction (MPF) method [41, p. 111-112]. The corrections are first carried out for jets in the central region ($|\eta| < 0.7$) and then extended to the forward region. In this method the EM energy scale is used as the reference. The idea is to look at a sample of events which have a good EM cluster (passing the reconstruction cuts for a photon) and a jet lying opposite in ϕ and no other objects. The EM cluster is corrected using the electron corrections. Further, there should be no energetic neutrinos in these events or ideally

the missing transverse energy ($\not\!\!E_T$) should be zero. This implies that any $\not\!\!E_T$ in the event can be attributed to a mismeasurement of the hadronic jet. By projecting the $\not\!\!E_T$ along the jet axis, the needed correction for the jet can be derived. The projection fraction is given by

$$\text{MPF} = \frac{\vec{\not\!\!E_T} \cdot \hat{n}_t^\gamma}{E_t^\gamma}, \tag{5.9}$$

where $\hat{n}_t^\gamma$ is the unit vector in the azimuthal direction of the photon, E_t^γ. The jet response R_j is then given by $R_j = 1+$ MPF. Out-of-cone showering, underlying event, and noise effects were determined in separate studies using Monte Carlo and minimum-bias event samples. The resulting correction factor which includes contribution of all the corrections described above is shown in figure 5.3 for two different values of η [65].

Once all the above corrections have been applied to the jets in the central region, they are transferred to jets in the forward region by using P_t balance. In this method, dijet events with at least one jet in the central region are used. The correction is obtained by comparing the P_t of the central jet with the P_t of the other jet as a function of the η of the other jet. This method has the advantage that all the corrections are taken care automatically thus avoiding the difficulty of getting the corrections in the forward region.

5.6.3 Missing E_T

As the $\not\!\!E_T^{cal}$ includes a summation over all the calorimeter cells, it implies that if any object in the calorimeter is mismeasured, then $\not\!\!E_T^{cal}$ will be mismeasured by the same amount [66]. So, whenever any corrections are made to electrons and jets, the similar correction must be made to $\not\!\!E_T^{cal}$. This means, as an object is corrected, the uncorrected

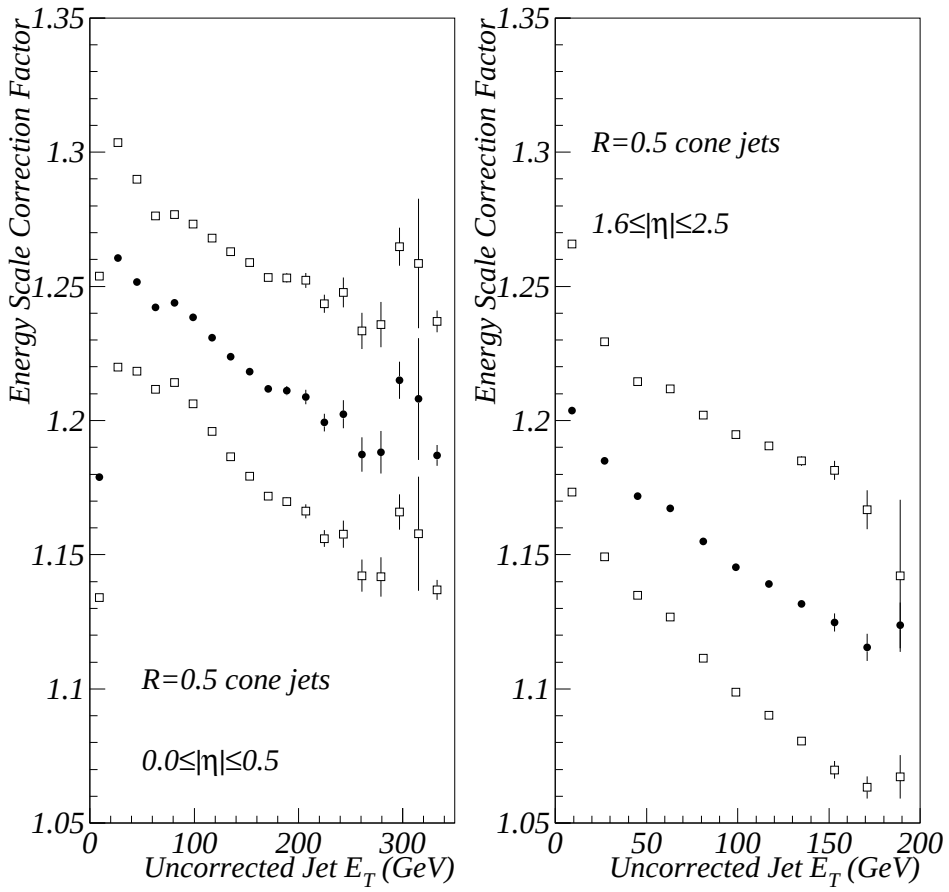

Figure 5.3: Jet E_T correction factors for 0.5 cone jets.

object E_T is added to $\not{E}_T^{cal}$ first and then the corrected object E_T is subtracted out from it.

Chapter 6

Modelling Signal and Backgrounds

The most important thing to know in any HEP analysis, like the one presented here, is the ability to distinguish between the signal and the backgrounds to that signal. The better the ability to separate out the two, better are the chances to observe a clean signal for any new process. For a signal of a new process, like $t\bar{t}$ production, the only way to know the signal details are by doing some sort of theoretical modelling of the process. Same thing is true for getting all the information about all possible backgrounds which could produce signatures similar to that of the top signal. But, there are still some backgrounds which are hard to simulate (section 6.6.2).

The random number based simulation techniques used in the field of High Energy Physics are known as Monte Carlo (MC) techniques. The MC techniques are used for two purposes: (1) to simulate the particle interactions in the collisions, and (2) simulating the detector response to these collisions of particles. These MC simulations help us visualize the physics processes and know the detector responses even before the actual detector fabrication takes place thus saving both money as well as manpower.

The following sections describe briefly the working of a simulator. Various other DØ specific simulators, which are used to make MC events have some real effects (detector specific) folded in, are also discussed here.

6.1 Event Simulator

The MC techniques, used in high energy physics, are usually geared towards the direct simulation of the physical processes. For a quantity of interest, say $\bar{f}$ (a cross section), multiple integrations arise from final phase space and other continuous variables such as momentum fractions of incident partons and fragmentation products. The integrand f can include not only theoretical cross sections but kinematic and geometrical restrictions also. Mathematically $\bar{f}$ is an integral of a weight function $f(x_1 \ldots x_n)$ over variables $x_1 \ldots x_n$ that parameterize the physics. MC methods calculate this integral by generating a random sample of configurations and averaging the integral [13, p. 399].

For hadron-hadron collisions the most commonly used event generators follow the same four basic steps [67]:

- **Hard Scattering**: Based on first order (Born) Feynman diagrams, the cross section for simple two body scattering, $\hat{\sigma}_{ij\to k}$, is used to calculate the contribution to the $p\overline{p}$ cross section with the convolution integral

$$\sigma_{ij\to k} = \int dx_1 \int dx_2 f_i^1(x_1, Q^2) f_j^2(x_2, Q^2) \hat{\sigma}_{ij\to k}$$

  where $x_i = p_i/p$ is the momentum fraction of parton i, Q^2 is the momentum transfer, and $f_i^1(x_k, Q^2)$ and $f_j^2(x_k, Q^2)$ are the structure functions for the proton

and antiproton respectively [67].

- **QCD Evolution**: All partons which participate in the hard scattering are then evolved through repeated parton branchings. The probability $\mathcal{P}$ that a branching $a \to bc$ will take place during a small change in the evolution parameter dt ($t = ln(Q^2/\Lambda^2)$) is given by the Altarelli-Parisi equations [68]

$$\frac{d\mathcal{P}}{dt} = \int dz \frac{\alpha_s(Q^2)}{2\pi} P_{a\to bc}(z)$$

  where $P_{a\to bc}(z)$ are the standard Altarelli-Parisi splitting functions, z is the energy/momentum fraction, and $\alpha_s(Q^2)$ is the strong coupling constant (typically evaluated to first order). The process starts with the maximum allowed mass for parton a then t is successively degraded until a branching occurs. The products, b and c, are then allowed to branch and so on, until a parton mass is evolved below some minimum value (i.e. $t < t_{min} = ln(Q^2_{min}/\Lambda^2)$) when the branching process is stopped. This procedure generates both initial and final state radiation.

- **Hadronization**: Due to the phenomenon of color confinement (see chapter 1), the quarks and gluons which emerge from the QCD evolution cannot continue in color singlet states. Virtual quarks and gluons are pulled from the vacuum (conserving color, charge, etc.) to bind with the original partons and form colorless states. This process is known as fragmentation or hadronization and can not be calculated in perturbative QCD regime, however there are several empirical schemes in which the final state partons are transformed into experimentally observed particles. Most event generators use the Feynman-Field fragmentation scheme [69], with the exception of the standard Lund string fragmentation [70] used in PYTHIA. The Feynman-Field scheme reproduces the limited transverse momenta and approximate scaling of energy fraction distributions found in quark

jets. In this scheme the fragmenting quark is combined with an antiquark from a $q\overline{q}$ pair pulled from the vacuum to produce a hadron with energy fraction z. The remaining quark, with energy $(1-z)$, is then fragmented in the same way, and this process is repeated until the energy of the leftover quark falls below some cutoff. The scaling follows from the energy independence of the distribution assumed for z, which is known as the fragmentation function [71].

- **Beam Fragmentation**: After the hard scattering has taken place, the evolution and hadronization of the leftover beam partons varies from one generator to another. (These leftover partons form a signal in the detector which is known as the underlying event. So it is necessary to model such "spectator" partons' evolution and hadronization along with the hard scattering). PYTHIA uses an extension of the Lund colored string scheme. In ISAJET a minimum bias event is simply superimposed on top of the hard scattering event [72].

After the event generation has taken place, the next step is to look at these events as they evolve inside the detector. Out of a number of event generators, only ISAJET, PYTHIA, and HERWIG generate output compatible to be fed into the detector simulator for the DØ detector directly.

6.2 Detector Simulator

A detector simulator is required to know the response of sophisticated detectors, like DØ, for both the design and development purposes. Performing detector simulations, even before the detector fabrication, give an insight into the range of physics a

detector would be capable of doing. Further, it is necessary to understand the detector acceptance, smearing, and other systematic effects to be used in all the physics analyses of the detector data, here again a detector simulator comes in handy. The detector simulator for DØ is based on version 3.14 of the CERN program GEANT [73]. For DØ, this program is known as DØGEANT. It tracks particles passing through volumes containing user specified materials and performs modelling of interaction and scattering processes correctly, which includes: multiple Coulomb scattering, δ-ray production, full electromagnetic and hadronic showering, electron and muon bremsstrahlung and decays [30]. The resultant response of the detector from these processes is then converted into digitized signals by the DØGEANT program which simulate the raw experimental data.

The GEANT simulation program for any detector involves the exact coding of the geometrical model through which the particles are tracked. For DØ, this geometry information is not hardcoded in the FORTRAN code but, instead, is placed in several ASCII geometry files which are read by the simulation program during the run time. These separate geometry files allow easier editing and alterations of the detector geometry information [74]. Using this information, DØGEANT simulates muon and tracking chambers in great detail, down to the level of sense wires, cathode material, support structure, etc. (however preamps, cables and electronics are not specified in detail).

The CPU time required for doing simulation of a detector of the scale of DØ is enormous, especially the simulation of showering process in the uranium plates and argon gaps of the calorimeter, where DØGEANT generates and tracks hundreds of secondaries through the calorimeter volumes. This requires an approximation of the calorimeter to be used, where all the support structures and individual modules are present but the

calorimeter itself is modelled as homogeneous blocks of uranium-G10-argon mixture. This greatly reduces the number of volumes and hence speeds up tracking. The sampling fluctuations are added after showering for each track and appropriate hadron to electron response, determined from test beam, is introduced. Electromagnetic showers are allowed to evolve until the individual secondary particle energies fall below 200 MeV at which level energies are determined from simple parameterization, again saving CPU time.

6.3 Trigger Simulator

Like knowing the geometrical acceptance for the top signal, by detector simulation, it is also necessary to know how efficient is the trigger framework (chapter 4) in triggering the signal events. As the real data is expected to have a small number of $t\bar{t} \rightarrow e\mu$, the only way to get the trigger efficiency is by doing trigger simulations. DØ has developed a package, TRIGSIM, which comprises of two separate packages namingly: L1SIM and L2SIM. L1SIM operates on Monte Carlo raw data events and simulates level 1 trigger elements. Level 2 is just a software trigger (chapter 4) and the L2SIM (level 2 simulator) just performs a transfer of code from the compact level 2 language (VAXELN) to standard VMS. The trigger simulators make use of the exact same configuration files which go into the real data triggering [75]. These configuration files change depending on the luminosity during the run taking and also with some particular physics studies (called "special run" in DØ language). This is done to control the triggering rates which are very much luminosity dependent, but if the triggers used in an analysis are unaffected by this luminosity change, a configuration file, which is used over large number of runs

of real data recording, can be used to get the trigger efficiency.

6.4 Fine Tuning

The output of DØGEANT is still not an accurate representation of the real data (even after considering the trigger efficiencies). There are, still, a number of variables which are not modeled well in these initial set of simulations. These variables were either not anticipated earlier or they change significantly over short durations. The only way out is to fine tune the Monte Carlo data (GEANT output) for these variations which are difficult to hard code in the simulator packages (saves time and again running of detector simulator with new changes hence cuts short the cpu usage!).

6.4.1 Musmear

The Muon system calls in for the fine tuning due to factors such as alignment uncertainties, muon chamber drift tube efficiency and inefficiencies due to gas leaks and voltage problems. For making these corrections to MC data (by including better calibration and new updated constants) the MU-SMEAR package [76] was created. This package corrects the DØGEANT output data for the above inefficiencies. This package has the response of 164 WAMUS chambers modeled in (independent of DØGEANT). MU-SMEAR uses the following information on simulated muon data to smear the resolutions, drop hits and offset the drift tubes:

- chamber position offset

- fraction of time drift tube ON/OFF
- pad latch efficiency
- drift time signal efficiency
- drift distance resolution in cm
- Δ-time efficiency
- Δ-time resolution in cm

The "new" mu-smeared raw data replaces the uncorrected raw muon data. MU-SMEAR has been tuned so that it correctly reproduces the observed width and tails of the $Z^0 \rightarrow \mu\mu$ mass peak.

6.4.2 Noisy

Another fine tuning is required for the effects of multiple interactions and calorimeter noise (present in the real data) to be added to the MC simulated data. Although the probability of two hard scatterings per beam crossing is extremely low but with increased luminosity during the present run (Run 1b when this analysis is done) is just enough to bring this multiple interactions to a worrisome point. As a result a "good" event might be accompanied by a minimum bias event or two hard scatterings sitting on top of each other with two different vertices. Further, the calorimeter signal for the real data has noise from the uranium and the electronics mixed in. To incorporate these effects in the Monte Carlo data, DØ has developed a package called NOISY [77].

This package simulates the multiple interactions by using a second event input stream which could be either real or geanted MC minimum bias data. A weight is determined based on the Poisson probability $P(N, \bar{N})$ for getting N additional interactions per beam crossing. Based on this weight and the wanted $\bar{N}$, events are then read in from the minimum bias stream and added cell by cell to the current Monte Carlo event.

As per the detector electronics and uranium noise goes, NOISY provides with two possibilities for their simulation. The first method models electronic plus uranium noise as a Gaussian of width and average (user controlled) and adds these values to the calorimeter cells. The second method is a data model based on pedestal distributions from the cosmic ray commissioning run. The ADC counts are then converted to energy and added to the cell noise array. The second method is applicable only to the central calorimeter (CC), for the end caps (EC) and ICD and MG the first, Gaussian, method is used.

6.5 Signal MC

Event samples ($t\bar{t} \rightarrow ll$, where $l \rightarrow e, \mu$ or τ) for seven different top masses ($M_t =$ 140, 150, 160, 180, 200, 220 and 250 GeV/c^2) were generated using ISAJET with the final topology of $t\bar{t} \rightarrow e\mu$ to estimate the signal acceptance. These events ($\sim$ 10K for each top mass) were put through DØGEANT and DØRECO before being subjected to any analysis. These seven different top mass samples were generated using the input cross sections from Laenen *et al.* (chapter 7, section 7.3).

6.6 Background MC

Like the estimation of the signal acceptance, the estimation of the processes which could mimic like the $t\bar{t} \rightarrow e\mu$ signal has to be performed. Such processes are termed as background processes which, as the name itself signifies, interfere in separating out the signal events. The backgrounds to the $e\mu$ channel can be divided into two categories depending upon how they creep in. It could be because of some real physics process which has the topology of the signal or it is the detector which misidentifies one of the objects involved in a process thus making it look like the signal. In the following sections we will discuss, in detail, these both types of backgrounds.

6.6.1 Physics Backgrounds

These backgrounds which arise due to "real" physics processes can be estimated using the standard Monte Carlo techniques (as discussed in earlier sections). Nine such physics processes have been identified as being capable of producing a signature similar to that of a $t\bar{t} \rightarrow e\mu$ event. These are listed below:

- QCD $\rightarrow e\mu$: The large production cross sections associated with QCD multijet processes make it extremely important to fully understand the probability that such a process can produce an isolated electron or muon. Further, the exponentially falling QCD multijet P_T spectrum requires that the Monte Carlo samples be generated in different P_T bins so as to avoid the clustering of events close to zero. The main feature of such processes is the absence of large missing E_T and well isolated electron and muon so this background can be reduced effectively using the

selection cuts described in section 7.2.

- $Z \to \tau\tau \to e\mu$: This background is one of the major backgrounds which has to be looked into carefully. The two τ's are the sources of isolated electrons and muons. But, the back-to-back nature of the τ decays produce a relatively small $\not\!\!E_T$ to be seen in the detector which gives a good rejection tool for this background. Still, the presence of jets, which get mismeasured, would give rise to some $\not\!\!E_T$ in the event. So, requiring two or more jets cut helps in reducing this background.

- $Z \to b\bar{b} \to e\mu$: The electrons and muons from b decay are not well isolated, and the electron E_T spectrum starts falling before 20 GeV. The ISAJET and DØGEANT $Z \to b\bar{b} \to e\mu$ sample's study done concludes that this process is not a significant background.

- $Z \to c\bar{c} \to e\mu$: The leptons from c decay are lower in P_T than those from b decay and are also less isolated, so the contribution from this background will be less than that from $Z \to b\bar{b} \to e\mu$. ISAJET only studies done for this process concluded the contribution from this background to be minimal.

- $W^+W^- \to e\mu$: The great similarity with $t\bar{t} \to e\mu$ events makes this process very hard to discriminate against the top signature. The lepton P_T cut (section 7.2) is not much effective against the high P_T of leptons from W decay. The only effective tool is the jets requirement which gives significant reduction because of the small W pair production cross section ($\approx$ 10 pb [78]). This study was performed using 2500 $WW \to e\mu$ PYTHIA generated events (passed through full DØGEANT and DØRECO).

- $WZ \rightarrow e\mu$: The cross section for this process is about 10 times smaller than that for W pair production so the background contribution from this process was neglected.

- DY: $\gamma^* \rightarrow \tau\tau \rightarrow e\mu$: The ISAJET studies indicate that Drell-Yan dilepton production is not a serious background. Getting high P_T leptons, large $\not{E}_T$ and two or more jets from this process has a very small probability.

- W+jets $\rightarrow$ eμ: The jets in this process are primarily gluon jets, thus the probability of obtaining $e\mu$ events where both leptons are prompt and isolated is very small.

- $W\gamma \rightarrow e\mu$: The studies done with ISAJET, PYTHIA, and the Baur & Zepenfeld Monte Carlo (for generating $W\gamma$ events) indicate that this background process's contribution is negligible [79].

Both ISAJET and PYTHIA were used to generate these events (or otherwise mentioned specifically). To avoid some of the inherent biases in Monte Carlo studies, all input cross sections are based on published values as opposed to those produced by the generator.

6.6.2 Instrumental Backgrounds

The instrumental backgrounds (as mentioned earlier) arise because the detector misidentifies one (or more) of the objects in a real physics process. This type of unusual detector response is not fully understood during the designing stage of the detector, this makes it hard to simulate such "faking" processes using standard event generators. Most prominent instrumental backgrounds are: a jet misidentified as an e, fake muons because

of a hadronic shower leakage (punch through) or due to a cosmic muon. The physics processes which contribute to these fake backgrounds are: $W+$jets, QCD$\rightarrow$ multijets, π/k decays and muon bremsstrahlung. Most of these instrumental backgrounds contribute negligibly [35, p. 113] [42] except the jet faking an electron which is described in greater details in the next chapter.

Chapter 7

Estimations and Expectations

Once we know the types of backgrounds involved with the $t\bar{t}$ signal in the $e\mu$ channel, the utmost task is to know how much each of such a background would contribute to give a certain number of background events (to be expected from the total accumulated luminosity). Similarly for the signal part, it is necessary to estimate the number of signal events expected from the total integrated luminosity. In order to reliably predict how many top and background events we would expect, we must understand all the efficiencies associated with the detector. As discussed in the previous chapter, most of the estimates for the top and the background comes from the Monte Carlo simulations in which particle identification (id) is not well modelled so we make use of real data to get the particle id efficiencies, whenever possible.

In this chapter, we, first, discuss the steps involved in getting all the input efficiency numbers, correction factors and the raw acceptances for both the top signal and background, then in the later part of the chapter we combine these together to get an estimate of the expected top and background events.

7.1 Input Efficiencies

The input efficiencies tell us how well the detector can identify the decay objects, i.e., electron and muon coming from the $t\bar{t}$ system. Knowing all sorts of efficiencies is the first step of any analysis to be performed on the real data. All the estimates for the background and the top signal are based on these efficiencies which are: electron id efficiency, electron tracking efficiency, muon id efficiency and triggering efficiency. The basic criteria to get these efficiency numbers is to apply object quality cuts on a known sample of events (from real data) and see how many events survive the cuts, where by "a known sample" it means the sample with known distributions and calibrated to some fixed reference (like $Z \to ee$ used for obtaining the electron efficiency).

7.1.1 Electron Efficiencies

For electrons, the detection efficiencies vary with cryostat (CC and EC) and depend on the choice of electron id. To incorporate data based efficiencies, the procedure is as follows: the Monte Carlo efficiencies are determined without any electron id requirements (only EM cluster Isolation (f_{iso}) is required to be < 0.1) and then multiplied by the appropriate electron id efficiency determined from data. The best data sample available for signal (electrons like those from W decays) comes from $Z \to e^+e^-$ candidates (selected by requiring the invariant mass of the two PELCs to be around the Z mass peak) and for background (needed for comparison with the signal electrons) a sample with only a single PELC and low $\not{E}_T$ (to discriminate against W's and Z's) was used. The final electron efficiency, ε^e, is, in fact, a product of two separate efficiencies: electron

id efficiency (ε^e_{id}) and electron tracking efficiency (ε^e_{trk}) which is just the probability to find a track in the road (to reconstruct a PELC).

To get the ε^e_{id} number (for both CC and EC), the two parameters used are: (i) isolation parameter (f_{iso}) and (ii) electron likelihood [80]. The first parameter is described in chapter 5 (section 5.4), here we describe the second parameter used for getting the electron id efficiency.

- Electron Likelihood: The two main sources for the fake electrons are: low energy charged hadrons spatially overlapping the energetic photons from π^o or η decays and the e^+e^- from isolated photon conversions. The conventional procedure [81, 82] for cutting down the fake electrons includes cuts to be applied on the electron quality variables (see section 5.4), namingly: H-matrix χ^2, track match (σ_{trk}), track ionization (dE/dx) and EM energy fraction (f_{EM}). However, we found that a multidimensional likelihood calculation (the Neyman-Pearson test [83, 84]) gives better rejection of these backgrounds than the individual cuts on these variables.

  Let x be a 4 dimensional column array consisting of the four parameters mentioned above. The probability $p(x|e)dx$ (or $p(x|b)dx$) represents that these four parameters for a signal (or background) event fall in the interval $[x, x+dx]$. These four parameters are assumed to be statistically independent, although there is apparently some correlation between the H-matrix χ^2 and f_{EM} yet this is still a good approximation. Based on the assumptions, the probability density functions $p(x|h)$ for signal ($h = e$) and backgrounds ($h = b$) are, then, computed using the formula

$$p(x|h) = p_1(\chi^2|h) \cdot p_2(\sigma_{trk}|h) \cdot p_3(dE/dx|h) \cdot p_4(f_{EM}|h),$$

	ε^e_{id}	ε^e_{trk} $(\frac{\varepsilon^e_{trk}(data)}{\varepsilon^e_{trk}(MC)})$	Electron Eff.
CC	0.831 ± 0.005	0.872 ± 0.013	0.725 ± 0.012
EC	0.779 ± 0.015	0.939 ± 0.020	0.731 ± 0.021

Table 7.1: Electron efficiencies for CC and EC.

where $p_i(x_i|h)$ is the probability distribution function of variable x_i and $h = e$ for real electrons and $h = b$ for fakes. To implement the density functions, each distribution is normalized and split into bins (50-100 bins are used for each distribution). The probability of each bin in each distribution is given by the integral of the probability density over that bin. So $p(x|h)$ is a product of four individual probabilities, one each corresponding to which bin x_i falls into.

A PELC, denoted by a 4 dimensional array x', is considered to be an electron if it passes the likelihood test:

$$\mathcal{L}_e \equiv \frac{p(x'|b)}{p(x'|e)} < k.$$

The electron id cuts require $\mathcal{L}_e < 0.5$ for the electrons in the CC and $\mathcal{L}_e < 1.0$ for those in the EC. The $f_{iso} < 0.1$ cut is applied to both the CC and EC electrons. The efficiencies (ε^e_{id}) corresponding to these id cuts are listed in table 7.1. The product of the tracking efficiency [85] (ε^e_{trk}, table 7.1) and ε^e_{id} gives the final electron finding efficiencies for CC and EC.

7.1.2 Muon Efficiencies

The muon efficiency is not yet fully data driven as that for electrons. So, the procedure is slightly different: we obtain the muon id efficiencies by making the final muon quality requirement on Monte Carlo data, then we multiply these efficiencies by an additional "scale-down" factor as determined from the mu-smear (section 6.4.1) which is data driven. The quality of a muon candidate depends on various factors. To separate out good muons (definition of "good" varies with analyses), a set of selection cuts are applied on the reconstructed muon tracks [58] [50, p. 70-83] in the Monte Carlo data, which are:

- Fiducial Cut: The muon is required to be either in CF (muon quadrant ≤ 4) or in EF ($4 <$ muon quadrant ≤ 12).
- A-stubs: The muon can not be an A-stub (Muon A layer only track).
- Track Quality (IFW4): Good χ^2 on track fit is required, (IFW4 ≤ 1 for CF and ≤ 0 for EF), implying the muon track is consistent with originating from the reconstructed vertex in the bend and non-bend views (section 3.3.1).
- MTC confirmation: MTC stands for muon tracking in calorimeter. Muons typically deposit 1 to 3 GeV of energy in the calorimeter and leave a distinctive energy signature over the total path length. The MTC package [86] (included in DØRECO) uses the event vertex position and the muon candidate information to identify and reconstruct a track-like energy deposition in the calorimeter. The quality of fit depends on the fraction of calorimeter layers used to get a fit. The two parameters used in muon identification in the calorimeter are:

mu_smear CF	mu_smear EF
0.91 ± 0.05	0.295 ± 0.1

Table 7.2: Muon efficiency correction factors for CF and EF.

- HFRAC: It is defined as the fraction of hadronic calorimeter layers used for the track fit out of the total possible. Ideally good muons will have HFRAC = 1, in that case all possible layers are used for the track fit.
- EFRAC_H1: The energy fraction of the last hadronic layer out of the total for a cluster of 3×3 towers; usually only muons deposit energy in the last layer.

The cut off requires, HFRAC = 1 or, HFRAC ≥ 0.7 and EFRAC_H1 > 0.

- Isolation: The muon should be well isolated (from any nearby jet activity) in η and ϕ (or ΔR). The cut off requires $\Delta R_{\mu,jet} \geq 0.5$ for all reconstructed jets in the event.

Muon Correction Factors

There are two correction factors which must be applied to monte carlo data, one from mu-smear (section 6.4.1) and another due to the phi hole. This phi hole factor is valid only for the beginning of the run 1b, known as "prezap" period. Due to the chamber aging, some of the muon chambers were dropped from the fiducial region cut thus giving an inefficiency factor. Later on after the fixing of the muon chambers, "postzap" period, this extra factor was dropped from the calculations. The final scale down factors due to these corrections are listed in table 7.2. The EF mu_smear correction factor has been

CCCF	CCEF	ECCF	ECEF
$0.95 \pm .05$	$0.93 \pm .05$	$0.90 \pm .04$	$0.93 \pm .05$

Table 7.3: Trigger efficiencies.

computed by scaling the "postzap" efficiency by the fraction of luminosity accumulated during the postzap period vs the total luminosity.

7.1.3 Trigger Efficiencies

These efficiencies are based on the TRIGSIM studies (see section 6.3). The four triggers used for collider data, from run 1b, are discussed in section 8.2. The TRIGSIM studies, based on the OR of these triggers, give the trigger efficiencies for CCCF, ECCF, CCEF and ECEF (four physics partitions of the DØ detector for efficiency purposes) listed in the table 7.3.

7.2 Selection Cuts

The motivation, which drive the following selection cuts, is to reduce the backgrounds described in section 6.4 and at the same time enhance the top signal detection efficiency. With both the samples (MC), signal as well as background, in hand, we apply the kinematical cuts to get the raw acceptances (which include the geometrical acceptance also). Keeping the above mentioned motivation in sight, we try to optimize the kinematical (selection) cuts so as to have a good signal to background ratio. This is achieved by calculating the expected event yield for both the signal and the background.

Cut Number	Cut Definition
1.	$E_T^e > 15$ GeV, $p_T^\mu > 15$ GeV/c + $\|\eta\|$ cuts
2.	Require Isolated muons: $\Delta R_{\mu,jet} \geq 0.5$
3.	$\not{E}_T^{cal} > 20$ GeV (calorimeter/ICD/MG)
4.	$\not{E}_T > 10$ GeV (muon corrected)
5.	$\Delta R_{e\mu} > 0.25$
6.	Require 2 jets, $E_T^{jet} > 15$ GeV
7.	H_T $(E_T^e + \sum E_T^{jet}) > 120$ GeV
8.	2 jets, $E_T^{jet} > 20$ GeV

Table 7.4: $e\mu$ selection cuts.

Then, these fine tuned cuts are applied to the detector data to look for the top quark signal (see next chapter).

At the Monte Carlo level, to get the signal and the background estimates, only the full muon id (section 7.1.2) requirement is made for the selection of events. For electrons, where the efficiencies are completely data driven (section 7.1.1), only the Electron Isolation ($f_{iso} < 0.1$) cut is made on the MC data. The selection cuts for the event selection criteria are listed in table 7.4. These cuts follow the above mentioned motivation to reduce the background as follows:

- Cut 1 & 2: The cuts on $E_T^e > 15$ GeV and $p_T^\mu > 15$ GeV/c are made primarily to reduce the background coming from b and c quark decays (from QCD multijet events, $Z \to b\bar{b}, c\bar{c} \to e\mu$). These background processes do produce relatively high p_T muons which are not isolated as compared to the well isolated muons from W decay (in the standard $t\bar{t}$ decay scheme). The muon isolation requirements (MTC

confirmation and $\Delta R_{\mu,jet}$, i.e. Cut 2) made for the muon identification (section 7.1.2) criteria reject these backgrounds. Cut 2 requires that the muon and jet be well separated because a typical non-isolated muon is very close to a jet. The MTC confirmation cut looks deeper in the hadronic layers of the calorimeter for the energy deposited by a muon.

- Cut 3: The third cut requires the Calorimeter missing E_T or $\not{E}_T^{cal}$ to be more than 20 GeV. Since neither muon nor the neutrino are seen by the the calorimeter, a measurement of the $\not{E}_T^{cal}$ is equivalent to a measurement of the P_T of the W. A cut of 20 GeV on this quantity reduces the major instrumental background of W + jets $\rightarrow \mu$ + jets, where one of the jets is misidentified as an electron. Where as this cut has little effect on the $t\bar{t}$ acceptance since for $t\bar{t} \rightarrow e\mu$ events, the $\not{E}_T^{cal}$ is derived from the high E_T electron and b jets. Figure 7.1(a) shows the $\not{E}_T^{cal}$ distribution for the top180 sample after the e, μ identification cuts and the muon isolation cuts. The arrow mark shows the cutoff value. Figures 7.2(a) and 7.3(a) show the $\not{E}_T^{cal}$ distribution for the two major backgrounds, *i.e.* $WW \rightarrow e\mu$ and $Z \rightarrow \tau\tau \rightarrow e\mu$.

- Cut 4: The muon corrected $\not{E}_T$ is due to the two high P_T neutrinos present in the $t\bar{t} \rightarrow e\mu$ events. One of the major backgrounds to produce so much $\not{E}_T$ is $Z \rightarrow \tau\tau \rightarrow e\mu$. A cut off at $\not{E}_T > 10$ GeV reduces the cross section of this background significantly.

- Cut 5: A high P_T muon will occasionally be accompanied by initial state bremsstrahlung and the majority of these photons will be very close to the parent muon (in $\eta\phi$ space). In such a situation the photon will be matched to the muon track in the central tracking system and will be labeled as an electron by DØRECO and thus creating an $e\mu$ event. The fifth cut requires $\Delta R_{e\mu} > 0.25$

which effectively removes such events while having no effect on the $t\bar{t}$ acceptance.

- Cut 6: The sixth cut requires the presence of two jets with $E_T > 15$ GeV. This cut reduces the $WW \to e\mu$, $Z \to \tau\tau \to e\mu$ and W + jets backgrounds.

- Cut 7: At this stage most of the backgrounds are reduced significantly by the above selection cuts but the most pronounced of all the backgrounds *viz* $Z \to \tau\tau$ and WW are still prevalent. The final cut of $H_T > 120$ GeV, where H_T is just the scalar sum of E_T^e (leading electron) and $\sum E_T^{jet}$ (all jets within $|\eta| \leq 2.5$ and having $E_T \geq 15$ GeV), efficiently cuts down these backgrounds. Since the top quark is heavy, and hence top events are more spherical than background events and are produced more centrally in the detector, this cut does not affect the top signal much. Figure 7.1(b) shows the H_T distribution for top180 sample after the e, μ id and muon isolation requirements. The arrow at 120 GeV shows the cutoff mark. Figures 7.2(b) and 7.3(b) show the H_T distribution for WW and $Z\tau\tau$ background samples.

- Cut 8: Finally the jets E_T cut is tightened to 20 GeV. This cut, drastically, cuts down all the WW pair, $Z \to \tau\tau$ and W + jets $\to \mu$ + jets(e) backgrounds whereas having very little effect on the signal. Figure 7.1(c) shows the distribution for number jets with $E_T > 20$ GeV present in top180 sample after the e, μ id and muon isolation requirements. Figures 7.2(c) and 7.3(c) show the number of 20 GeV jets present in WW and $Z\tau\tau$ background samples.

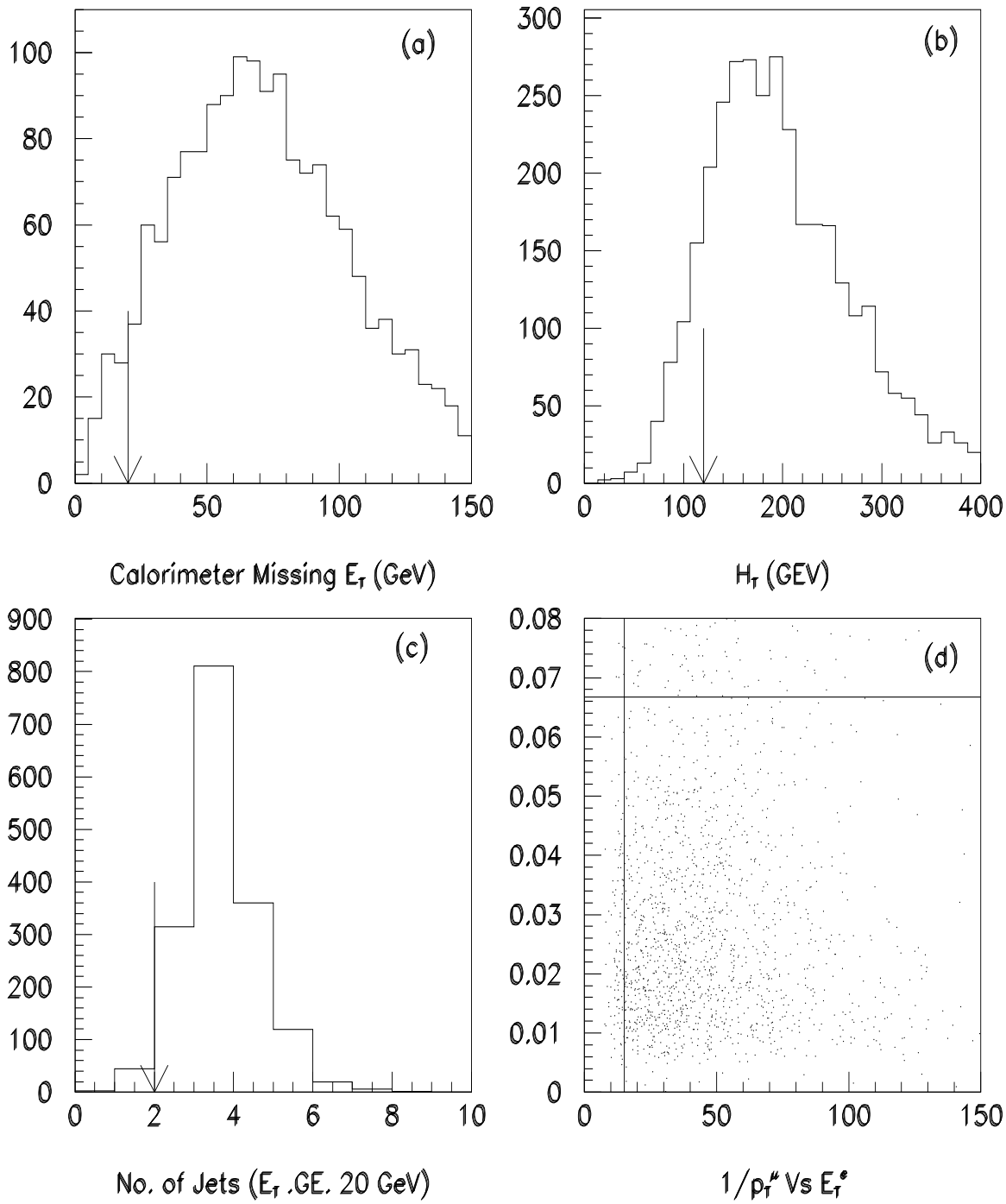

Figure 7.1: (a) $\not{E}_T^{cal}$, (b) H_T, (c) number of jets ($E_T > 20$ GeV), (d) $1/p_T^\mu$ Vs E_T^e distributions for top180 MC (after the e, μ id and muon isolation requirements).

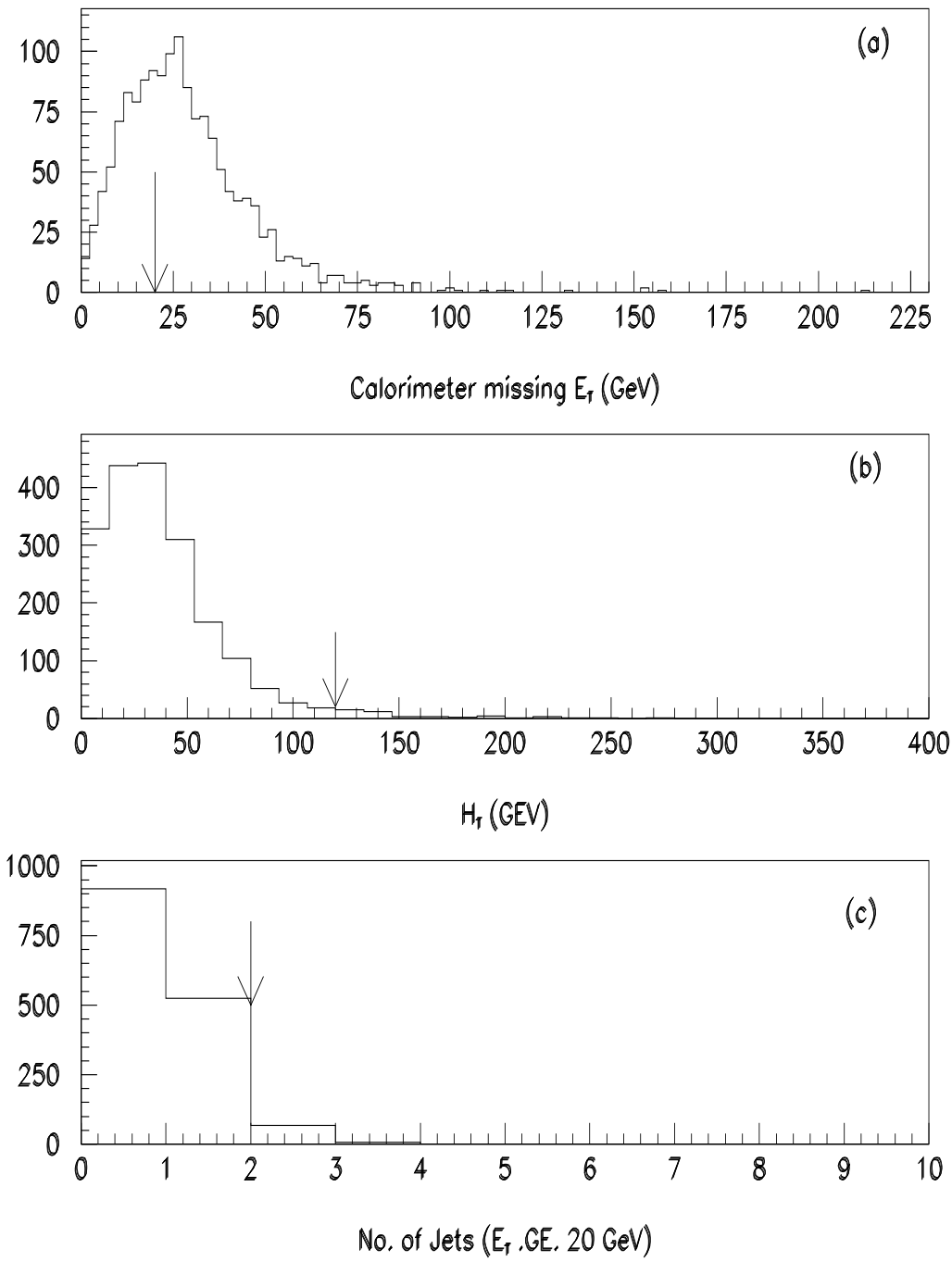

Figure 7.2: (a) $\not{E}_T^{cal}$, (b) H_T, (c) number of jets ($E_T > 20$ GeV) distributions for $Z \to \tau\tau \to e\mu$ background.

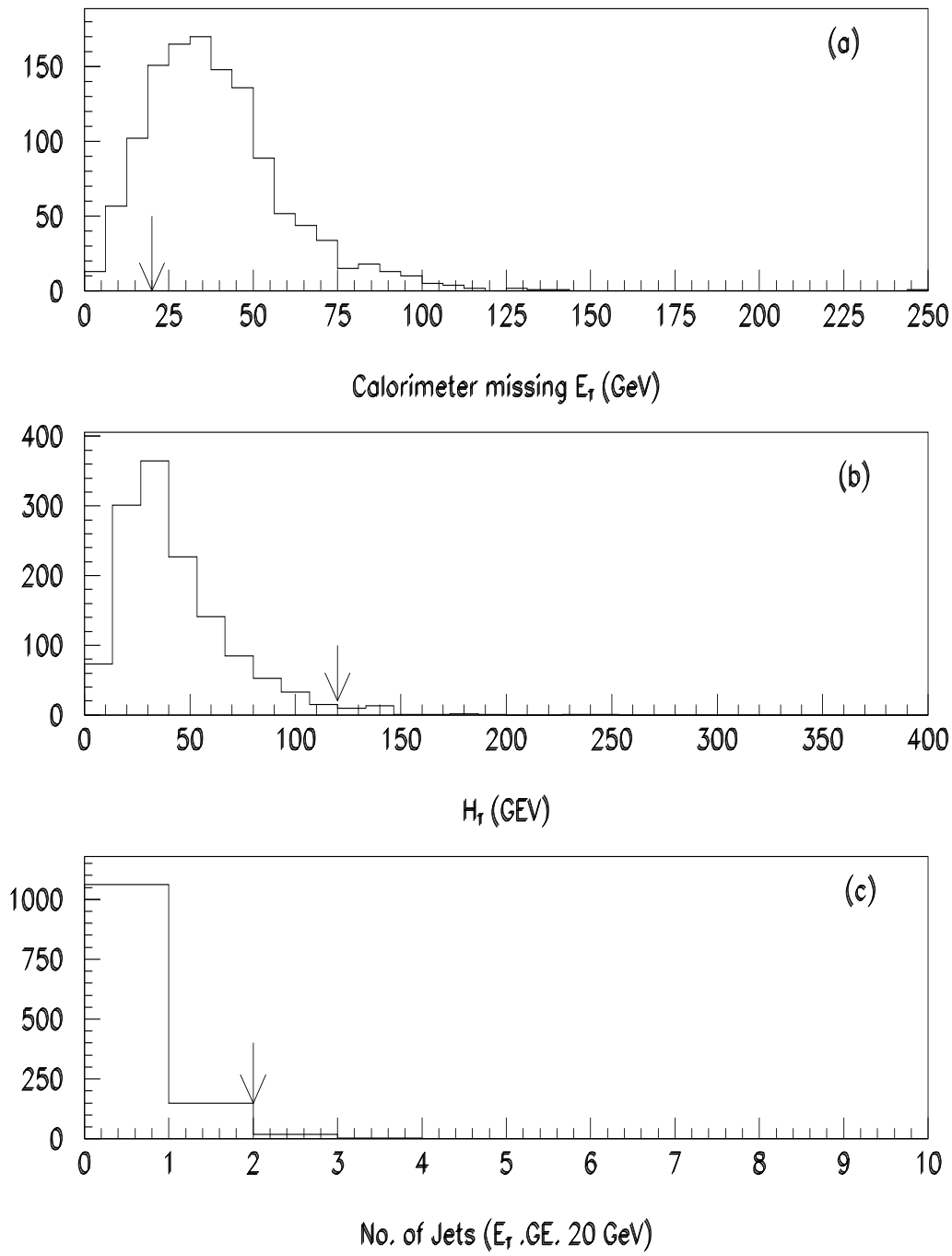

Figure 7.3: (a) $\not{E}_T^{cal}$, (b) H_T, (c) number of jets ($E_T > 20$ GeV) distributions for $WW \rightarrow e\mu$ background.

7.3 Acceptances for $t\bar{t} \rightarrow e\mu$

After getting the selection cuts optimized, we apply these cuts to the samples of different top masses. The ratio of events left after these cuts to the total number of input events gives the selection cut efficiency. Once we have this acceptance, the next step is to get the overall top detection efficiency (ε) which is the product of all the efficiencies we discussed in section 7.1 and the selection cuts efficiency. Table 7.5 gives the final acceptances, *i.e.* efficiency $\times$ branching fraction for different top masses.

M_t (GeV/c^2)	$\varepsilon \times Br$
140	0.280 ± 0.048
150	0.330 ± 0.058
160	0.416 ± 0.071
180	0.456 ± 0.079
200	0.501 ± 0.087
220	0.503 ± 0.088
250	0.781 ± 0.127

Table 7.5: Acceptances for $t\bar{t} \rightarrow e\mu$ production.

The errors quoted in table 7.5 include both statistical and systematic errors (added in quadrature). The systematics contribute about 17% of the total error and the breakup is given in table 7.6. The standard DØ luminosity error used is 5.4%. The ultimate aim is to estimate the number of top events expected with the above acceptances. The number of expected events is given by the formula:

$$n = \sigma \times Br \times \varepsilon \times \mathcal{L}$$

Source	% error
1. Energy scale	5
2. Electron Efficiency	~ 0.8
3. High p_T muon efficiency	~ 11
4. Non-muon trigger efficiency	5
5. Multiple interactions	5
6. Top quark generator	10

Table 7.6: Systematic errors.

where

σ is the $t\bar{t}$ production cross section central value from Laenen *et al* [18], ε is the final detection efficiency, $\mathcal{L}$ is 76.6 pb^{-1}, the total integrated luminosity for run 1b (see next chapter), and finally, Br is the total branching ratio for $t\bar{t}$ going to $e\mu$. This Br includes the fraction of $e\mu$ events coming from the decays like: $t\bar{t} \to e\tau \to e\mu$, $t\bar{t} \to \mu\tau \to e\mu$ and $t\bar{t} \to \tau\tau \to e\mu$ besides the standard $t\bar{t} \to e\mu$ (section 1.5 and [35, appendix A]).

The number of top events expected from 76.6 pb^{-1} of integrated luminosity and $\sigma_{t\bar{t}}$ (central value) from Laenen *et al.* for various top masses are tabulated in table 7.7. Figure 7.4 shows the final acceptance for various top masses (lower curve) and the expected number of top events versus the top mass (upper curve), and figure 7.5 shows the Laenen *et al.* central value $t\bar{t}$ production cross section versus the top mass. The errors in table 7.7 include both the statistical as well as systematic errors (added in quadrature). Besides the 17% systematic error (table 7.6) described before, there is 5.4% luminosity error to be added to this plus the error on $\sigma_{t\bar{t}}$ is taken from Laenen *et al.* (figure 7.5) which varies with top mass.

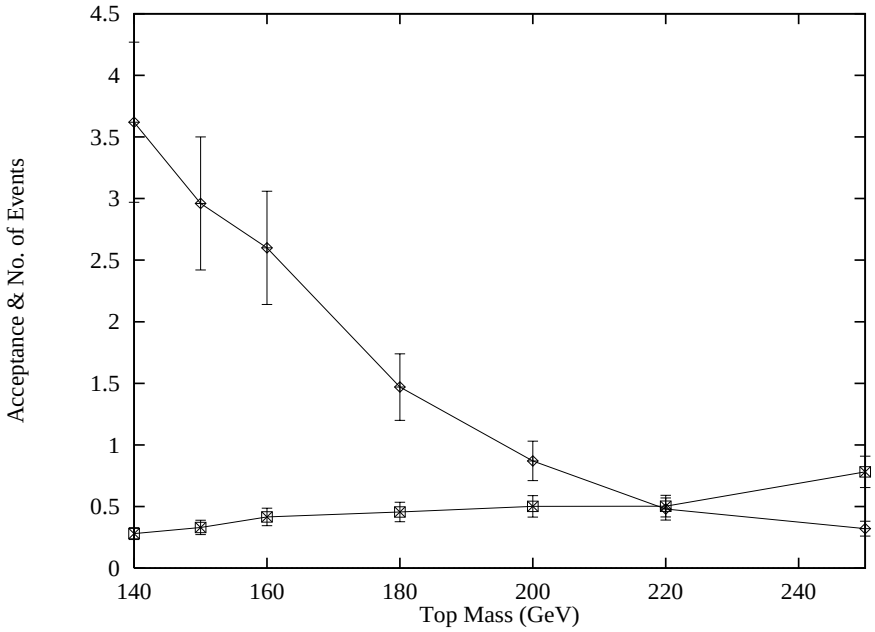

Figure 7.4: Acceptance (boxes) and Expected event yield (rhombuses)Vs M_{top}.

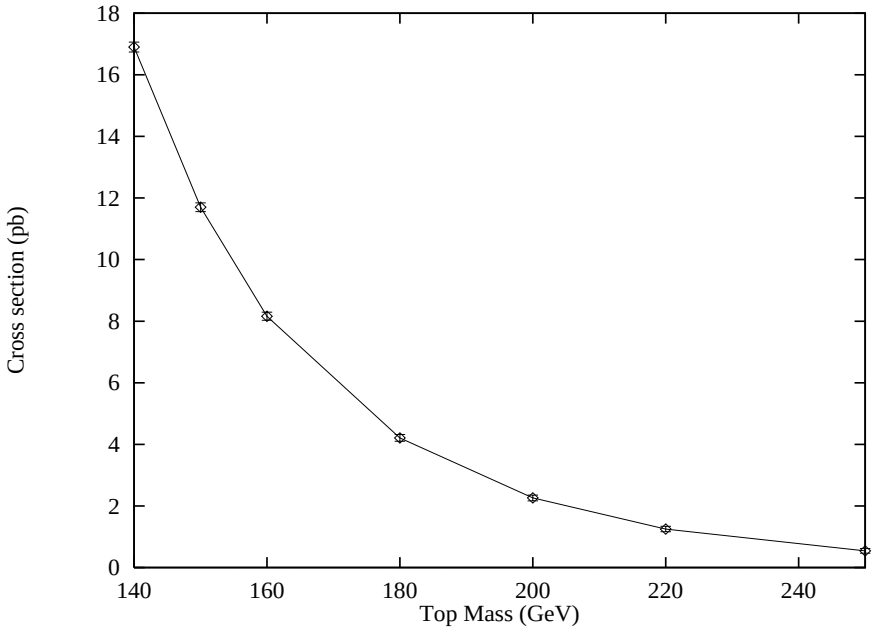

Figure 7.5: Laenen *et al.* $\sigma_{t\bar{t}}$ central value Vs M_{top}.

M_t (GeV/c^2)	$\sigma_{t\bar{t}}$ (pb)	events from 76.6 pb^{-1}
140	16.9 ± 0.160	3.26 ± 0.65
150	11.7 ± 0.141	2.96 ± 0.54
160	8.16 ± 0.130	2.60 ± 0.46
180	4.21 ± 0.109	1.47 ± 0.27
200	2.26 ± 0.095	0.87 ± 0.16
220	1.25 ± 0.088	0.48 ± 0.09
250	0.54 ± 0.074	0.32 ± 0.06

Table 7.7: $\sigma_{t\bar{t}}$ and number of top events expected from 76.6 pb^{-1}.

Background	Number of events in 76.6 pb^{-1}
$WW \to e\mu$	0.0240 ± 0.0116
$Z \to \tau\tau \to e\mu$	0.2629 ± 0.0697
DY: $\gamma^* \to \tau\tau \to e\mu$	0.0148 ± 0.0258

Table 7.8: Number of physics background events from 76.6 pb^{-1}.

7.4 Background Estimation

The background estimation involves a similar procedure like the one used in the previous section to estimate the number of signal (top) events. The selection cuts described in section 7.2 are applied to the background samples (Monte Carlo geanted and reconstructed events, see section 6.6). The major physics backgrounds (section 6.6.1) are $WW \to e\mu$, $Z \to \tau\tau \to e\mu$ and DY: $\gamma^* \to \tau\tau \to e\mu$, which are the processes contributing to the total background for the $e\mu$ channel. The rest of the processes: $QCD \to e\mu, Z \to b\bar{b} \to e\mu, Z \to c\bar{c} \to e\mu, WZ \to e\mu, W + \text{jets} \to \text{e}\mu$ and $W\gamma \to e\mu$ do not contribute significantly to the background. The number of physics background

events expected from 76.6 pb^{-1} are tabulated in table 7.8. The errors in table 7.8 include both statistical and systematic errors (added in quadrature). Error on the input cross sections is taken to be $\sim$ 10% and the systematic error due to MC simulations is taken to be about 8 $\sim$ 9% and rest of the systematic error sources are listed in table 7.6 (excluding top quark generator). The standard DØ luminosity error of 5.4 % is also included in the total error.

To estimate the instrumental or fake backgrounds (section 6.6.2), we use the detector data to get the number of fake events expected. The most significant of all the processes which could appear as an $e\mu$ event because of detector misidentification is W + jets $\rightarrow \mu$ + "fake" e (from one of the jets). The procedure to make this estimate is following: We obtain a sample which passes all kinematic constraints imposed in the analysis and also passes the same triggers as the signal events. No electron id (section 7.1.1) requirement is made on the sample and then the number of unbiased jets (JETS bank) are counted. This number is then multiplied by the "fake rate" obtained from a jets-only data. Numerically, the number of background events from fakes is given by

$$N_{fakes} = N \times P_{j \rightarrow e}$$

where

N_{fakes} is the estimated number of "fake" events

N is the number of jets in the background data sample which, when misidentified, would result in a $t\bar{t} \rightarrow e\mu$ signal

$P_{j \rightarrow e}$ is the probability of a jet faking an electron (fakerate).

This $P_{j\to e}$ is purely data driven and the data sample involves mainly the jet triggers, so that the electron contamination is very low. Therefore, any electron found in this data set (passing the electron selection criteria of the analysis) should be accounted for to be coming from a misidentified jet. The $P_{j\to e}$ varies from cryostat to cryostat and also differs for different electron id requirements. For the present analysis the $P_{j\to e}$ is $(1.39 \pm 0.11) \times 10^{-4}$ for CC and $(3.88 \pm 1.98) \times 10^{-4}$ for EC. Using this, the "fake" background is estimated to be

$$0.0160 \pm 0.0040$$

events. This, when added to the above estimated physics backgrounds (table 7.8), yields the total background to be

$$0.318 \pm 0.075$$

events from 76.6 pb^{-1}, where error includes both the statistical and systematic errors added in quadrature.

Chapter 8

Collider Data Analysis

In this chapter we discuss the final step of the analysis performed for the search of the top quark in the $e\mu$ decay channel. This involves looking into the collider data collected with the DØ detector. The chapter begins with a description of the data sample and the triggers used in this analysis. Using the electron and muon identification cuts (defined in the previous chapter for getting the respective efficiencies) and the kinematic cuts, an offline event selection is made to look for the top signal. In the end, the DØ top search results for both the collider runs (1a and 1b) are summarized along with the latest top mass measurement results.

8.1 Data Sample

The analysis data was taken with the DØ detector from January 1994 to July 1995 which is referred to as the Run 1b. The raw data was recorded on magnetic tapes and reconstructed on UNIX nodes by DØRECO (version 12). The reconstructed data are

written to different streams corresponding to different physics studies. This streamed data is then used to select the initial $e\mu$ sample which is dumped on hard disks in condensed format for final analysis. Before the final data analysis, some of the unusable data sets have to be removed from this sample and the corrected integrated luminosity has to be calculated. The corrections for luminosity include the bad runs and Main Ring (MR) Veto factors described below.

- Bad Runs: Bad runs are those runs which were recorded when the detector or the data acquisition (DAQ) system had some problems. These problems could be due to level 2 trigger corruption, tracking chamber high voltage being down and calorimeter electronics problem, etc. Another type of runs which are known as "special" runs are also excluded from the final data sample, as these are recorded for some specialized studies and involved a different trigger list not meant for $t\bar{t}$ study.

- MR Veto: Since the Main Ring passes through the DØ hadronic calorimeter, this leaves a big splash of energy being seen by the muon chambers and the hadronic calorimeter if at the same time the Tevatron beam is passing (means we are recording the data). The event being recorded during this coincidence loses the useful information for analysis purposes and hence thrown out of final data list. This corresponds to a loss of about 9% in total recorded luminosity.

Thus the final integrated luminosity accumulated by the $e\mu$ channel for run 1b is

$$76.6 \pm 4.1 \text{ pb}^{-1}$$

where the standard DØ luminosity error of 5.4% [87] is used.

8.2 Triggers

The run 1b data was collected using a number of level 2 triggers. The triggers which were used in the selection of the $e\mu$ data sample are listed in table 8.1. Whenever we talk of an event passing the trigger requirements, it means that one of the triggers from this list of four has fired (in the selection procedure an OR logic is required among these four). Both the MU_JET triggers incorporated the use of cosmic scintillator (section

Trigger	Definition
MU_ELE	1 electron, $E_T > 10$ GeV 1 muon, $p_T > 8$ GeV
ELE_JET_HIGH	1 electron, $E_T > 15$ GeV, $\|\eta\| < 2.5$ 2 jets ($\Delta R = 0.3$), $\|\eta\| < 2.5$ & $E_T > 10$ GeV $\not{E}_T > 14$ GeV
MU_JET_HIGH	1 muon, $p_T > 10$ GeV 1 jet ($\Delta R = 0.7$), $E_T > 15$ GeV, $\|\eta\| < 2.5$
MU_JET_CENT	1 muon, $\|\eta\| < 1.0$ (CF) & $p_T > 10$ GeV 1 jet ($\Delta R = 0.7$), $E_T > 15$ GeV

Table 8.1: Level 2 Triggers used in run 1b.

3.3.2) as soon as it was available during run 1b.

8.3 Offline Event Selection

The selection cuts described in section 7.2 are now applied to the run 1b data. All the object id (section 7.1), for electron and muon, and the level 2 trigger cuts are applied

here, whereas for the MC case these id and trigger efficiencies are used in the calculation of final acceptances. The number of events surviving after each cut are listed in table 8.2. Figure 8.1 shows the $1/p_T^\mu$ versus E_T^e plot for the two surviving events after the final

Selection Cut	Event Yield (76.6 pb^{-1})
0. Initial Selection: $E_T^e \geq 10$ GeV, $\lvert det.\eta^e \rvert < 3.3$ & $p_T^\mu \geq 7$ GeV, $\lvert\eta^\mu\rvert < 2.5$ (no id)	≈ 500 K
1. $E_T^e > 15$ GeV, $p_T^\mu > 15$ GeV/c + $\lvert\eta\rvert$ + trigger and full μ & e Id cuts	122
2. Require Isolated muons: $\Delta R_{\mu,jet} \geq 0.5$	56
3. $\not{E}_T > 10$ GeV (muon corrected)	38
4. $\not{E}_T^{cal} > 20$ GeV (calorimeter/ICD/MG)	18
5. $\Delta R_{e\mu} > 0.25$	17
6. Require 2 jets, $E_T^{jet} > 15$ GeV	4
7. H_T $(E_T^e + \sum E_T^{jet}) > 120$ GeV	2
8. 2 jets, $E_T^{jet} > 20$ GeV	2

Table 8.2: Number of data events passing each level of selection cuts.

cut.

8.4 Anything Interesting

The two surviving events (events 12814 and 26920) from the above offline selection were looked at carefully for any uncertainties. The detailed parameters of these two events are given in table 8.3. Figures 8.2 and 8.3 show the DØ event displays for event 12814 (end-view and $\eta - \phi$ view). Figure 8.4 shows the $\eta - \phi$ Lego plot for the second surviving event 26920 and figure 8.5 shows the $r - z$ view of the event (muon with

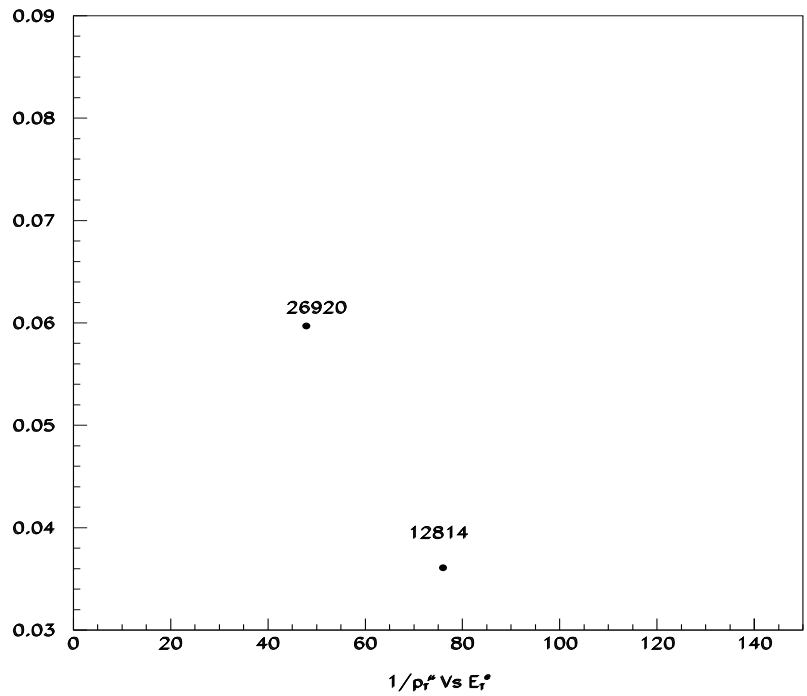

Figure 8.1: $1/p_T^{\mu}$ Vs E_T^e plot after the final cut.

its mip trace in calorimeter is clearly visible). The quality of the electrons in the two top candidate events is shown in figures 8.6 and 8.7. These two figures show the electromagnetic energy deposition in the EM Calorimeter where identification of an EM cluster, depending on the quality (chapter 5), is made as an electron.

8.5 Summary of $e\mu$ analysis

The analysis performed to search for the top quark in the $e\mu$ decay channel was described in the previous sections and in the previous chapter. The analysis assumes Standard Model couplings and branching ratios and is based on an integrated luminosity of 76.6 ± 4.1 pb^{-1} accumulated by the DØ detector during its second collider run (run

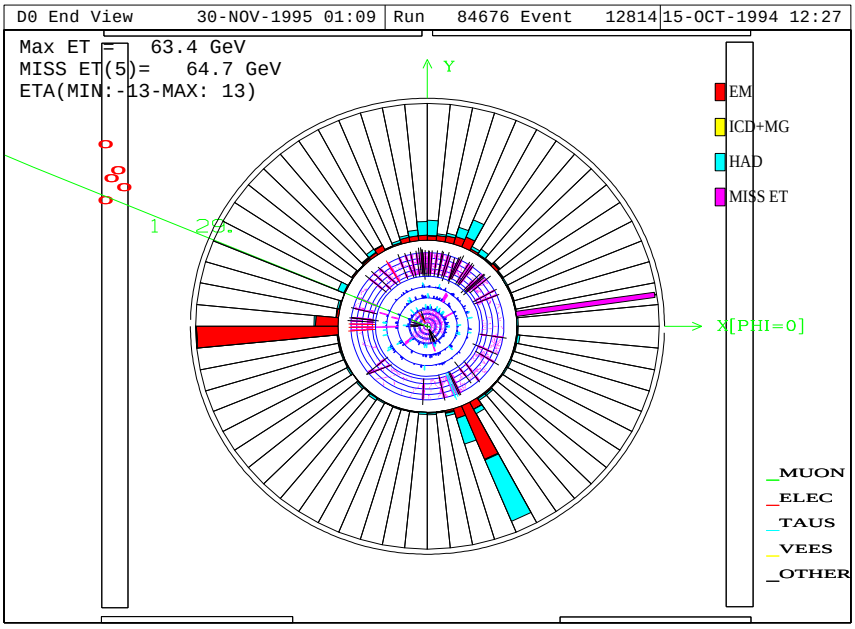

Figure 8.2: DØ end-view of event 12814.

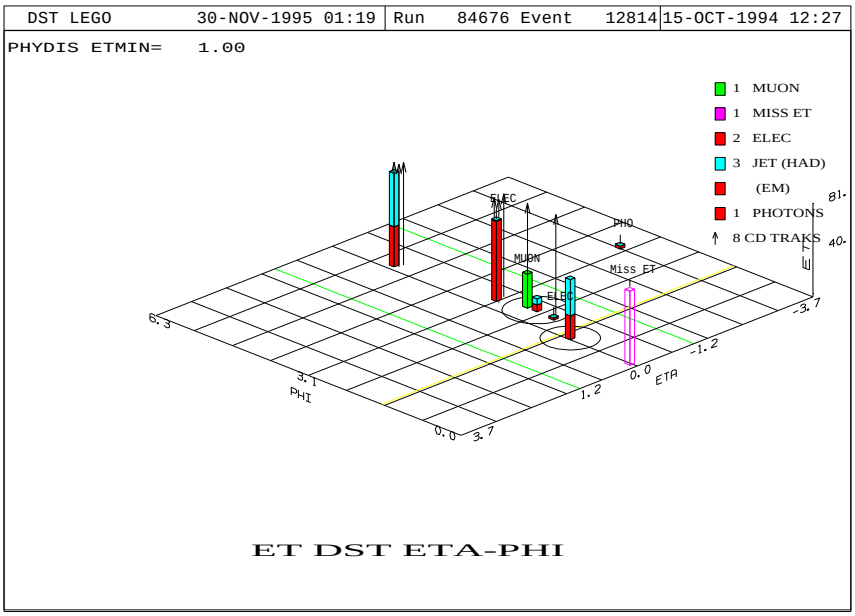

Figure 8.3: $\eta - \phi$ lego plot of event 12814.

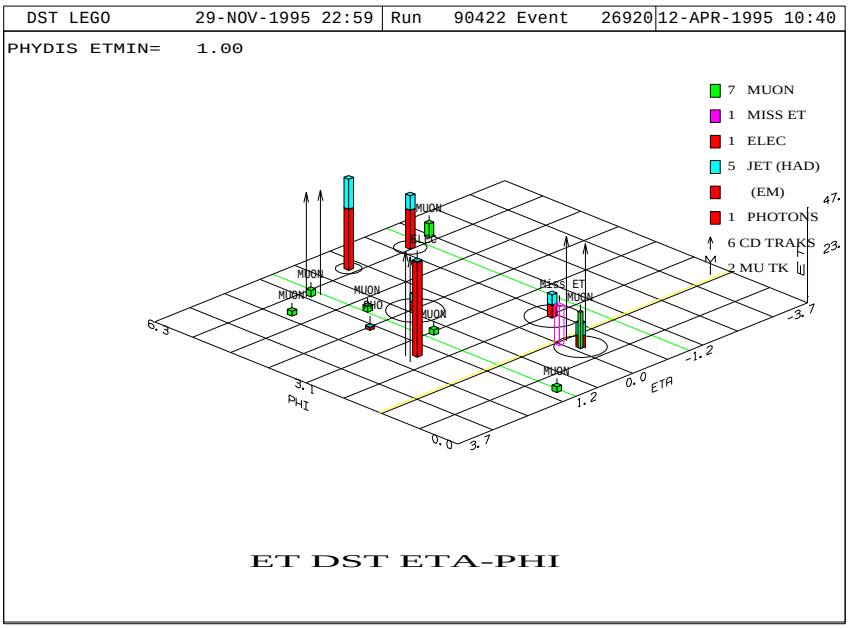

Figure 8.4: $\eta - \phi$ lego plot of event 26920.

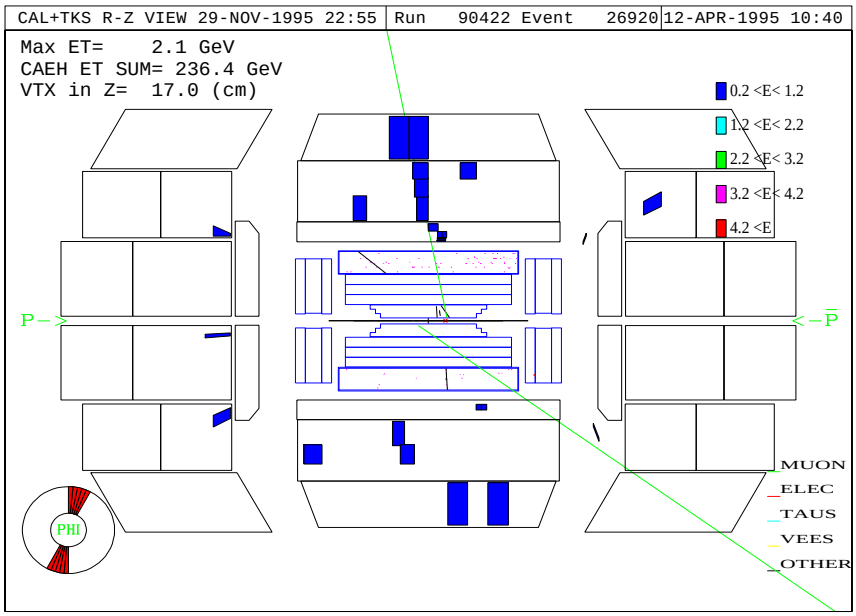

Figure 8.5: $r - z$ view of event 26920.

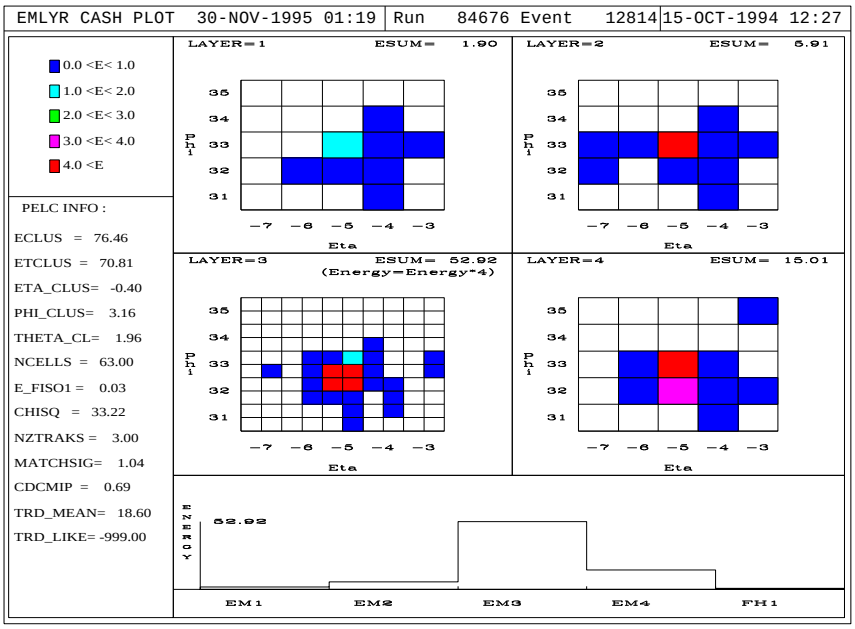

Figure 8.6: EM Shower profile of e in event 12814.

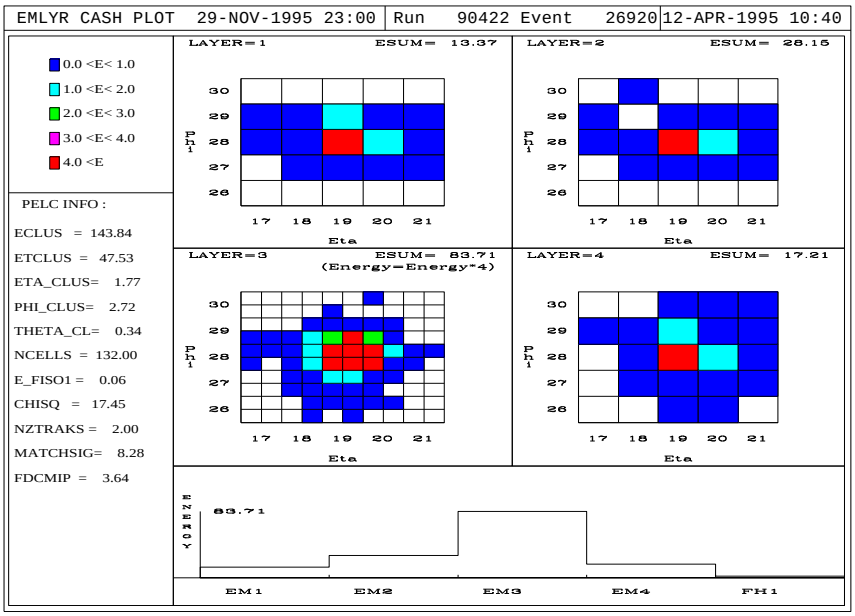

Figure 8.7: EM Shower profile of e in event 26920.

Parameter	Event 12814	Event 26920
# of event vertex	1	1
z-vertex (cm)	-6.17	18.23
Instantaneous luminosity (pb^{-1})	8.56	12.24
E_T^e (GeV)	75.45	49.41
η_e	-0.4	1.76
Detector η_e	-5.00	19.0
ϕ_e	3.16	2.72
H-Matrix χ^2	33.22	17.49
f_{isol}	0.02	0.06
σ_{track}	1.06	8.57
$\frac{dE}{dx}$	0.69	3.64
$\mathcal{R}$ (electron likelihood)	0.0483	0.2895
p_T^μ (GeV/c)	27.35	16.77
η_μ	-0.45	-0.19
ϕ_μ	2.75	1.38
# of Z tracks	1	2
MTC_HFRAC	1.0	1.0
MTC_EFRH1	0.3011	0.2742
IFW4	0	1
MUCTAG	0	0
$\int B.dl$	0.71	0.65
# of hits in layer A, B and C	4, 2 and 2	3, 3 and 3
Global fit χ^2	1.45	235.99
$\not{E}_T^{cal}$ (GeV)	40.06	22.94
$\not{E}_T$ (muon corrected) (GeV)	62.26	23.48
# of jets ($E_T > 15$ GeV)	3	2
E_T, η, ϕ & Det. η: Jet1	91.95, -0.17, 5.14, -0.23	48.14, 0.21, 5.64, 0.40
E_T, η, ϕ & Det. η: Jet2	35.15, -0.31, 1.17, -0.38	26.03, -0.97, 5.51, -0.83
Final H_T (GeV)	231.22	123.58
μ-Blank	0	0

Table 8.3: Details of the two $e\mu$ candidates from run 1b.

1b). The final results are summarized in table 8.4. The errors on the expected number of

	Events (76.6 pb^{-1})
Top MC (180 GeV)	1.47 ± 0.27
Total Background	0.318 ± 0.075
Data	2

Table 8.4: $e\mu$ final summary for run 1b.

events and the total number of background events include statistical as well as systematic errors (including the standard DØ systematic error of $\pm 5.4\%$ on the luminosity). This data can be used to set an upper limit on the top quark production cross section, which is of major significance as this limit leads to a lower limit on top mass (M_t).

8.5.1 Cross Section from $e\mu$ Channel

The relationship between the number of events expected (N_{exp}) in a channel and the cross section for that channel is given by

$$N_{exp} = \sigma \cdot (\varepsilon \times B) \cdot \left(\int \mathcal{L} dt\right)$$

where $\varepsilon \times B$ is the acceptance and $\int \mathcal{L} dt$ is the integrated luminosity.The presence of background events modifies this equation then the $\sigma_{t\bar{t}}$ is given by

$$\sigma_{t\bar{t}} = \frac{N_{obs} - N_{bkgd}}{(\varepsilon \times B) \cdot (\int \mathcal{L} dt)}.$$

For the present analysis, N_{obs}, the number of observed events are 2 and N_{bkgd}, the number of estimated background events, is $= 0.318 \pm 0.075$ (table 8.4). Using $\int \mathcal{L} dt = 76.6 \pm 4.1$ pb^{-1} and the acceptances from table 7.5, the above $\sigma_{t\bar{t}}$ equation gives the $t\bar{t}$ production

cross sections for the $e\mu$ channel, which are listed in table 8.5, for various top masses. The errors on the measured cross sections include both the statistical and systematic

M_t (GeV/c^2)	$\sigma_{t\bar{t}}$ (pb)
140	7.84 ± 6.75
150	6.66 ± 5.73
160	5.28 ± 4.54
180	4.82 ± 4.15
200	4.38 ± 3.77
220	4.37 ± 3.76
250	2.81 ± 2.42

Table 8.5: Measured $\sigma_{t\bar{t}}$ from the $e\mu$ channel.

uncertainties. The dominant error is due to the small statistics of top candidate events.

8.6 Conclusions

Similar to the $e\mu$ search analysis, analyses were performed to look for top in other search channels (section 1.5) using 1b data. These are: ee, $\mu\mu$, $e+$ jets, $\mu+$ jets and $e/\mu+$ jets with soft μ-tag. During the first collider run for DØ, run 1a (1992 - 1993), about 14 pb^{-1} of luminosity was recorded and analyses similar to run 1b were performed to search for the top quark. The top $\rightarrow e\mu$ channel saw one top candidate event (event 417) in a similar run 1a analysis [35], making the total to 3 $e\mu$ top candidate events (2 from run 1b as described in the previous sections) from the two collider runs. Presently, there are other analysis techniques (known as "multivariate" techniques) being used in the data analysis for the $e\mu$ channel and the details are available in [88, 89]. The details of all

the seven run 1a analyses are available in [58]. A summary of results from all the seven channels (3 dilepton channels, 2 lepton + jets and 2 lepton + jets with μ-tag) for run 1a, 1b combined are tabulated in tables 8.6 and 8.7. Using the total number of top events

Channel	$\int \mathcal{L}dt$ (pb^{-1})	Background	Signal (Top 180 GeV)	Data
$e\mu$	90.5 ± 4.9	0.36 ± 0.09	1.69 ± 0.27	3
ee	105.9 ± 5.7	0.66 ± 0.17	0.92 ± 0.11	1
$\mu\mu$	86.7 ± 4.7	0.55 ± 0.28	0.53 ± 0.11	1
e+ jets	105.9 ± 5.7	3.81 ± 1.41	6.46 ± 1.38	10
μ+ jets	95.7 ± 5.2	5.42 ± 2.05	6.40 ± 1.51	11
e+ jets (μ-tag)	90.5 ± 4.9	1.45 ± 0.42	2.43 ± 0.42	5
μ+ jets (μ-tag)	95.7 ± 5.2	1.13 ± 0.23	2.78 ± 0.92	6

Table 8.6: Run 1a+1b top search results for dilepton, lepton + jets and lepton + jets with μ-tag channels (errors include correlations between channels).

Total	Background	Signal Expected (Top 180 GeV)	Data
Seven Channels	13.4 ± 3.0	21.2 ± 3.8	37

Table 8.7: Summary of 1a+1b top search results.

seen, the total estimated background, the overall top acceptance and the integrated luminosity for the seven top search channels, a total $t\bar{t}$ production cross section ($\sigma_{t\bar{t}}$), background subtracted, is calculated (see section 8.5.1). Figure 8.8 shows the DØ top production cross section and the theoretical $\sigma_{t\bar{t}}$ at the Tevatron energies. For a 180 GeV top, the value of $\sigma_{t\bar{t}} = 4.69 \pm 1.62$ pb.

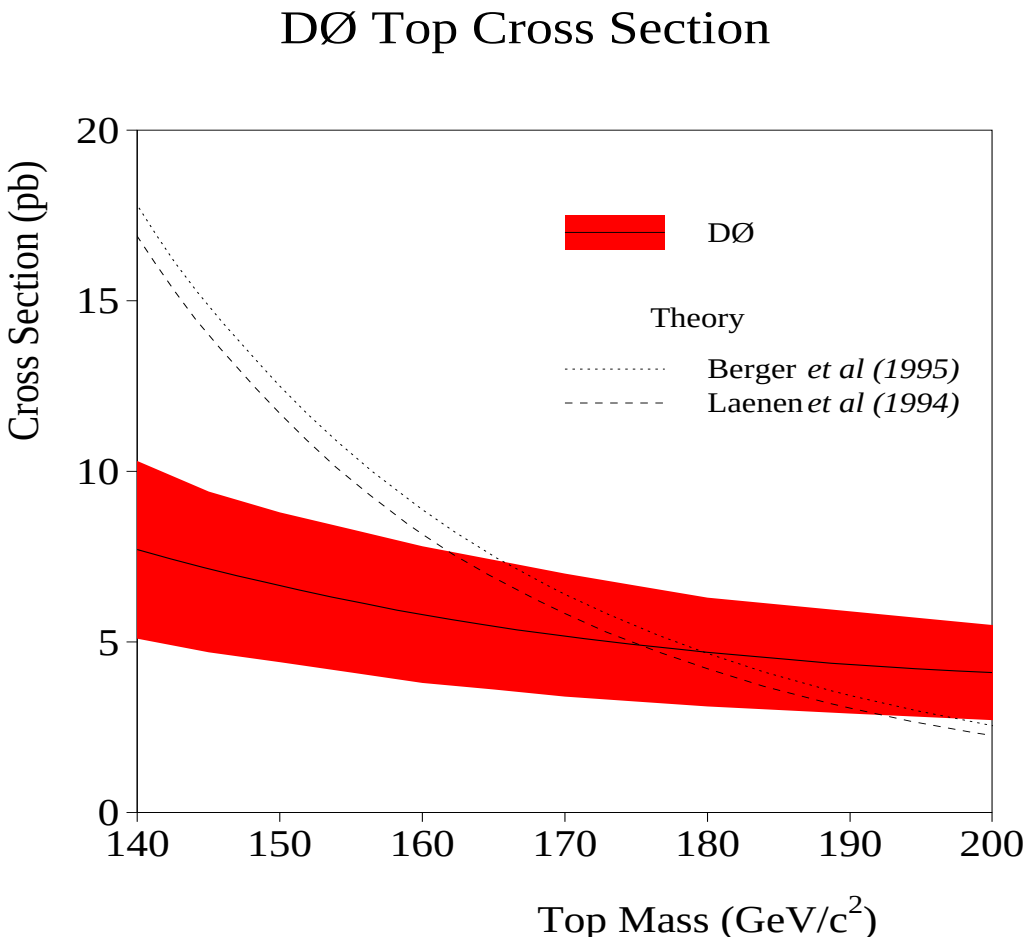

Figure 8.8: DØ top cross section.

8.7 Final Remarks

The DØ discovery paper was published [1] using an $\int \mathcal{L} dt = 50.0$ pb^{-1} collected during the 1992 - 1995 collider run, in which 3 *dileptons* and 4 *lepton* + jets (with/without muon tag) channels were used yielding 17 top candidate events with an expected background of 3.8 ± 0.6 events. The probability for an upward fluctuation of this background to produce the observed signal is 2×10^{-6} ($\equiv 4.6\ \sigma$), firmly establishing the existence of the top quark. At the present stage, we have about 100 pb^{-1} of data (collected during the two collider runs) and we observe 37 top candidate events from 7 channels (previous section), with an estimated background of 13.4 ± 3.0 events.

The next step of measuring the top mass will provide a greater insight into the missing pieces of the Standard Model and beyond (see chapter 1). Hence, using these observed events, the top mass is measured using a maximum likelihood fit method. The description of the fitting method is beyond the scope of this thesis. The details are available in [41, 90]. The latest top mass measurement, using the *leptons* + jets events, gives $M_t = 169 \pm 8(sta) \pm 10(sys)$ GeV [91] and using only the $e\mu$ channel, the measured top mass is $158 \pm 24(sta) \pm 10(sys)$ GeV [92]. So for a 170 GeV top, the DØ $t\bar{t}$ production cross section is measured as 5.2 ± 1.8 pb.

The next DØ run would be with an upgraded detector, for which the work is under progress. In its new look, the DØ detector will have a silicon vertex detector, thus enabling the b-vertex tagging and a central magnetic field which will improve the muon momentum resolution and electron identification. We see a future full of "tops" with all these improvements and will be able test the Standard Model thoroughly thus opening up the door to beyond the Standard Model surprises.

BIBLIOGRAPHY

[1] DØ Collaboration, S. Abachi *et al.*, Phys. Rev. Lett., **74:** 2632, April 1995.

[2] CDF Collaboration, F. Abe *et al.*, Phys. Rev. Lett., **74:** 2626, April 1995.

[3] A. Einstein, *The Principle of Relativity*, (Methuen, 1923) reprinted by Dover, New York (1952).

[4] J. C. Maxwell, *Treatise on Electricity and Magnetism*, 3rd edition (1891), 2 vols. reprint by Dover, New York (1954).

[5] P. A. M. Dirac, *Proc. Roy. Soc. London*, **A114:** 243,710 (1927).

[6] M. Kaku, *Quantum Field Theory*, (Oxford University Press, New York): 5 (1993).

[7] E. Fermi, Z. Phys. **88:** 161 (1934).

[8] R. Crease and C. Mann, *The Second Creation*, (MacMillian Publishing Co., New York): 211 (1986).

[9] G. D. Coughlan and J. E. Dodd, *The ideas of particle physics*: An Introduction for Scientists, (Cambridge University Press, Cambridge) (1991).

[10] Kerson Huang, *Quarks, Leptons & Gauge Fields*, (World Scientific, Singapore): 105 (2nd edition, 1992).

[11] Particle Data Group, Phys. Rev., **D50:** 1173-1876 (August 1994).

[12] The program used for this calculation was written by Gerrit Burgers (CERN/TH).

[13] V. D. Barger and R. J. N. Phillips, *Collider Physics*, (Addison-Wesley Publishing Co., Redwood City, California) (1987).

[14] I. Halzen and Alan D. Martin, *Quarks and Leptons: An Introductory Course in Modern Particle Physics*, John Wiley & Sons, New York (1984).

[15] K. Gottfried and V. F. Weisskopf, *Concepts of Particle Physics*, Vol. 1, (Oxford University Press, New York): 165 (1984).

[16] G. Kane, *Modern Elementary Particle Physics*, (Addison-Wesley Publishing Co., Reading, Massachusetts) (1993).

[17] E. Laenen, J. Smith and W. L. van Neerven, Phys. Lett. **B321:** 254-258 (1994).

[18] E. Laenen, A note on the lower limit of the top quark production rate at the Tevatron, FERMILAB-PUB-93/155-T (June 1993).

[19] C. Quigg, Top–ology, FERMILAB-CONF-95/139-T (1995).

[20] D. Schaile. *Proceedings of the 1994 International Conference on High Energy Physics*, edited by P. J. Bussey and I. G. Knowles (Institute of Physics, London): 27 (1995).

[21] CDF Collaboration, F. Abe *et al.*, Phys. Rev. **D45:** 3921-3948 (1992).

[22] DØ Collaboration, S. Abachi *et al.*, Phys. Rev. Lett. **72:** 2138 (1994).

[23] Particle Data Group, Phys. Rev., **D54:** 309 (Part I, July 1996).

[24] CDF Collaboration, F. Abe *et al.*, Phys. Rev. Lett. **73:** 225 (1994); Phys. Rev. **D50:** 2966 (1994).

[25] DØ Collaboration, S. Abachi *et al.*, Phys. Rev. Lett. **74:** 2422 (1995).

[26] J. Thompson, *Introduction to Colliding Beams at Fermilab*, DØ Note 2367 (FERMILAB-TM-1909) (October 1994).

[27] L. M. Lederman, *The Tevatron*, Scientific American, **Vol. 264:** 53, March 1991.

[28] M. P. Church and J. P. Marriner, Ann. Rev. Nucl. Part. Sci. **43:** 253-295 (1993).

[29] D. Möhl, G. Petrucci, L. Thorndhal and S. van der Meer, Phys. Rep. **C58:** 73-119 (1980).

[30] DØ Collaboration, S. Abachi *et al.*, Nucl. Inst. and Meth. in Phys. Res. **A338:** 185-253 (1994).

[31] A. R. Clark *et al.*, Nucl. Inst. and Meth. in Phys. Res. **A279:** 243-248 (1989).

[32] A. R. Clark *et al.*, Nucl. Inst. and Meth. in Phys. Res. **A315:** 193 (1992).

[33] J. F. Detoeuf *et al.*, Nucl. Inst. and Meth. in Phys. Res. **A265:** 157-166 (1988).

[34] J. F. Detoeuf *et al.*, Nucl. Inst. and Meth. in Phys. Res. **A279:** 310-316 (1989).

[35] James. H. Cochran, Jr., *Search for Truth in the $e\mu$ Channel.* Ph. D. Thesis, SUNY at Stony Brook, New York, 1994 (unpublished).

[36] S. Rajagopalan, *The dE/dx Capabilities of the DØ Tracking System.* Ph. D. Thesis, Northwestern University, Evanston, Illinois (June 1992).

[37] D. Buchholz *et al.*, Nucl. Inst. and Meth. in Phys. Res. **A257:** 556-566 (1987).

[38] Jeffrey W. Bantly, *The DØ Detector Forward Drift Chamber Performance and Physics Capablity in the 1990 FNAL Testbeam Run.* Ph. D. Thesis, Northwestern University, Evanston, Illinois (June 1992).

[39] David F. Anderson, *Principles of EM Calorimetry*, Academic Lecture Series, Fermilab (April 1993).

[40] Richard Wigmans, Nucl. Inst. and Meth. **A259:** 389-429 (1987).

[41] Scott S. Snyder, *Measurement of the Top Quark Mass at DØ.* Ph. D. Thesis, SUNY at Stony Brook, New York, 1995 (unpublished).

[42] V. Bhatnagar and J. B. Singh, *Study of Hadron Punchthrough in DØ*, DØ Note 1858, 1993 (unpublished).

[43] C. Gerber *et al.*, *Muon Momentum Determination*, DØ Note 2140, 1994 (unpublished).

[44] C. Brown *et al.*, Nucl. Inst. and Meth. **A279:** 331-338 (1989).

[45] J. M. Butler *et al.*, Nucl. Inst. and Meth. **A290:** 122-130 (1990).

[46] Yu. M. Antipov *et al.*, Nucl. Inst. and Meth. **A297:** 121-125 (1990).

[47] V. Bhatnagar, S. Chopra, A. S. Ito, J. M. Kohli and J. B. Singh, *Fiber Studies for the Muon Scintillators*, DØ Note 2421, 1994 (unpublished).

[48] G. S. Gao and R. Partridge, IEEE Trans. Nucl. Sci. **38**(2): 286-289 (1991).

[49] J. Bantly *et al.*, *The level 0 trigger for the DØ detector*, DØ Note 1996, (1993).

[50] W. J. Thompson, *Search for the Top Quark in the Muon + Jets Channel at DØ.* Ph. D. Thesis, SUNY at Stony Brook, New York, 1994 (unpublished).

[51] Balamurali V., *Search for the Top Quark in the Dielectron Channel in $p\overline{p}$ Collisions at $\sqrt{s} = 1.8$ TeV*, Ph. D. Thesis, University of Notre Dame, Indiana, 1994 (unpublished).

[52] M. Fortner *et al.*, *IEEE Trans. Nucl. Sci.* **38**(2): 480-485 (1991).

[53] Myungyun Pang, *Search for top in $p\overline{p}$ collisions at $\sqrt{s} = 1.8$ TeV by constrained kinematic fitting.* Ph. D. Thesis, Iowa State University, Ames, Iowa (1994).

[54] Jaehoon Yu. *Determination of the Strong Coupling Constant (α_s) and a Test of perturbative QCD Using $W+$ jets Processes in the DØ detector.* Ph. D. Thesis, SUNY at Stony Brook, New York, August 1993.

[55] UA1 Collaboration, G. Arnison *et al.*, Phys. Lett. **B123:** 115-122 (1983).

[56] UA1 Collaboration, G. Arnison *et al.*, Phys. Lett. **B132:** 214-222 (1983).

[57] N. J. Hadley, *Cone algorithm for jet finding*, DØ Note 904, November 1989 (unpublished).

[58] DØ Collaboration, S. Abachi *et al.*, Phys. Rev. **D52**: 4877 (1995).

[59] Saul Youssef, *Comp. Phys. Comm.* **45:** 423-426 (1987).

[60] T. C. Awes *et al.*, Nucl. Inst. and Meth. **A311:** 130-138 (1991).

[61] Dhiman Chakraborty, *A search for $t\overline{t} \rightarrow$ electron + $\not\!\!E_T$ + jets signature in $p\overline{p}$ collisions at $\sqrt{s} = 1.8$ TeV with the DØ detector.* Ph. D. Thesis, SUNY at Stony Brook, New York, September 1994.

[62] R. Engelmann *et al.*, Nucl. Inst. and Meth. **A216:** 45-56 (1983).

[63] T. Diehl and D. Hedin, *DØ muon level 2 filter*, DØ Note 1325, January 1992 (unpublished).

[64] U. Heintz, *Standard EM Energy Scale Correction for RECO V10*, DØ Note 1758, Jun 1993 (unpublished).

[65] Mrinmoy Bhattacharjee, private communication.

[66] R. Astur, *Correction of* $\not{E}_T$, DØ Note 2088 (1994).

[67] S. Protopopescu, *Event Simulation for Hadron Colliders*, "University of DØ proceedings", August 1991 (unpublished).

[68] G. Altarelli and G. Parisi, Nucl. Phys. **B126:** 298 (1977).

[69] R. D. Field and R. P. Feynman, Nucl. Phys. **B136:** 1 (1978).

[70] B. Anderson, G. Gustafson, G. Ingelman and T. Sjöstrand, Phys. Rep. **97:** 33 (1983).

[71] B. R. Webber, *Monte Carlo Simulation of Hard Hadronic Processes* in Ann. Rev. Nuc. Sci. Vol. 36: 279, (Annual Reviews Inc. Palo Alto) (1986).

[72] J. C. Collins and T. D. Gottschalk, *Assesment of Perturbative Monte Carlos For Hadron-Hadron Scattering*, Proceedings of Snowmass 85: 303.

[73] R. Brun *et al.*, GEANT 3.14 program manual, CERN.

[74] J. Womersley, *The DØ Monte Carlo*, DØ Note 1520, August 1992 (unpublished).

[75] J. T. Linnemann, *Triggering the DØ Experiment*, in *The Fermilab Meeting DPF92*, Vol.2: 1642 (1992).

[76] T. Diehl, *MU_SMEAR Package Documentation*, 1993 (updated P. Quintas, 1994) (unpublished).

[77] A. I. Mincer, P. Nemethy and A. Boehnlein, *NOISY Documentation*, June 1992 (unpublished).

[78] J. Ohnemus, Phys. Rev. D44: 1403 (1991).

[79] A. Klatchko *et al.*, *Background to the top in the $e\mu$ Signature from $W\gamma$*, DØ Note 1815, July 1993 (unpublished).

[80] M. Narain and U. Heintz, *A Likelihood Test for Electron ID*, DØ Note 2386, 1994 (unpublished).

[81] M. Narain, *Electron Identification in the DØ Detector*, DØ Note 1548, 1992 (unpublished).

[82] M. Narain, *The Fermilab Meeting: Proceedings of 7th Meeting of the Division of Particles and Fields of the American Physical Society*, **Vol.2:** 1678, *edited by* C. Albright, P. Kasper, R. Raja and J. Yoh (World Scientific, Singapore, 1993).

[83] J. Neyman and E. S. Pearson, Phil. Trans. Roy. Soc., **231:** 289 (1933).

[84] J. Neyman, *First Course in Probability and Statistics*, Henry Holt & Co, 1950.

[85] J. Cochran, *Status of $t\bar{t} \to e\mu$ analysis*, DØ internal documentation, July 1996 (unpublished).

[86] E. Gallas, *The MTC Package (Muon Tracking in the DØ Calorimeter)*, DØ Note 2066, 1994 (unpublished).

[87] J. Bantly, A. Brandt, R. Partridge, J. Perkins and D. Puseljic, *Improvement to the DØ luminosity monitor constant*, DØ Note 2544, 1995 (unpublished).

[88] S. B. Beri, P. Bhat, R. Raja, H. Prosper, *An H-matrix study of the $t\bar{t} \to e\mu$ channel*, DØ Note 2227, Sep. 1994 (unpublished).

[89] Harpreet Singh, S. B. Beri, *Top via $e\mu$ using Neural Nets at DØ*, DØ Note 3071, Aug. 1996 (unpublished).

[90] Erich W. Varnes, *Top Quark Mass fitting in the Dilepton Channel by Approximate Integration over Neutrino variables*, DØ Note 2654, July 1995 (unpublished).

[91] P. Bhat, J. Cochran, F. Hsieh, M. Jones, R. Gilmartin, J. McDonald, R. Partridge, H. Prosper, S. Protopopescu, S. Snyder, M. Strovink, T. Trippe, E. Varnes and G. Watts, *Measurement of Top Mass Using Lepton + Jets Events*, DØ Note, 1996 (unpublished).

[92] M. Narain, (for the DØ Collaboration), presented at Les Rencontres de Physique de La Vallee D'Aoste, La Thuile, Italy (Mar. 1996).